## Abstract

**KIEFER, AARON JOSEPH.** Integrating Electromechanical Actuator Hardware with Receptance Coupling Substructure Analysis for Chatter Prediction on High Speed Machining Centers. (Under the direction of Dr. Gregory Dale Buckner).

Machine tool chatter imposes limitations on the productivity and quality of modern high speed machining (HSM) operations. It has been shown that chatter prediction and avoidance strategies can lead to increased machining productivity if certain modal characteristics of the machine are known. The objectives of this research are twofold.

The first aim is to design and demonstrate a non-contacting electromechanical actuator (EMA) to easily and accurately identify these characteristics. Design specifications for this actuator reflect a wide range of machine tools and operating conditions. A simulation-based design strategy is employed, based on traditional electromechanical analysis, finite element analysis (FEA), and computer simulations to ensure performance meets the design specifications. A prototype EMA system is built to validate the analytical results and demonstrate its capabilities as part of an automated chatter prediction and avoidance system. The EMA is shown to generate the required modal characteristics, namely frequency response functions (FRFs) quickly, accurately, and with fewer technical skill requirements than other vibration testing methods. Experimental machining tests demonstrate that the EMA can be an effective component of an integrated chatter prediction and avoidance system.

The second goal is to investigate the feasibility of extending receptance coupling substructure analysis (RCSA) theory to tool-point FRF prediction. Inverse and forward RCSA algorithms are developed using Matlab software. FRF prediction is first evaluated in simulation and later tested with experimental results from the EMA actuator. RCSA prediction in simulation is correct; experimental results are highly susceptible to input error.

# INTEGRATING ELECTROMECHANICAL ACTUATOR HARDWARE WITH RECEPTANCE COUPLING SUBSTRUCTURE ANALYSIS FOR CHATTER PREDICTION ON HIGH SPEED MACHINING CENTERS.

(Under the direction of Dr. Gregory Dale Buckner).

Submitted by

AARON J KIEFER

A thesis submitted to the Graduate Faculty of
North Carolina State University
in partial fulfillment of the
requirements of the degree of
Master of Science

MECHANICAL & AEROSPACE ENGINEERING

Raleigh, North Carolina
March 2004

APPROVED BY:

| | |
|---|---|
| Dr. Eric C. Klang<br>(Advisory Committee Member) | Dr. Melur K. Ramasubramanian<br>(Advisory Committee Member) |

Dr. Gregory D. Buckner
(Chair of Graduate Advisory Committee)

# Dedication

To my family for their continued love and support.

## Biography

Aaron Joseph Kiefer was born in Durham, North Carolina, in 1980. He was schooled at home in Chapel Hill from kindergarten through high school. Aaron chose North Carolina State University and Mechanical Engineering because he loves cars and trucks and things that go.

Aaron attended graduated from NCSU in December, 2002 with a BS degree in Mechanical Engineering. His second graduation from NCSU, in May of 2004, will be followed by a semester of living and training at the national triathlon training center located in Cleremont, Florida.

## Acknowledgements

My family has always supported me – I want to thank my parents especially for inspiring me to work to my very best to the glory of God.

I would like recognize Dr. Donald Esterling of Vulcancraft LLC for his generous support and for his many instructive contributions to this research project. I also owe much to F. Donald Caulfield who was my predecessor in this research.

Thanks to Dr. Gregory Buckner for providing leadership and direction.

I also want to acknowledge Mike Breedlove, Skip Richardson, and Dale Myatt for their hard work and unending patience with this project.

# Table of Contents

List of Figures ..... vi
List of Tables ..... viii
1. Introduction [1] ..... 1
2. Background: Machining Chatter ..... 5
2.1 Stability Lobe Diagrams ..... 6
2.2 Simulations ..... 8
2.3 Experimental Techniques ..... 9
*2.3.1 In-Situ Control* ..... 9
*2.3.2 A-Priori Prediction* ..... 10
3. Receptance Coupling Substructure Analysis (RCSA) ..... 12
3.1 Overview ..... 12
*3.1.1 Inverse RCSA* ..... 14
3.2 Mass Spring Damper Simulations ..... 15
*3.2.1 Solving for Subsystem 1 Receptance* ..... 19
3.2.2 *Predicting Compound Receptance* ..... 22
4. Tool-point FRF Prediction using RCSA ..... 26
4.1 Identifying Toolholder Receptance ..... 26
4.2 Predicting Tool-point (Compound) FRFs ..... 33
5. Tool-point FRF Prediction using RCSA: Experimental Results ..... 35
5.1 Experimental Setup ..... 35
5.2 Hammer Test Results ..... 39
5.3 Inverse RCSA: Finding Subsystem Receptances ..... 42
5.4 Forward RCSA: Predicting New Tool-point FRFs ..... 45
5.5 Modal Testing Drawbacks ..... 47
6. Experimental RCSA – Non Contacting EMA ..... 52
6.1 EMA System Design ..... 53
6.1.1 RCSA Requirements ..... 54
6.1.2 Hardware Design ..... 54
6.1.3 Actuation Force Measurement ..... 57
6.2 EMA Experimental Setup ..... 70
6.3 EMA Test Results ..... 72
6.4 Inverse RCSA: Finding Subsystem Receptance ..... 77
6.5 Forward RCSA: Predicting Tool-point FRFs ..... 80
7. RCSA Prediction Errors ..... 82
8. Conclusions ..... 88
9. Bibliography ..... 90

# List of Figures

Figure 2-1: Stability Lobe Diagram [26] ..... 7
Figure 3-1: Linear spring mass system ..... 13
Figure 3-2: Linear, 2 DOF Mass Spring Damper System ..... 16
Figure 3-3: Simulink Model for the Double MSD System ..... 16
Figure 3-4: $X_1/F_1$ Frequency Response for the Double MSD System ..... 17
Figure 3-5: Inverse RCSA Flowchart: Double Spring Mass Damper Simulation ..... 18
Figure 3-6: Forward RCSA Flowchart: Double Spring Mass Damper Simulation ..... 18
Figure 3-7: Swept Sinusoid Force Profile ..... 19
Figure 3-8: Double MSD System Modeled as Two Subsystems ..... 20
Figure 3-9: Identified Subsystem 2 Receptance ..... 22
Figure 3-10: Forward RCSA: Combining Identified Subsystem 2 with Subsystem 3 ..... 23
Figure 3-11: Predicted Compound Receptance: Double SMD Simulations ..... 24
Figure 3-12 Predicted vs. Analytical Compound Receptances: Double SMD Simulations ..... 24
Figure 4-1: Excitation and Measurement Locations for Experimental Tool-point FRFs ..... 27
Figure 4-2: Internal Displacements and Reactions Resulting from Applied Force F1 ..... 27
Figure 4-3 External Force Applied to Tool at Location 2; Internal Reactions Shown ..... 31
Figure 5-1: Eddy Current Displacement Sensor Mount ..... 35
Figure 5-2: Modal Testing Layout ..... 36
Figure 5-3: HAAS VF-1 3-Axis CNC Machine and Experimental Setup ..... 37
Figure 5-4: 4.00 in Tool Blank Mounted in Collet Toolholder ..... 37
Figure 5-5: Simulink Modal Testing Program ..... 38
Figure 5-6: ControlDesk Modal Testing Console ..... 39
Figure 5-7: Impact Hammer Testing $X_1/F_1$ Receptance ..... 40
Figure 5-8: Impact Hammer Testing $X_2/F_1$ Receptance 5.75 in Tool ..... 41
Figure 5-9: Impact Hammer Testing $X_1/F_2$ Receptance 5.75 in Tool ..... 41
Figure 5-10: Impact Hammer Testing $X_2/F_2$ Receptance 5.75 in Tool ..... 42
Figure 5-11: Identified $B_1$ Receptance for a 4.75 in Tool (Impact Hammer Testing) ..... 43
Figure 5-12: Identified $B_2$ Receptance for a 4.75 in Tool (Impact Hammer Testing) ..... 43
Figure 5-13: Identified $B_3$ Receptance for a 4.75 in Tool (Impact Hammer Testing) ..... 44
Figure 5-14: Impact Hammer RCSA Prediction and Measured Tool-Point FRF ..... 46
Figure 5-15: Impact at Tool Tip (Location 1) ..... 48
Figure 5-16: Impact at Tool Interface (Location 2) ..... 48
Figure 5-17: Frequency Spectrum at Tool Tip (Location 1) ..... 49
Figure 5-18: Frequency Spectrum at Tool Interface (Location 2) ..... 49
Figure 5-19: $X_1/F_1$ Impact Hammer Receptance 3.25 in Tool Blank ..... 51
Figure 6-1: Electromechanical Actuator, with Support Structure and Displacement Sensor Mount (Connecting Base Plate Omitted) ..... 52
Figure 6-2: EMA Core, Custom Sensor Plate, and PCB Shear Force Sensor ..... 55
Figure 6-3: Updated ECDS Mount ..... 55
Figure 6-4: Complete EMA Experimental Setup ..... 55
Figure 6-5: FEA Modal Analysis of EMA Core and Actuator Shelf ..... 56
Figure 6-6: FEA Modal Analysis of Eddy Current Sensor Mount ..... 56
Figure 6-7: GMT Calculated Swept Sinusoid Actuation Force ..... 59
Figure 6-8: EMA Actuator Mount; Full Bridge Strain Gage Circuit ..... 60

Figure 6-9: Strain Gage Load Cell Dimensions ..... 62
Figure 6-10: Custom Strain Gage Load Cell Amplifier ..... 63
Figure 6-11: Vishay Micro Measurements 2110 Signal Conditioning Amplifier ..... 64
Figure 6-12: Strain Gage Load Cell Calibration Curve ..... 64
Figure 6-13: Impact Hammer Tests on EMA Structure with Strain Gage Load Cell ..... 65
Figure 6-14: Strain Gage Load Cell Swept Sinusoid Force Measurements ..... 65
Figure 6-15: Strain Gage Load Cell with Ferromagnetic Shield (Actuator Removed) ..... 66
Figure 6-16: PCB 201M73 Shear Force Sensor ..... 67
Figure 6-17: Offset Sinusoid EMA Core Current Input ..... 68
Figure 6-18: EMA Current Input Prep Signal (0-4 Sec) ..... 68
Figure 6-19: Actuator Response with PCB Shear Force Sensor and 5/16in Stud ..... 69
Figure 6-20: Reduced Mass Actuator Response with PCB Shear Force Sensor and 3/8in Stud ..... 70
Figure 6-21: Complete EMA Experimental Setup: Eddy Current Mount and Sensor, Actuator Core, ..... 71
Figure 6-22: Non-Contacting EMA System Hardware ..... 71
Figure 6-23: Non-Contacting EMA Actuator $X_1/F_1$ FRF 5.75in Tool ..... 73
Figure 6-24: Non-Contacting EMA Actuator $X_2/F_2$ FRF 5.75in Tool ..... 74
Figure 6-25: Non-Contacting EMA Actuator $X_1/F_2$ FRF 5.75in Tool ..... 74
Figure 6-26: Impact hammer and EMA Sweep Measured $X_1/F_1$ FRF Comparison 5.75in Tool ..... 75
Figure 6-27: Impact Hammer and EMA Sweep Measured $X_1/F_1$ FRF Comparison, 6.75in Tool ..... 76
Figure 6-28: $B_1$ Receptance Measured via EMA Actuator ..... 77
Figure 6-29: $B_2$ Receptance Measured via EMA Actuator ..... 78
Figure 6-30: $B_3$ Receptance Measured via EMA Actuator ..... 78
Figure 6-31: RCSA Predicted FRF and EMA Measured $X_1/F_1$ FRF 6.75in Tool ..... 80
Figure 6-32: Measured and Smoothed EMA $X_1/F_1$ FRF 4.75in Tool ..... 81
Figure 7-1: Enlarged View Double MSD Simulation RCSA Prediction and Analytic Solution ..... 83
Figure 7-2: RCSA Double MSD Simulation Prediction and Analytic Solution ..... 83
Figure 7-3: Enlarged View Double MSD Simulation RCSA Prediction and Analytic Solution ..... 84
Figure 7-4: Double MSD Input Comparison (Analytic and 2% White Noise) ..... 85
Figure 7-5: Computed Double MSD Subsystem Comparison (Analytic and 2% White Noise) ..... 86
Figure 7-6: RCSA Predicted Double MSD FRF Comparison (Analytic and 2% White Noise) ..... 86

# List of Tables

Table 5-1 Modal Testing Measurement Positions ..... 40
Table 6-1 Actuator Force Parameters ..... 53
Table 6-2 FEA Modal Analysis Natural Frequency Predictions ..... 56
Table 6-3: PCB Piezotronics Shear Force Sensor Specifications ..... 67
Table 6-4 Non-Contacting EMA Measurement Positions ..... 72

# 1. Introduction [1]

Recent advances in the design of machining centers have increased commercially available spindle speeds to over 40,000 rpm, and have given rise to the practical implementation of high speed machining (HSM). Using HSM, large, complex aluminum parts can be machined from a single workpiece instead of being assembled from many components. Besides the time saved in assembly, other benefits include reduced lead time, reduced waste, and parts that are simultaneously lighter, stronger, and cheaper [1].

HSM is currently finding application mainly in the aerospace industry, although a recent white paper from Unigraphics, Inc. suggests that "approximately 30 percent of the companies in the U.S. and Japan are already using HSM, with the number even greater in Germany at 40 percent. The remaining companies in all these countries are considering making an investment in HSM or are interested in this new technology" [2]. HSM will find its way into smaller machine shops as it becomes better understood and its drawbacks are addressed.

Self-induced vibration or machine tool 'chatter' is a critical limiting factor to HSM metal removal rates [3]. Vertical milling operations in particular are susceptible to regenerative chatter due to the relatively compliant nature of slender milling tools and chip load variations encountered during the discontinuous cutting process [4]. The intuitive method of chatter avoidance dictates that whenever chatter is encountered the spindle speed should be reduced. This eliminates the production gains made possible through high speed machining.

In recent years, chatter research has focused on mathematically describing and predicting the behavior of milling systems. Feedback theory, [5] modal analysis [6], iterative time domain

simulations [6, 7], and analytical and finite element models [8] have all been used to predict frequency responses and stability traits with varying degrees of success. While the capabilities of these solution methods have improved, the quality of computational output remains sensitive to the accuracy of input parameters.

Chatter avoidance techniques can be categorized to in-situ control and a-priori prediction [9]. In-situ control methods typically use sensors to detect the onset of chatter and active control strategies to reduce or eliminate the vibration. While these methods can be effective in controlling chatter after its onset, they have the disadvantage of not being able to prevent chatter from occurring. A-priori methods rely on dynamic system models, typically frequency response functions (FRFs), to predict and avoid chatter. The determination of accurate FRFs requires specialized excitation equipment and careful measurement techniques that make it impractical for widespread industrial adoption [9]. Current practice is to measure the tool-point FRFs (the combined dynamic response of the spindle, toolholder, and tool) for each cutting tool. These FRF measurements can be used to accurately predict stability regions for each tool, but require extensive experimental measurements. CNC machines with large tool carrousels could require 20 to 50 tests [10].

Recent literature has identified a method for measuring a single tool response and using this system information to predict the FRFs for a collection of tools [11-13]. This proposed prediction method uses receptance coupling substructure analysis (RCSA) theory to combine a range of analytic (modeled) tool responses with a single experimental FRF. While RCSA is a well-established theory first introduced in the 1960's [14], the details of its application to CNC chatter prediction are still in question. Preliminary research has utilized RCSA to approximate unknown machine characteristics through single tool-point FRF measurements [11].

Attempts are being made to address the technical difficulties of modal testing and to reduce the number of trials required to predict stability for a range of cutting tools. Researchers at the National Institute of Science and Technology (NIST) have developed a passive magnetic actuator device to predict 'best spindle speeds' [15] without need for modal testing. The device consists of permanent magnet that passively excites a rotating ferromagnetic machine tool. While the device is easy to set up and requires limited modal testing expertise, it cannot produce controllable excitation forces and thus cannot measure precise FRFs.

The research described in this thesis has two objectives: The first is to design and fabricate a non-contacting EMA actuator and sensor system that addresses the challenges and limitations of modal testing. The second aim is to develop 'inverse RCSA' and 'forward RCSA' software to predict dynamic characteristics (tool-point FRFs) for a range of machine tools based on information from a single battery of FRF measurements. The EMA actuator utilizes controllable magnetic reluctance forces to deliver accurately-shaped, high-magnitude forces to a milling center tool. This solution improves upon the passive magnetic excitation of the NIST device and enables more accurate FRF measurements. The EMA is designed to measure four force/displacement pairs (three independent) to fully characterize milling system dynamics. EMA system function is validated through comparisons with modal testing. The non-contacting EMA was conceptualized by Vulcancraft LLC and developed in collaboration with NCSU. Vulcancraft has a patent pending on the device [16].

This research also investigates the feasibility of modifying classical RCSA theory to predict a range of tool-point FRFs. The 'invRCSA' algorithm functions by decoupling three experimental displacement/force receptances (measured via non-contacting EMA) to characterize the FRF of the toolholder, spindle, and milling machine structure. These component FRFs are then combined

through classical RCSA theory with analytical models of milling tools to predict tool-point FRFs [10]. It is anticipated that these predicted tool-point FRFs can be converted into stability lobe diagrams to predict machine chatter. This adaptation of classical RCSA to tool-point FRF prediction was developed by Vulcancraft LLC which has a patent pending on the method [17].

## 2. Background: Machining Chatter

The earliest data related to vibration in milling was gathered by Salomon in the late 1920s [18]. In 1939, the American Society of Mechanical Engineers (ASME) correctly identified chatter as a result of interactions between cutting force and the natural modes of vibration of the cutting tool and work piece:

"It's severity undoubtedly is determined by the degree of resonance between periodic variations in the cutting force, and the natural frequencies of the work, and of the work and tool supporting structures" [19].

In 1946, Arnold used several simple yet successful measuring systems to record tool vibration and vertical cutting forces on a lathe. For both non-interference and interference cutting, he investigated the effects of tool sharpness, cutting speed, tool overhang, and feed rate on vibration amplitude and force. His careful experiments confirmed that chatter is not induced by external forces but by internal forces caused by the variations in the cutting process [20].

Following Arnold's early work, researchers focused on tool and workpiece interactions as well as dynamic responses of milling systems. Tobias noted in 1959 that chatter was not a result of interrupted cutting, but was due to what he termed "dynamic instability in the machine tool system" [21]. This slightly misleading dynamic instability terminology refers to cutting situations in which the internal forces generated by the dynamic cutting process overwhelm the inherent system damping. Damping of a milling system is due to many different effects ranging from the hysteretic/viscous damping of the distributed mass mill frame to chip thickness and penetration rate

[22]. Tobias was also one of the first to record that chatter occurring only in certain "chatter speed bands" [21]. During the 1960s, Tobias, Peters, and Tlusty published basic mathematical theories describing the closed loop nature of self-excited vibration. These theories, which assumed the cutting forces varied linearly with chip thickness and acted on the cutting tool in one direction, all were able to predict stability limits as a function of the chip thickness. The resulting 'stability lobe diagram' is a graphical representation of these equations. The diagram divides a cut depth vs spindle speed plot along a line where the summation of system damping is zero. Areas below the zero-damping line (which look like a series of interconnected arcs or 'lobes') are predicted to be dynamically stable while those above are unstable [22-25].

In 1965, Tobias published a thorough text titled *Machine-Tool Vibration* which covered vibration theory as well as machine tool chatter phenomena [22]. He correctly identified mode coupling and regeneration of waviness as the primary causes of regenerative chatter in milling. Also in 1965, Merritt published an important paper (one of a series by researchers at Cincinnati Machine Tool) in which he utilized a "chatter feedback loop" to create a cutting stability diagram. Merritt's application of control theory to chatter allowed straightforward calculations of stability borderlines for n-degree of freedom systems [5]. This solution however, as with all analytic solutions of the time, simplified the problem by neglecting important variations in cutting forces and directions.

## *2.1 Stability Lobe Diagrams*

While Merritt, Tobias, and other early metal machining researchers identified the existence of "lobed stability regions" (at very high spindle rpm) where stable cutting should theoretically be possible, they did not appreciate the importance of their find. The milling machines in the 1960s and 1970s could not achieve the required spindle speeds and power requirements to take advantage of these

hypothetical zones. In his innovative paper on feedback chatter theory, Merritt stated that, "…lobed borderlines of stability are progressively more difficult to compute, but fortunately, are progressively less important from a practice viewpoint" [5]. A generic stability lobe diagram is shown in Figure 2-1.

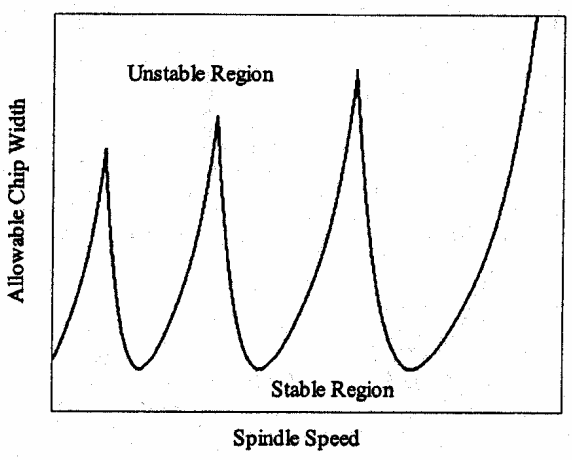


**Figure 2-1: Stability Lobe Diagram [26]**

Historically, milling operations were limited by power rather than spindle and tool dynamics (regenerative chatter). In recent years however, milling machines of exceptional speed (40,000rpm), power (40kW), and accuracy (0.0002in) have been developed. The aircraft industry in particular uses this HSM technology on aluminum components to substantially decrease machining time while maintaining part strength and surface finish. The benefits of HSM are real and measurable. Boeing uses HSM to produce the new F/A-18E/F fighter jet with 42% fewer parts than previous F/A-18 generations while increasing the aircraft dimensions by 25%. Regenerative chatter is now a significant obstacle to further growth of HSM. Researchers are attempting to formulate new methods of identifying and avoiding chatter [27].

## *2.2 Simulations*

Since the landmark research of Merritt and Tobias, many authors have used analytical methods to investigate stability limits, machine tool dynamics, and mechanics of the cutting process. In his 1981 paper, however, Tlusty contended that existing simulations did not take into account the complicating peculiarities of the milling process: "Not enough has been done yet to properly understand chatter in milling with its periodically interrupted cutting process" [28]. His paper identified characteristics unique to the milling process: damping and stiffness variations with cutting frequency, chip thickness and cutting force variations, and regenerative and forced vibration interactions. Tlusty proposed an iterative vibration simulation program based on the assumed direct proportionality between cutting force and chip cross section ($F_T = k_S bh$). Ironically, his proposed time-domain model did not take into account the earlier-mentioned 'complicating peculiarities' of the cutting process.

To include all significant process dynamics, researchers developed more complex time domain simulation methods [7]. Smith and Tlusty reviewed five of the most common milling process models in 1991 [26]. Iterative time domain cutting simulations, such as the one included in Tlusty's latest text [4], are quite sophisticated. Tlusty's simulation, which bears much resemblance to the code described in his 1983 paper, outputs time domain tool displacement data for a wide range of machining conditions. Steady or decaying amplitude time responses indicate steady cutting conditions, while exponentially growing vibrations signify unstable chatter conditions [4]. Yusef Altintas is currently regarded as an authority in the field of machining modeling software. His *Manufacturing Automation Laboratory Inc* markets the *CUTPRO*© software package [29]. This package, which uses time domain simulation techniques as well as advanced analytical solutions, is capable of

producing 3-D stability diagrams, predicting surface finish and tool motion, and outputting cutting force values for three dimensions. Available add-on packages allow for experimental impact hammer data to be used as inputs for prediction and modeling.

Other researchers have attempted to mathematically describe the behavior of milling systems by incorporating feedback theory, modal analysis, iterative time domain simulations, and analytical models with varying degrees of success. While the capabilities and accuracy of these solution methods have improved, the quality of the computational output remains sensitive to the accuracy of input parameters.

## *2.3 Experimental Techniques*

### *2.3.1 In-Situ Control*

Considerable time and money has been spent developing in-situ chatter control systems. Many of these proposed methods for detecting and avoiding chatter are based on adaptive or feedback control theory [30-32]. Controlling the spindle speed of a milling machine in real time, however, requires precise sensors and a data acquisition system capable of very high sampling rates. In 1975, Weck utilized spindle-mounted strain gauges to measure spindle torque and thereby cutting force. This setup allowed for better frequency response than earlier dynamometers but required slip rings on the spindle to transmit the data [30]. During the past five years, Smith and Delio have developed a working system that uses audio signals to detect and control chatter [8]. A software package employing this method of chatter detection and avoidance is currently marketed by Manufacturing Laboratories Inc (MLI) as the "Harmonizer®" [33]. The system monitors the cutting process through a directional microphone and will indicate whether or not chatter exists. The chatter

regognition and control "CRAC" program will suggest alternate (chatter-free) spindle speeds if chatter exists. Some work has also been done in the area of using active control to reduce spindle vibration. A 1999 paper describes a "proof of concept" active toolholder device that imparts vibratory forces to the spindle to cancel out resonant cutting forces. The paper claims a factor of five improvement in surface finish over the uncontrolled system [34].

Although much progress has been made in the field of in-situ chatter detection and control, these methods are inherently limited to react to the occurrence of chatter. This fundamental limitation requires the user to make several rehearsal cuts to find the best cutting conditions before machining a critical tolerance part.

### *2.3.2 A-Priori Prediction*

The FRF required by most a-priori prediction methods can be mathematically defined as the Fourier transform of the output response (displacement of the tool) divided by the Fourier transform of the input data (excitation force applied to the tool) [6]. The experimental determination of a system's FRF, a process known as modal testing, involves three steps. First, a wideband excitation force (one containing a wide range of frequencies) is applied to the system. Impulsive and periodic force profiles are most commonly utilized in modal testing [35]. Impact hammers equipped with force transducers are for impulse testing while hydraulic and electromechanical shakers are often required to create periodic forces across large frequency ranges. Piezo-electric transducers (force sensors and accelerometers) are frequently often utilized to record excitation forces and acceleration responses. Finally, time domain data is transformed to the frequency domain via Fourier analysis techniques. The modal behavior of the system can then be graphically displayed by plotting the FRF

of the output displacement divided by input force (the system compliance), output velocity over input force (the system mobility), or output acceleration over input force (the system inertance) [6].

# 3. Receptance Coupling Substructure Analysis (RCSA)

## *3.1 Overview*

Receptance coupling substructure analysis (RCSA) is a method used to determine the frequency response of a compound linear elastic structure when the frequency responses (receptances) of each system subcomponent are known. Early work by Bishop and Johnson [14] described the utility of RCSA in determining closed-form algebraic expressions for displacement and slope at any point along a beam with a known input force or moment. The authors recognized that simple linear relations (receptances) between inputs and outputs could be used to analytically 'combine' the responses of simple linear components into a compound system response.

The research presented in this thesis utilizes a variation of the RCSA technique to analytically decouple the dynamics of a CNC milling system into component tool and spindle responses. The spindle receptance information garnered through this 'inverse RCSA' approach can then be re-coupled through traditional 'forward RCSA' to predict the response of any analytically modeled end mill. This approach yields full knowledge of compound tool and spindle frequency responses for a range of tool geometries.

The receptance of any linear system can be represented as a transfer function relating the output (displacement or slope) to the input (applied force or moment). Thus, the receptance is simply the frequency-dependent compliance of a linear system. The receptance ($\alpha$) of a linear single-input, single-output (SISO), spring mass system (Figure 3-1) can be derived from its equation of motion:

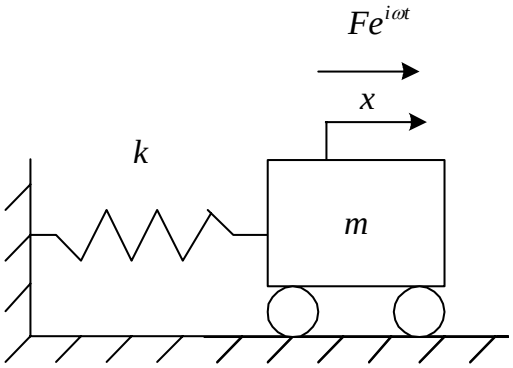


**Figure 3-1: Linear spring mass system**

$$
\begin{aligned}
&m\ddot{x}(t) + kx(t) = Fe^{i\omega t} \\
&-m\omega^2 X(i\omega) + kX(i\omega) = F \\
&\alpha = \frac{X(i\omega)}{F(i\omega)} = \frac{1}{k - m\omega^2}
\end{aligned}
\qquad (3.1).
$$

Bishop and Johnson categorized receptances as being either *direct* receptances (displacement and force at the same point) or *cross* receptances (force and resulting displacement at different points), and used subscripts for identification:

$$
\begin{array}{r}
\alpha_{XY} \\
\text{Measured Displacement} \longrightarrow \\
\text{Applied Force} \longrightarrow
\end{array}
\qquad (3.2)
$$

The relations between applied forces and resulting displacements/slopes at the ends of uniform beams with known boundary conditions are tabulated in Bishop and Johnson's text as 'tip receptances'. These tip receptances are simply algebraic expressions for the deflection and slope frequency responses of a simple beam. For reference, the tip receptance for a cantilever beam can be expressed [14]:

$$\alpha_{LL} = \frac{-\cos(\lambda L)\sinh(\lambda L) + \sin(\lambda L)\cosh(\lambda L)}{EI\lambda^3(\cos(\lambda L)\cosh(\lambda L) - 1)}$$
$$\lambda^4 = \frac{\omega^2 A\rho}{EI} \tag{3.3}$$

Where:

$\omega =$ frequency $(\text{rad/sec})$

$A =$ cross-sectional area $(\text{m}^2)$

$\rho =$ density $\left(\text{kg}/\text{m}^2\right)$

$E =$ elastic modulus $(\text{GPa})$

$I =$ area moment of inertia $(\text{m}^4)$

$L =$ length $(\text{m})$

The utility of the RCSA technique is the straightforward algebraic coupling or 'substructuring' procedure. Using RCSA, the dynamics of a compound linear system can be analyzed by combining receptances of known (tabulated) subcomponents. In order to produce a compound system response, RCSA requires boundary conditions and receptance information at connection coordinates.

### *3.1.1 Inverse RCSA*

A logical modification to the forward RCSA procedure is to measure the compound receptance of a linear system and use this information to predict the receptance of one subcomponent. As noted earlier, forward RCSA requires component FRF measurements at each coupling point. Inverse RCSA requires FRFs for the compound system and all but one subcomponent. This can be done experimentally or analytically (by using closed form receptance terms from Bishop and Johnson as in the following simulation). System boundary and compatibility conditions must be recorded at each

interconnection point. Algebraic coupling equations relating internal and external coordinates (forces and displacements in the following simulation) are then generated from known receptances and boundary conditions. The equations are then solved simultaneously, relating known subcomponent receptances to known system excitation and responses. This solved subcomponent receptance can then be combined through forward RCSA with other known subsystem receptances to predict compound system responses. The inverse/forward RCSA FRF prediction method is demonstrated in the following simulations.

## *3.2 Mass Spring Damper Simulations*

To demonstrate the utility of inverse RCSA for compound linear systems, the dynamics of a simple 2 DOF mechanical system (a double mass, spring, damper or MSD) of (Figure 3-2) were analyzed. The equations of motion for this system were derived using Newton's second law of motion:

$$\begin{aligned} m_1\ddot{x}_1 &= F_1 - k_1(x_1 - x_2) - b_1(\dot{x}_1 - \dot{x}_2) \\ m_2\ddot{x}_2 &= -k_2 x_2 - b_2\dot{x}_2 - k_1(x_2 - x_1) - b_1(\dot{x}_2 - \dot{x}_1) \end{aligned} \tag{3.4}$$

A Simulink™ program was developed to analyze the dynamics of this linear system (Figure 3-3). System parameters ($m_1 = 1.0\,kg$, $b_1 = 5\,kg/s$, $k_1 = 1.2\times10^5\ N/m$, $m_2 = 10\,kg$, $b_2 = 25\,kg/s$, and $k_2 = 4\times10^5\ N/m$) were chosen to yield lightly-damped resonances at 30 Hz and 60 Hz. The need for very accurate FRFs necessitated a high-order solver with a small time step, thus an ODE-5 Dormand-Prince solver with a fixed time step of $10.0\,\mu s$ was chosen.

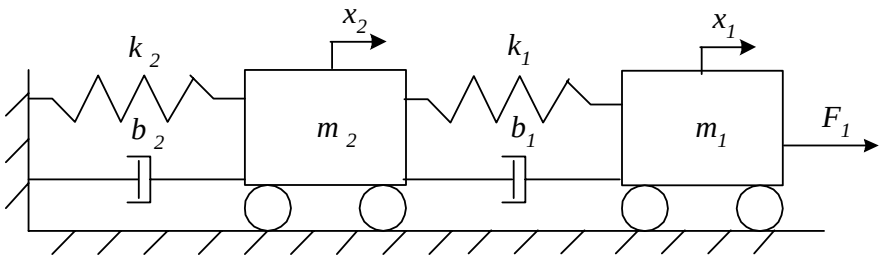


**Figure 3-2: Linear, 2 DOF Mass Spring Damper System**

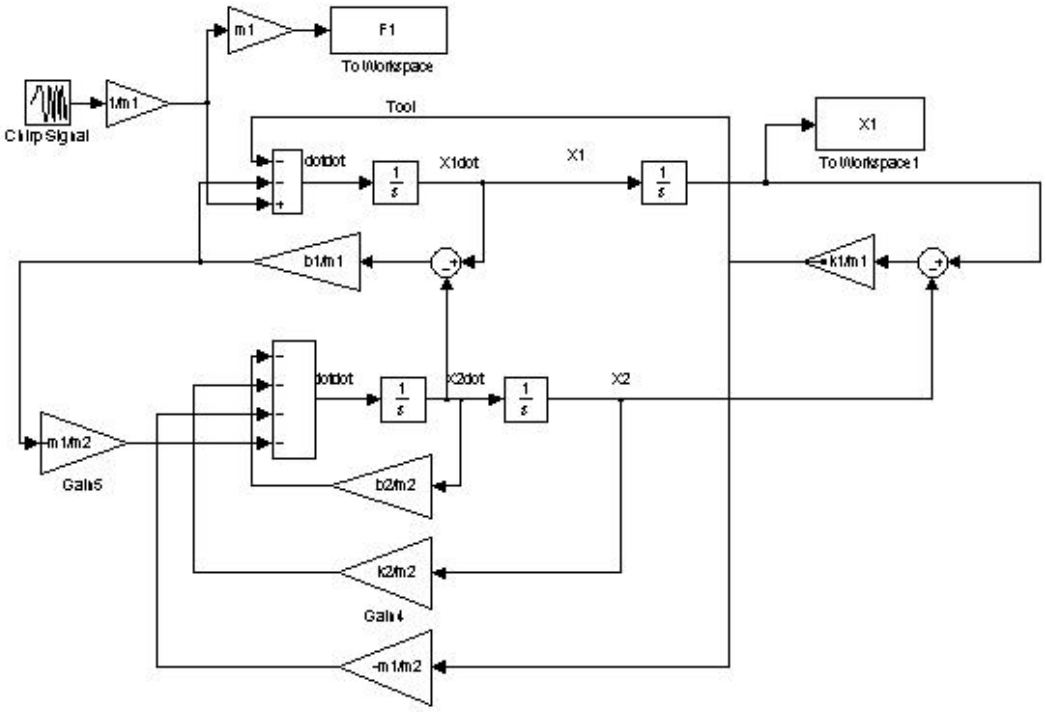


**Figure 3-3: Simulink Model for the Double MSD System**

The simulated frequency response for this double MSD system, shown in Figure 3-4, reveals natural frequencies at approximately 30 Hz and 60 Hz.

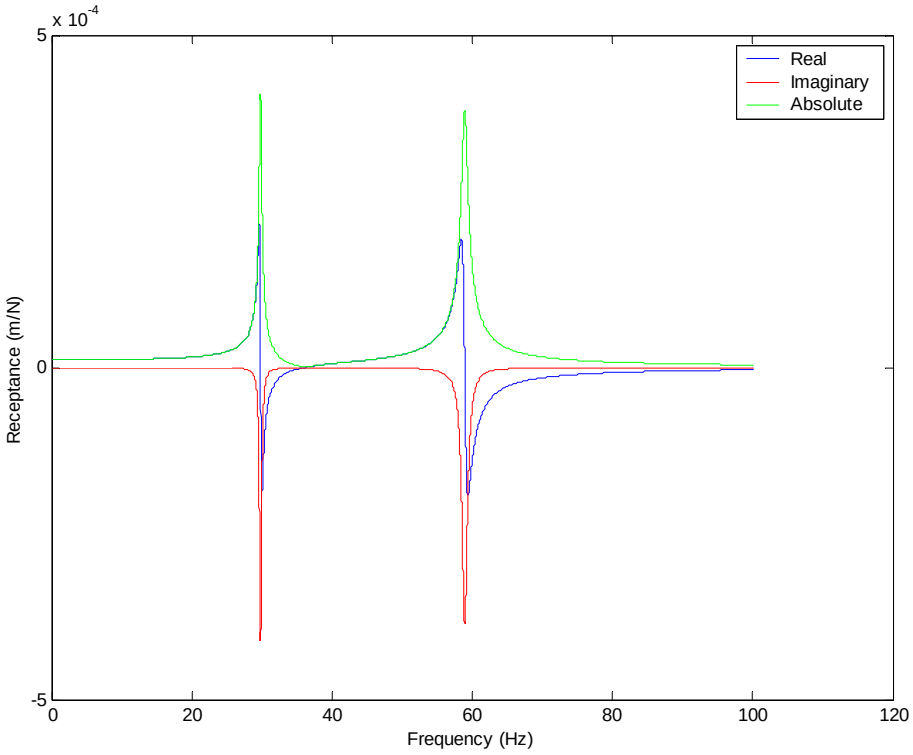


**Figure 3-4: $X_1/F_1$ Frequency Response for the Double MSD System**

The RCSA process consists of several steps, as highlighted in the following inverse and forward RCSA flowcharts (Figure 3-5 and Figure 3-6, respectively). The receptance of Subsystem 1 (consisting of spring 1 and mass 1) was assumed to be known, while the receptance of Subsystem 2 (consisting of spring 2 and mass 2) was assumed to be unknown but predictable from the simulation data. A known input force $F_1$ was applied to mass $m_1$ and time-domain responses were recorded. The time-domain force and displacement data was transformed to the frequency domain via Matlab's Fast Fourier Transform (FFT) command to produce the system FRF. Inverse RCSA was then applied to decouple the known dynamics of Subsystem 1 from the compound response and identify the dynamics of Subsystem 2.

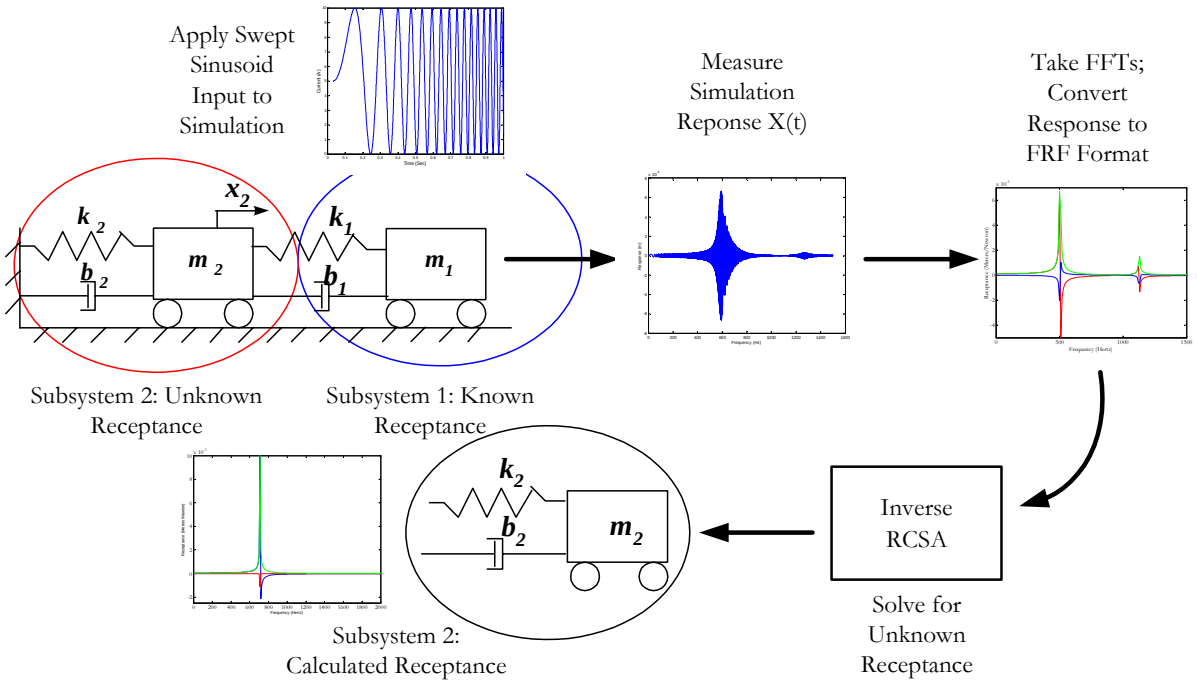


**Figure 3-5: Inverse RCSA Flowchart: Double Spring Mass Damper Simulation**

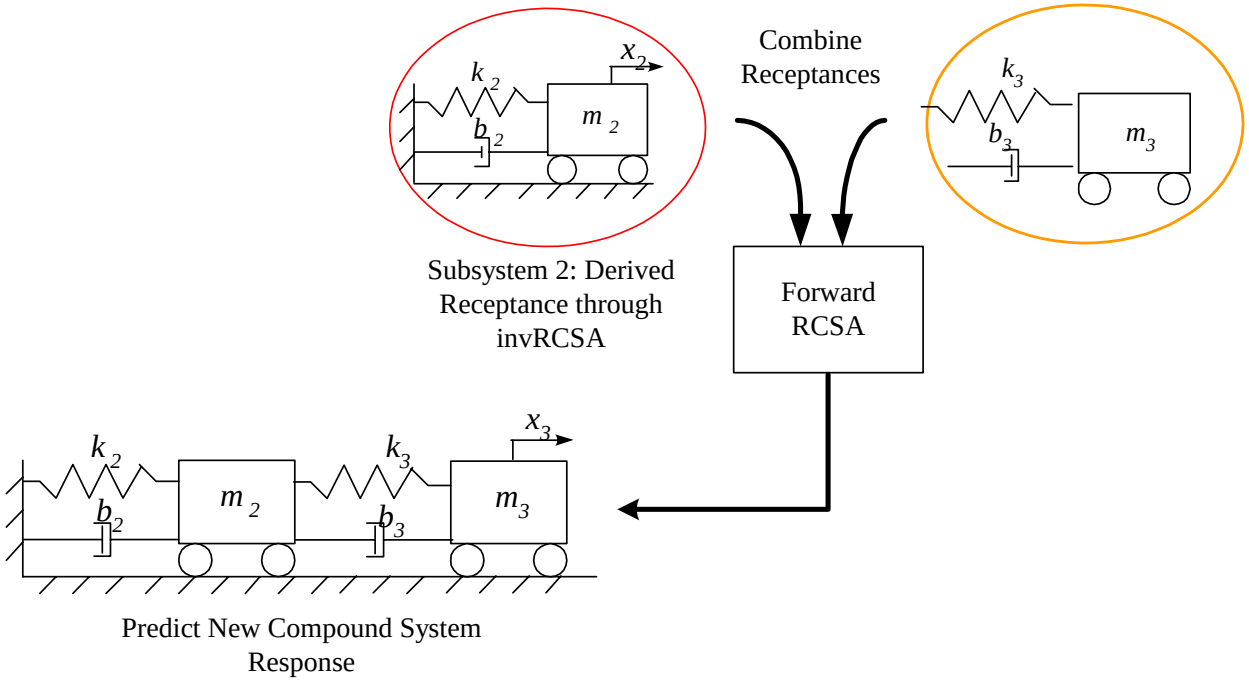


**Figure 3-6: Forward RCSA Flowchart: Double Spring Mass Damper Simulation**

Once the receptance for Subsystem 2 was identified, it was then coupled (via forward RCSA) to a different spring mass system (analytically modeled Subsystem 3). The FRF of this 'new' compound system was then compared to an analytic model of the compound system. Details of all RCSA simulations are presented in the following sections.

### *3.2.1 Solving for Subsystem 1 Receptance*

The 2 DOF system (Equation 3.4) was excited using a swept sinusoid forcing function applied at $m_1$, with frequencies varying linearly from 1 to 1000 Hz (Figure 3-7). Forcing functions of this type are commonly used in modal analysis, as they provide the wideband excitation needed for identification. The input force $F_1(t)$ and system response $x_1(t)$ were assumed known, while internal forces $f_2(t)$ and $f_3(t)$ and internal displacements $x_2(t)$ and $x_3(t)$ were assumed unknown.

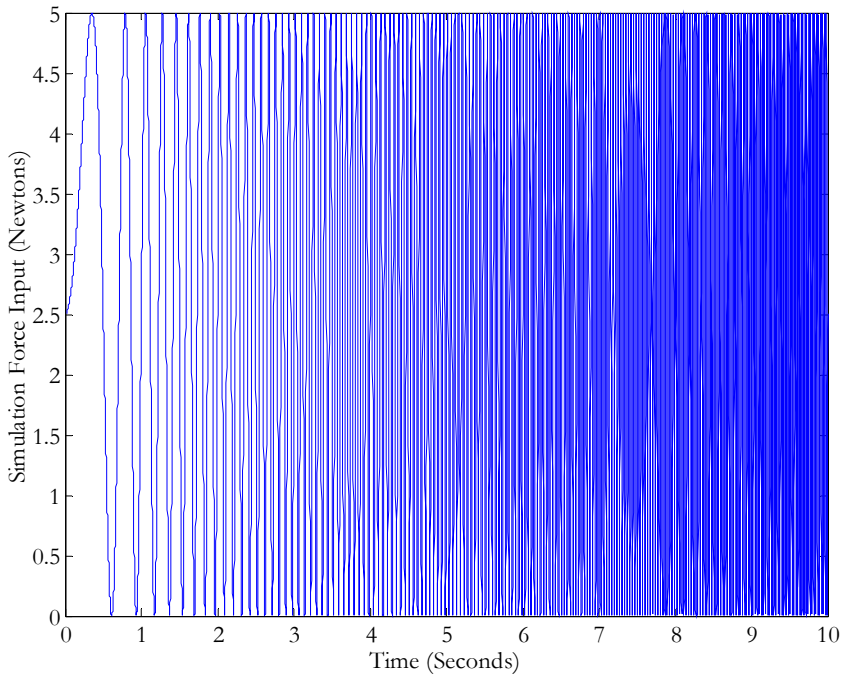


**Figure 3-7: Swept Sinusoid Force Profile**

RCSA solutions (forward and inverse) require boundary conditions and compatibility information related to the subsystems. To assist in specifying this information, Figure 3-8 shows this compound system modeled as two subsystems.

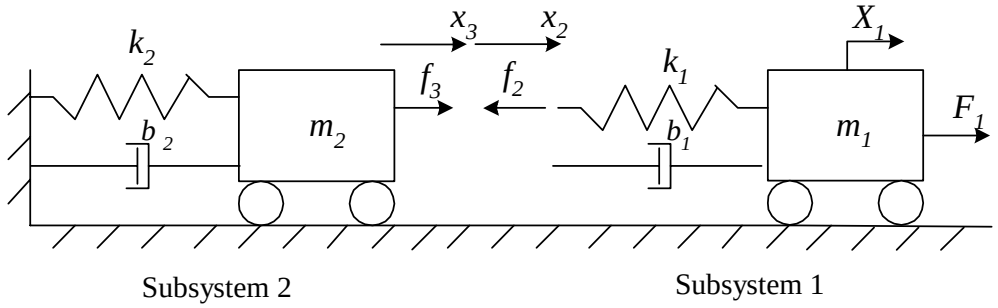


**Figure 3-8: Double MSD System Modeled as Two Subsystems**

The boundary and compatibility conditions associated with these subsystems are:

$$\begin{aligned} &\textit{Boundary Conditions :} \quad x2 = x3 \\ &\textit{Compatibility Conditions :} \quad f2 + f3 = 0 \end{aligned} \tag{3.5}$$

The receptances for Subsystem 1 were derived from the equations of motion (3.4), but are also compiled in Bishop and Johnson's *Mechanics of Vibration* text:

$$\begin{aligned} \alpha_{11} &= -\frac{1}{m_1\omega^2} \qquad \alpha_{12} = -\frac{1}{m_1\omega^2} \\ \alpha_{21} &= -\frac{1}{m_1\omega^2} \qquad \alpha_{22} = \frac{1}{k_1 - b_1\omega} - \frac{1}{m_1\omega^2} \end{aligned} \tag{3.6}$$

Algebraic coupling equations linking measured forces and displacements to unknown internal forces and displacements were then generated. For the 2 DOF compound system of Figure 3-8, the applied force F(t) and the compound system response $X_1(t)$ are measured variables while internal displacements $x_2(t)$ and $x_3(t)$ and internal forces $f_2(t)$ and $f_3(t)$ can be determined via the coupling equations:

$$\begin{aligned} X_1 &= \alpha_{11} F_1 + \alpha_{12} f_2 \\ x_2 &= \alpha_{21} F_1 + \alpha_{22} f_2 \\ x_3 &= \alpha_{33} f_3 \end{aligned} \tag{3.7}$$

Next, the unknown component receptance ( $\alpha_{33}$) was algebraically solved in terms of the known receptances ($\alpha_{11}, \alpha_{12}, \alpha_{21}, \alpha_{22}$), known response $x_1(t)$, and known input force $F_1(t)$.

$$\begin{aligned} f_3 &= -f_2 = \frac{\alpha_{11} F_1 - X_1}{} \\ x_3 &= x_2 = \alpha_{21} F_1 - \frac{\alpha_{22}\alpha_{11} F_1 - \alpha_{22} X_1}{\alpha_{12}} \\ \alpha_{33} &= \frac{x_3}{f_3} = -\alpha_{22} - \frac{\alpha_{21}^{\,2}}{\frac{X_1}{F_1} - \alpha_{11}} \end{aligned} \tag{3.8}$$

The identified receptance of Subsystem 2 ($\alpha_{33}$, Figure 3-9), has a resonance of similar size and shape to the first resonance of the compound system (Figure 3-4). This similarity is expected because the 'identified subsystem' is simply the first MSD of the double MSD system with linear dynamics.

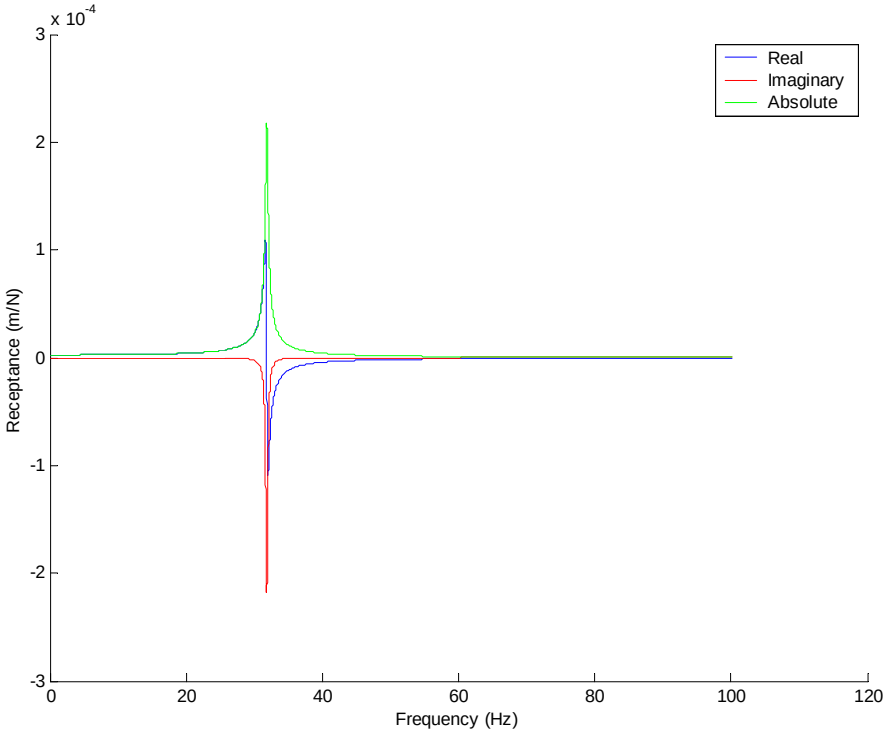


**Figure 3-9: Identified Subsystem 2 Receptance**

### 3.2.2 *Predicting Compound Receptance*

The identified receptance $\alpha_{33}$ was then coupled to a new linear subsystem ($m_3 = 1.75\,kg$, $k_3 = 1\times10^5\ N/m$, and $b_3 = 10\,kg/s$), as shown in Figure 3-10. The boundary conditions, compatibility conditions, and internal states are related:

$$\begin{aligned} &\textit{Boundary Conditions}: && x_2 = x_3 \\ &\textit{Compatibility Conditions}: && f_2 + f_3 = 0 \end{aligned} \tag{3.9}$$

$$
\begin{aligned}
X_1 &= \alpha_{11} F_1 + \alpha_{12} f_2 \\
x_2 &= \alpha_{21} F_1 + \alpha_{22} f_2 \\
x_3 &= \alpha_{33} f_3
\end{aligned}
\tag{3.10}
$$

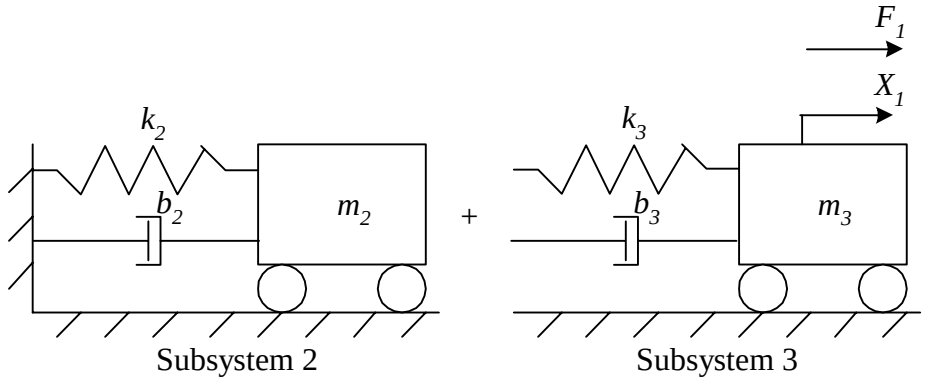


**Figure 3-10: Forward RCSA: Combining Identified Subsystem 2 with Subsystem 3**

Equations 3.9 and 3.10 were then used to predict the compound receptance:

$$
\begin{aligned}
f_2 &= \frac{-\alpha_{21} F_1}{\alpha_{33} + \alpha_{22}} \\
X_1 &= \alpha_{11} F_1 + \frac{-\alpha_{21} F}{\alpha_{33} + \alpha_{22}} \alpha_{12} \\
\frac{X_1}{F_1} &= \alpha_{11} - \frac{\alpha_{12} \alpha_{21}}{\alpha_{33} + \alpha_{22}}
\end{aligned}
\tag{3.11}
$$

The accuracy of this predicted compound receptance (plotted in Figure 3-11) can be assessed by comparing it to the analytic compound response (Figure 3-12).

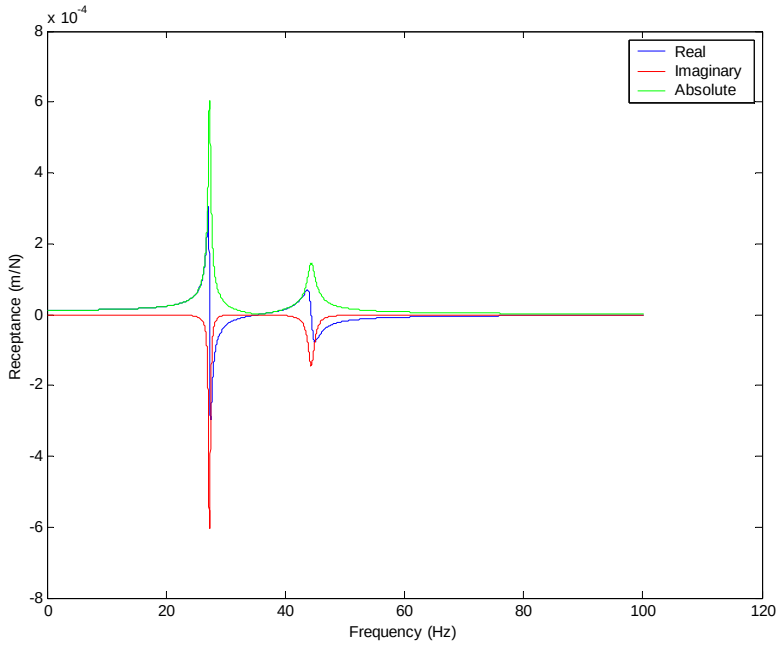


**Figure 3-11: Predicted Compound Receptance: Double SMD Simulations**

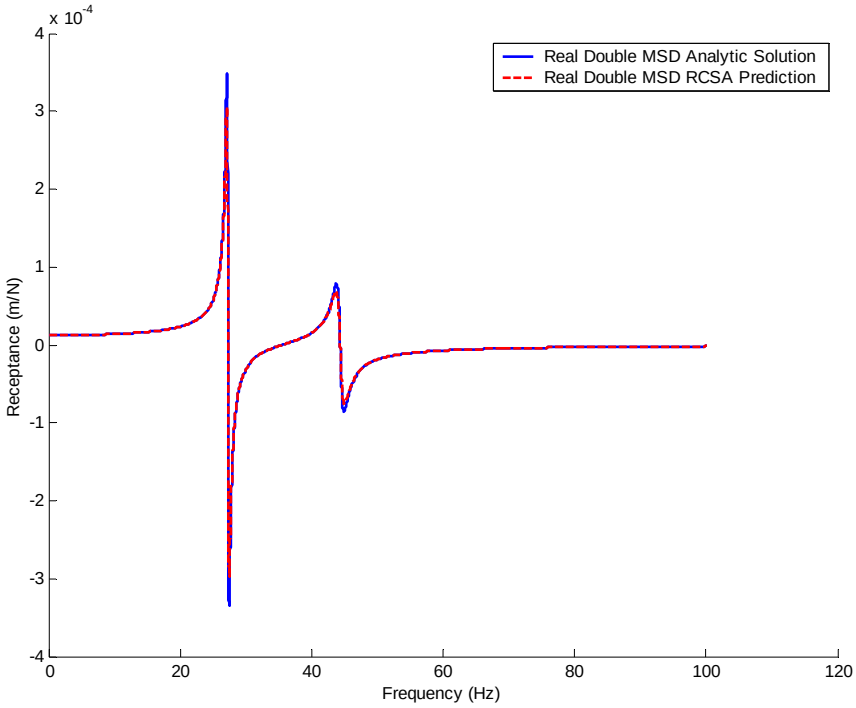


**Figure 3-12 Predicted vs. Analytical Compound Receptances: Double SMD Simulations**

While these receptances appear to be identical, small errors are present near the resonance peaks. These discrepancies result from numerical inaccuracies in the simulation and the conversion of time-domain responses to the frequency domain. These errors will be discussed in Section 7.

# 4. Tool-point FRF Prediction using RCSA

The primary goal of this research is to predict tool-point FRFs for a collection of tools in a high speed milling machine by measuring a single set of compound receptances. Each tool-point FRF includes coupled responses of the tool, toolholder, spindle, and machine structure. The approach used to predict these FRFs is the same as that used in the MSD example: unknown component receptances are identified using inverse RCSA, and compound receptances are predicted using these components with forward RCSA. Unlike the MSD simulations, however, this approach involves compound cantilever beams and requires multiple receptance measurements. This is true because input forces (or moments) are coupled to both translation and slope responses. As a result, the machine, spindle, and toolholder coupling equations contain three unknown receptances which must be determined experimentally.

## *4.1 Identifying Toolholder Receptance*

The inverse RCSA strategy presented here replicates the theory developed by Esterling [10]. This approach uses three independent force/translation receptance measurements taken at Locations 1 and 2 on the tool (Figure 4-1). These measurements are ultimately used to solve for the unknown receptances of the toolholder, spindle, and machine structure. Figure 4-2 shows internal displacements and reaction forces/moments resulting from toolpoint excitation $(F_1)$.

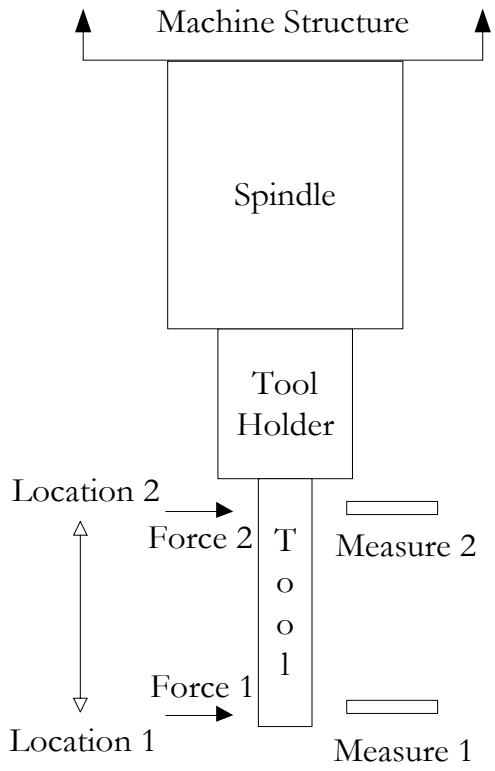


**Figure 4-1: Excitation and Measurement Locations for Experimental Tool-point FRFs**

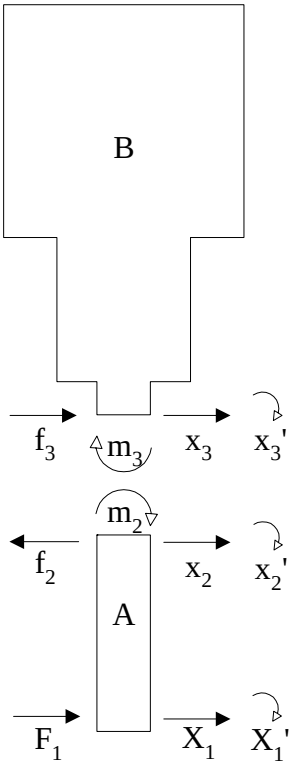


**Figure 4-2: Internal Displacements and Reactions Resulting from Applied Force F1**

RCSA theory requires that cross receptances exhibit 'reciprocity' (reversing the order of subscripts does not change their value). Thus, only three of these measured receptances (Equation 4.1) will be unique, as $\alpha_{21}$ and $\alpha_{12}$ are theoretically equal.

$$\begin{aligned} \alpha_{11} &= \frac{X_1}{F_1} \\ \alpha_{12} &= \frac{X_1}{F_2} \\ \alpha_{21} &= \frac{X_2}{F_1} \\ \alpha_{22} &= \frac{X_2}{F_2} \end{aligned} \tag{4.1}$$

Analytical receptances for tool blanks (uniform beams of length L) with free-free boundary conditions are listed below [14].

$$
\begin{aligned}
\alpha_{22} &= \frac{-\cos(\lambda L)\sinh(\lambda L)+\sin(\lambda L)\cosh(\lambda L)}{EI\lambda^3(\cos(\lambda L)\cosh(\lambda L)-1)} \\
\alpha_{2'2} &= \alpha_{22'} = \frac{-\sinh(\lambda L)\sin(\lambda L)}{EI\lambda^2(\cos(\lambda L)\cosh(\lambda L)-1)} \\
\alpha_{12} &= \alpha_{21} = \frac{\sin(\lambda L)-\sinh(\lambda L)}{EI\lambda^3(\cos(\lambda L)\cosh(\lambda L)-1)} \\
\alpha_{1'2} &= \alpha_{21'} = \frac{\cos(\lambda L)-\cosh(\lambda L)}{EI\lambda^2(\cos(\lambda L)\cosh(\lambda L)-1)} \\
\alpha_{2'2'} &= \frac{\cos(\lambda L)\sinh(\lambda L)+\sin(\lambda L)\cosh(\lambda L)}{EI\lambda(\cos(\lambda L)\cosh(\lambda L)-1)} \\
\alpha_{12'} &= \alpha_{2'1} = \frac{-\cos(\lambda L)+\cosh(\lambda L)}{EI\lambda^2(\cos(\lambda L)\cosh(\lambda L)-1)} \\
\alpha_{1'2'} &= \alpha_{2'1'} = \frac{\sin(\lambda L)+\sinh(\lambda L)}{EI\lambda(\cos(\lambda L)\cosh(\lambda L)-1)} \\
\alpha_{11} &= \frac{-\cos(\lambda L)\sinh(\lambda L)+\sin(\lambda L)\cosh(\lambda L)}{EI\lambda^2(\cos(\lambda L)\cosh(\lambda L)-1)} \\
\alpha_{1'1} &= \alpha_{11'} = \frac{\sin(\lambda L)\sinh(\lambda L)}{EI\lambda^2(\cos(\lambda L)\cosh(\lambda L)-1)} \\
\alpha_{1'1'} &= \frac{\cos(\lambda L)\sinh(\lambda L)+\sin(\lambda L)\cosh(\lambda L)}{EI\lambda^2(\cos(\lambda L)\cosh(\lambda L)-1)}
\end{aligned}
\tag{4.2}
$$

where:

$$\lambda = \left(\frac{\omega^2 A\rho}{EI}\right)^{\frac{1}{4}}$$

$\omega = Frequency\ (rad/sec)$

$A = Cross\ Sectional\ Area\ of\ Beam$

$\rho = Density\ of\ Beam$

$E = Young's\ Modulus$

$I = Moment\ of\ Inertia$

As in the MSD simulation examples, inverse RCSA algebra begins with the definition of boundary and compatibility conditions:

$$\begin{aligned} &\textit{Boundary Conditions :} && x_2 = x_3 \\ & && x_{2'} = x_{3'} \\ &\textit{Compatibility Conditions :} && f_2 + f_3 = 0 \\ & && m_2 + m_3 = 0 \end{aligned} \tag{4.3}$$

Six algebraic coupling equations relate known forces $(F_1, F_2)$ and measured displacements $(X_1, X_2)$ to unknown internal forces and moments $(f_2, f_3, m_2, m_3)$, unmeasured tip rotations $(X_{1'}, X_{2'})$, and undetermined coupling receptances $(B_1, B_2, B_3)$:

$$\begin{aligned} X_1 &= \alpha_{LL} F_1 - \alpha_{L0} f_2 - \alpha_{L0'} m_2 && [a] \\ X_2 &= -\alpha_{00} f_2 + \alpha_{00'} m_2 + \alpha_{0L'} F_1 && [b] \\ X_{1'} &= -\alpha_{L'L} F_1 + \alpha_{L'0'} m_2 - \alpha_{L'0} f && [c] \\ X_{2'} &= \alpha_{0'0} f_2 - \alpha_{0'L} F_1 + \alpha_{0'0'} m_2 && [d] \\ X_3 = X_2 &= B_1 f_3 + B_2 m_3 && [e] \\ X_{3'} = X_{2'} &= B_2 f_3 + B_3 m_3 && [f] \end{aligned} \tag{4.4}$$

The B receptances $(B_1, B_2, B_3)$ describe the dynamics of subsystem B; finding all three in closed form is the objective of this exercise. By applying a swept sinusoidal input force at the tool tip (Location 1 of Figure 4-2) and measuring displacements at locations 1 and 2, the first two receptances ($\frac{X_1}{F_1}$ and $\frac{X_2}{F_1}$) are calculated. Equations 4.4 (*a-d*) can be inverted to solve for $f_2$ and $m_2$:

$$f_2 = \frac{\alpha_{00'}\left(X_1 - \alpha_{LL}F_1\right) - \alpha_{L0'}\left(X_1 - \alpha_{0L}F_1\right)}{-\alpha_{L0}\left(X_2 - \alpha_{0L'}F_1\right) + \left(\alpha_{L0'}\alpha_{00}\right)}$$
$$m_2 = \frac{-\alpha_{L0}\left(X_2 - \alpha_{0L'}F_1\right) - \alpha_{00}\left(X_1 - \alpha_{LL}F_1\right)}{\alpha_{00}\alpha_{L0} - \alpha_{L0}\alpha_{00}} \tag{4.5}$$

Using the prescribed boundary and compatibility conditions (Equation 4.3), Equation 4.4*b* can be equated to 4.4*e*, and 4.4*d* can be equated to 4.4*f*. The resulting equations relate solved internal forces and moments ( $f_2$ and $m_2$) and known free-free boundary condition receptances to the unknown B receptances.

$$X_2 = -\alpha_{00}f_2 + \alpha_{00'}m_2 + \alpha_{0L'}F_1 = -B_1 f_2 - B_2 m_2$$
$$X_{2'} = \alpha_{0'0}f_2 - \alpha_{0'L}F_1 + \alpha_{0'0'}m_2 = -B_2 f_2 - B_3 m_2 \tag{4.6}$$

A third unique equation involving $B_1$ and $B_2$ or $B_2$ and $B_3$ must be used with (Equation 4.6) to solve for all three unknowns. This third relation comes from measured tool-point receptances $\frac{X_1}{F_2}$ and $\frac{X_2}{F_2}$ resulting from an applied swept sinusoidal input force at Location 2 (Figure 4-3):

$$\tilde{X}_1 = \alpha_{L0}F_2 - \alpha_{L0}\tilde{f}_2 - \alpha_{L0'}\tilde{m}_2 \qquad [a]$$
$$\tilde{X}_2 = -\alpha_{00}\tilde{f}_2 + \alpha_{00'}\tilde{m}_2 + \alpha_{00}F_2 \qquad [b]$$
$$\tilde{X}_{1'} = \alpha_{L'0}F_2 + \alpha_{L'0'}\tilde{m}_2 - \alpha_{L'0}\tilde{f}_2 \qquad [c]$$
$$\tilde{X}_{2'} = -\alpha_{0'0}\tilde{f}_2 + \alpha_{0'0}\tilde{F}_2 + \alpha_{0'0'}\tilde{m}_2 \qquad [d]$$
$$\tilde{X}_3 = B_1\tilde{f}_3 + B_2\tilde{m}_3 \qquad [e]$$
$$\tilde{X}_{3'} = B_2\tilde{f}_3 + B_3\tilde{m}_3 \qquad [f] \tag{4.7}$$

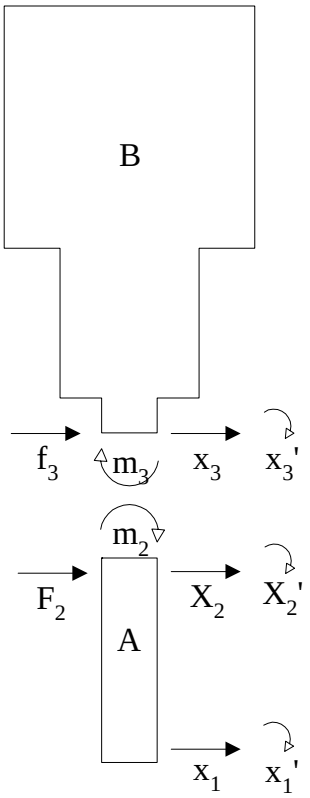


**Figure 4-3 External Force Applied to Tool at Location 2; Internal Reactions Shown**

As before, Subsystem A equations (those involving $X_1$ and $X_2$) can be used to solve for internal forces and moments ($\tilde{f}_2, \tilde{m}_2$). The tilda overbar indicates these measured displacements and internal forces are generated by force applied at Location 2 – they are different than the internal forces generated by external force at Location 1.

$$\tilde{f}_2 = \frac{\alpha_{00'}\left(\tilde{X}_1 - \alpha_{L0}F_2\right) + \left(\alpha_{L0}\tilde{X}_2 - \alpha_{00}\tilde{F}_2\right)}{-\left(\alpha_{00'}\alpha_{L0}\right) + \left(\alpha_{L0'}\alpha_{00}\right)}$$
$$\tilde{m}_2 = \frac{[\alpha_{L0}(\alpha_{00}\tilde{F}_2 - \tilde{X}_2) + \alpha_{00}(\tilde{X}_1 - \alpha_{00}\tilde{F}_2)]}{-[(\alpha_{L0}\alpha_{00'}) + (\alpha_{:L0'}\alpha_{00})]} \quad (4.8)$$

Combining equations 4.7*b* and 4.7*e* (or 4.7*c* and 4.7*f*) produces two equations (one independent equation) relating unknowns $B_1$ and $B_2$ to measured response ($\tilde{X}_2 / \tilde{F}_2$) and known receptances.

$$\begin{aligned} \tilde{X}_2 &= -\alpha_{00}\tilde{f}_2 + \alpha_{00'}\tilde{m}_2 + \alpha_{00}F_2 = B_1\tilde{f}_2 + B_2\tilde{m}_2 \\ \tilde{X}_{2'} &= -\alpha_{0'0}\tilde{f}_2 + \alpha_{0'0}\tilde{F}_2 + \alpha_{0'0'}\tilde{m}_2 = B_2\tilde{f}_2 + B_3\tilde{m}_2 \end{aligned} \tag{4.9}$$

Together, Equations 4.6 and 4.9 relate known system forces and displacements to the unknown system receptances $B_1$, $B_2$ and $B_3$. The expressions for $B_1$, $B_2$ and $B_3$ are complicated. It is important to note, however that they are linear relations easily evaluated numerically. The B-system receptances describe the frequency responses at the selected coupling point to input forces or moments. $B_1$ represents the tool/toolholder interface displacement-force receptance ($x_3/f_3$). $B_2$ describes the interface displacement resulting from applied moment $(x_3/m_3)$ or equivalently, the slope resulting from applied force $(x_{3'}/f_3)$. The third and final independent subsystem receptance $B_3$ describes the interface slope resulting from applied moment $(x_{3'}/m_3)$.

This inverse RCSA method uses four tool FRFs (three independent) to completely characterize the dynamics of the CNC structure, spindle, and toolholder. Recent work by Schmitz and Burns [36] presents a similar RCSA strategy for predicting tool-point frequency response. However, their work does not include a direct method of solving for the three unknown receptances $(B_1, B_2, B_3)$. Instead, they attempt a best-fit approximation of toolholder dynamics by measuring a single spindle receptance and then conducting a series of tests with tools of variable lengths. This approximate method creates errors in the predictions. A recent patent application [10] by Vulcancraft LLC

compares RCSA predictions made through the best-fit technique and the RCSA algorithm described in this thesis.

## *4.2 Predicting Tool-point (Compound) FRFs*

In order to predict tool-point FRFs for a variety of tools, the identified B receptances must be combined with appropriate free-free tool FRFs. As noted earlier, milling tool frequency responses can be approximated using tabulated tip receptances for uniform Bernoulli-Euler beams with free-free boundary conditions [14]. The following derivation closely follows the work of Schmitz and Burns [36] and of Esterling [10]. Again, the RCSA solution requires boundary conditions, compatibility conditions, and subsystem coupling equations:

$$\begin{aligned} X_2 &= X_3 \\ X_{2'} &= X_{3'} \\ f_2 + f_3 &= 0 \\ m_2 + m_3 &= 0 \end{aligned} \tag{4.10}$$

$$\begin{aligned} X_1 &= \alpha_{LL} F_1 - \alpha_{L0} f_2 - \alpha_{L0'} m_2 \\ X_{1'} &= -\alpha_{L'L} F_1 + \alpha_{L'0'} m_2 - \alpha_{L'0} f_2 \\ X_2 &= -\alpha_{00} f_2 + \alpha_{00'} m_2 + \alpha_{0L} F_1 \\ X_{2'} &= -\alpha_{0'0} f_2 - \alpha_{0'L} F_1 + \alpha_{0'0'} m_2 \\ X_3 &= B_1 f_3 + B_2 m_3 \\ X_{3'} &= B_2 f_3 + B_3 m_3 \end{aligned} \tag{4.11}$$

While the reverse RCSA method used four tool measurements to solve for internal forces and moments, the forward RCSA code relates $f_2$ and $m_2$ to external force $F_1$ through experimentally-computed receptances $(B_1, B_2, B_3)$ and tip receptances:

$$f_2 = \frac{(-\alpha_{00} + B_1)(\alpha_{0'0'} + B_3) - (\alpha_{00}' + B_2)(-\alpha_{0L} F_1)}{(-\alpha_{00} + B_1)(\alpha_{0'0'} + B_3) - (\alpha_{00'} + B_2)(-\alpha_{0'0} B_2)}$$
$$m_2 = \frac{(-\alpha_{00} + B_1)(\alpha_{0'L} F_1) - (-\alpha_{0'0} + B_2)(\alpha_{0'0'} + B_3)}{(-\alpha_{00} + B_1)(\alpha_{0'0'} + B_3) - (\alpha_{00}' + B_2)(\alpha_{0'0'} + B_3)} \tag{4.12}$$

Closed-form expressions for internal forces and moments at the subsystem connection can now be substituted into the compound receptance equation:

$$\frac{X_1}{F_1} = \alpha_{LL} - \alpha_{L0} \frac{f_2}{F_1} - \alpha_{L0'} \frac{m_2}{F_1}$$

$$\frac{X_1}{F_1} = \alpha_{LL} - \frac{\alpha_{L0}\left[(-\alpha_{00} + B_1)(\alpha_{0'0'} + B_3) - (\alpha_{00}' + B_2)(-\alpha_{0L} F_1)\right]}{F_1\left[(-\alpha_{00} + B_1)(\alpha_{0'0'} + B_3) - (\alpha_{00'} + B_2)(-\alpha_{0'0} B_2)\right]} \tag{4.13}$$
$$- \frac{\alpha_{L0}\left[(-\alpha_{00} + B_1)(\alpha_{0'L} F_1) - (-\alpha_{0'0} + B_2)(\alpha_{0'0'} + B_3)\right]}{F_1\left[(-\alpha_{00} + B_1)(\alpha_{0'0'} + B_3) - (\alpha_{00}' + B_2)(\alpha_{0'0'} + B_3)\right]}$$

This expression provides the compound frequency response of any tool/milling machine combination. It can be used to predict the FRF for a collection of tools by combining the identified CNC subsystem receptance with analytic frequency response approximations for tools.

# 5. Tool-point FRF Prediction using RCSA: Experimental Results

Initial tool-point FRF measurements were made on a HAAS VF-1 three axis CNC milling machine using impact testing. Impact testing is an established method of experimental modal testing that uses high magnitude, short duration impact forces to excite the vibratory system over a broad frequency range. Impacts are delivered using a modally tuned impact hammer equipped with a piezoelectric force transducer. The impact is modeled after the impulse function, which has a force of infinite amplitude applied over an infinitesimal time. While an impulse function excites all system frequencies with constant amplitude, the frequency range and amplitude of impact hammer excitation depends on the impact duration (pulse width). Impact tests provide experimental FRFs with reasonable accuracy. Accordingly, impact testing was used to generate baseline system receptances for RCSA. RCSA predictions from these impact tests are later compared with those of the non contacting EMA.

## *5.1 Experimental Setup*

The experimental setup for modal testing consisted of a PCB Piezotronics© U086C03 modally tuned impact hammer, a Micro-Epsilon© U05 high resolution eddy current displacement sensor (ECDS), and a dSpace© (digital Signal Processing And Control Engineering) 1102 ACE kit for real-time data acquisition and control. A custom aluminum sensor mount was designed and fabricated to support the ECDS. Ten recessed set screws contact the aluminum sensor carrier and allow precise placement of the sensor probe in the mount's vertical slot (Figure 5-1). This sensor was used to record tool displacement for modal testing and non-contacting

**Figure 5-1: Eddy Current Displacement Sensor Mount**

electromechanical actuation. Figure 5-2 shows how these hardware components were utilized to facilitate modal testing. The CNC machine and complete experimental setup are shown in Figure 5-3.

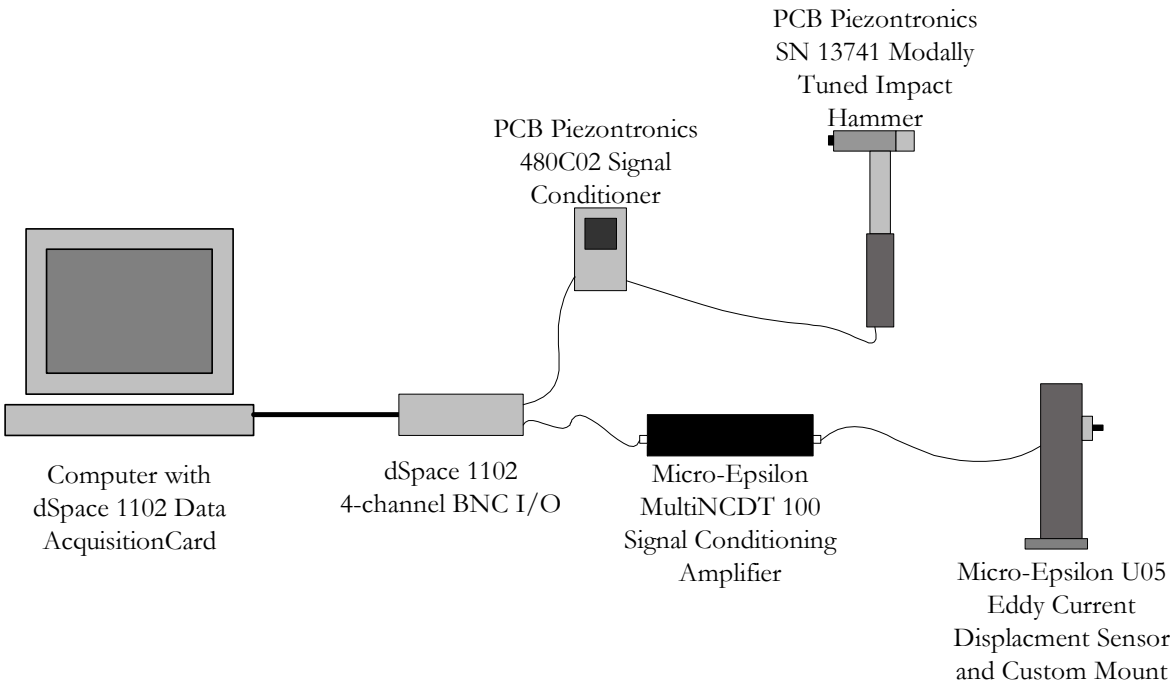


**Figure 5-2: Modal Testing Layout**

Tool blanks, made from 0.50 in diameter 1018 steel rods of various lengths, were used for these experiments. All tool blank specimens were clamped into a collet toolholder with approximately 1.50 in of insertion. The eddy current sensor and tool blank were positioned as shown in Figure 5-4 for modal testing on the CNC machine:

**Figure 5-3: HAAS VF-1 3-Axis CNC Machine and Experimental Setup**

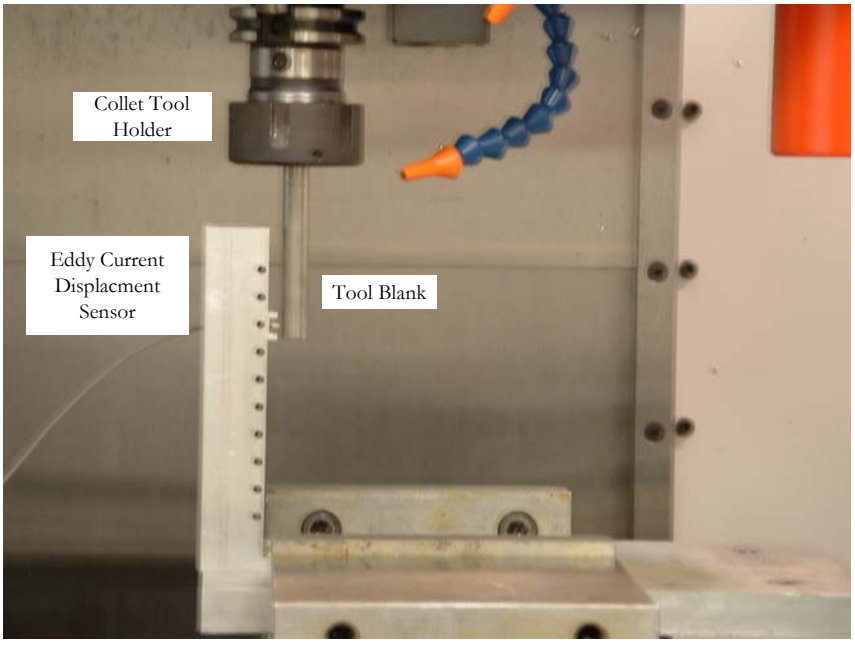


**Figure 5-4: 4.00 in Tool Blank Mounted in Collet Toolholder**

The data acquisition and control algorithm was programmed in Simulink© (MathWorks, Inc., Natick MA) and interfaced to the dSpace 1102 hardware using Real Time Workshop©, while the graphical user interface was developed using dSpace ControlDesk© 1.13 developer environment software. Force and displacement measurements were acquired at 20.0 kHz using the Simulink program of Figure 5-5. A "rising edge" force threshold trigger and negative sample delay was configured in ControlDesk to capture force and displacement data before and after impact (Figure 5-6).

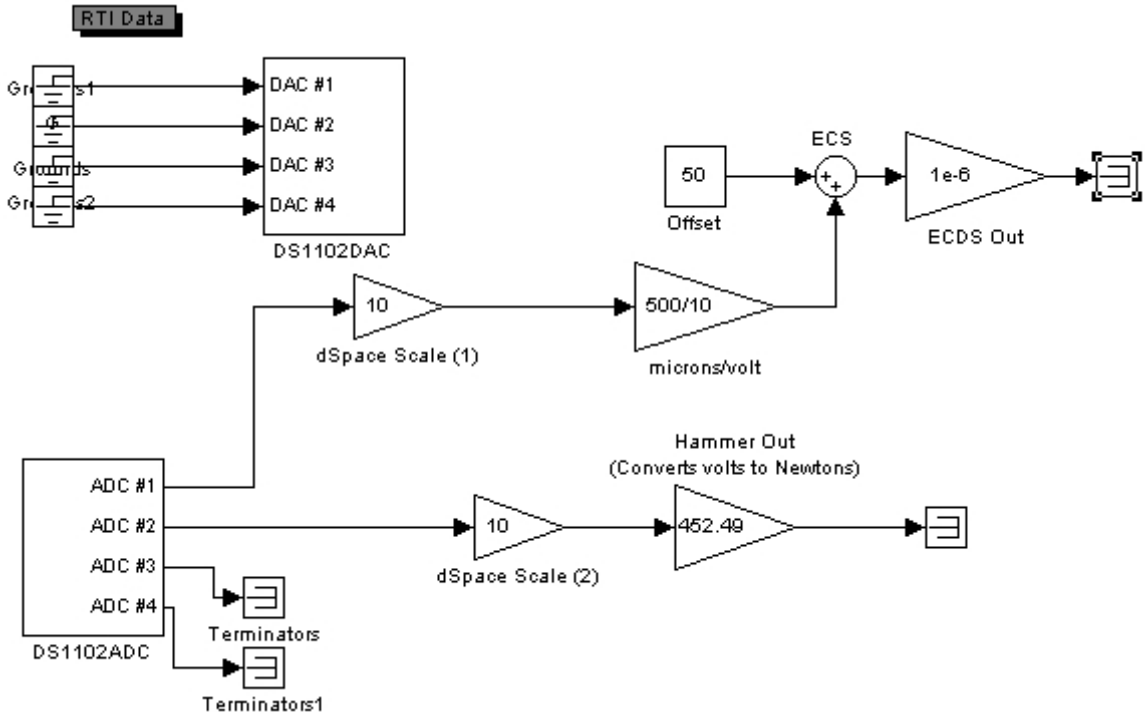


**Figure 5-5: Simulink Modal Testing Program**

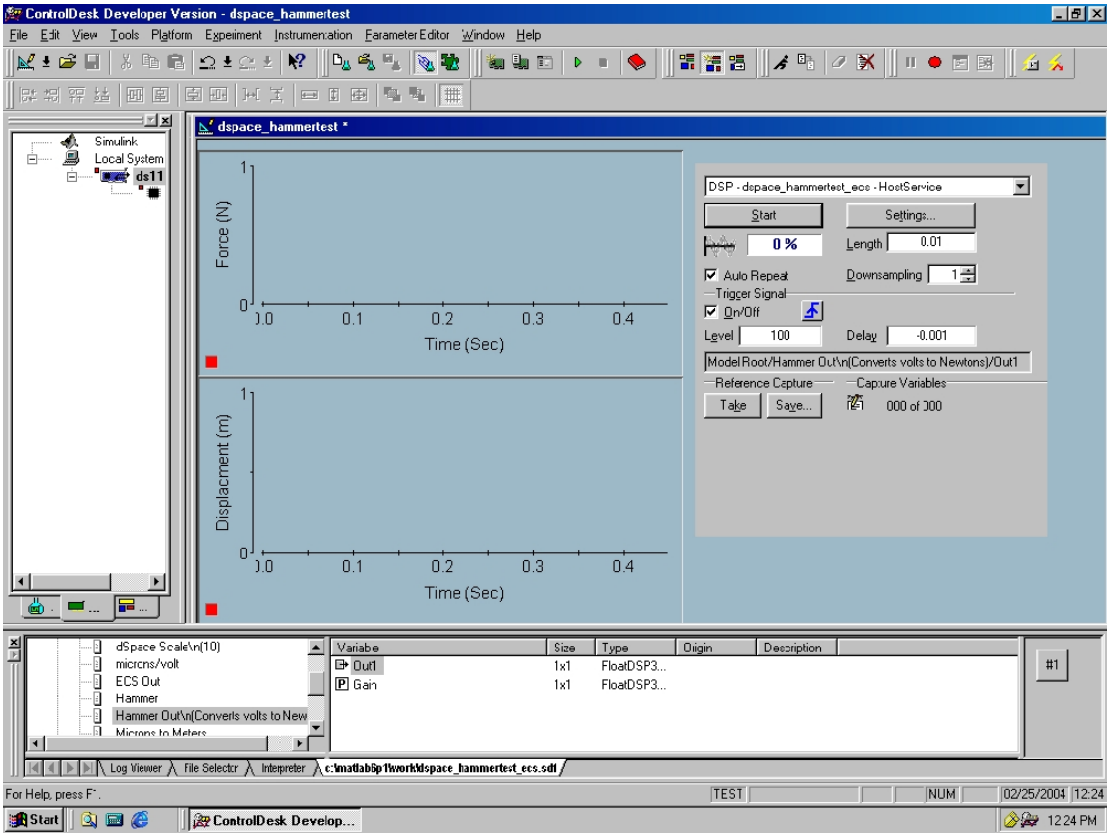


**Figure 5-6: ControlDesk Modal Testing Console**

## *5.2 Hammer Test Results*

Frequency response measurements ($X_1/F_1$, $X_2/F_1$, $X_1/F_2$, $X_2/F_2$) were collected from three 0.50 in diameter tool blanks (with overhang lengths 4.75 in, 5.75 in, and 6.75 in) mounted in the HAAS VF-1 collet toolholder. Tool blanks with overhang-to-width ratios greater than 9 to 1 were used due to an actuator resonance that limited the natural frequency of tool blanks to 650 Hz. Ten consecutive impacts and responses were recorded, transformed to the frequency domain, and averaged for smoothness and consistency. Measurement locations are shown in Table 5-1.

**Table 5-1 Modal Testing Measurement Positions**

| Tool Length in (cm) | 6.5 (16.5) | 6.8 (17.25) | 8.0 (20.25) |
|---|---|---|---|
| Tool Overhang in (cm) | 4.75 (12.1) | 5.75 (14.6) | 6.75 (17.2) |
| $X_1/F_1$ Position* in (cm) | 0.25 (.635) | 0.25 (.635) | 0.25 (.635) |
| X2/F2 Position* in (cm) | 3.25 (8.25) | 4.25 (10.8) | 5.25 (13.35) |

*Measured from Tool Tip

Figures 5-7 through 5-10 show the four measured receptances ( $X_1/F_1$, $X_1/F_2$, $X_2/F_1$, $X_2/F_2$ ) for a 5.75 in tool blank. The quality of these plots was refined by carefully impacting the tool (to minimize tip bouncing), averaging* the FRFs (to reduce scatter in the data), and employing a windowing procedure* (to eliminate noise in the time domain force data). As noted previously, RCSA theory requires that reciprocal receptances $X_2/F_1$ and $X_1/F_2$ be identical, as they appear to be.

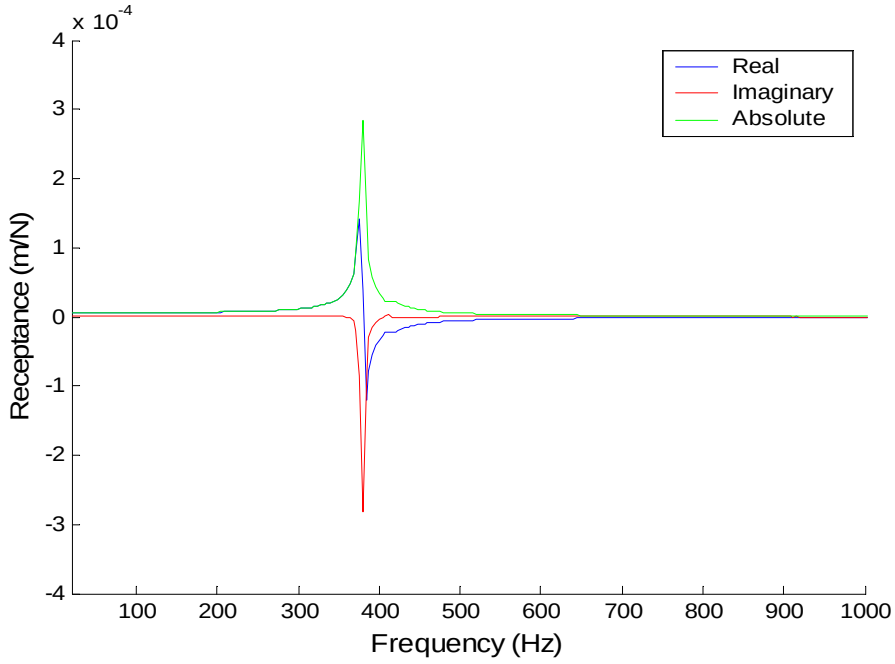


**Figure 5-7: Impact Hammer Testing $X_1/F_1$ Receptance**

* Matlab averaging and windowing routines shown in Appendix B

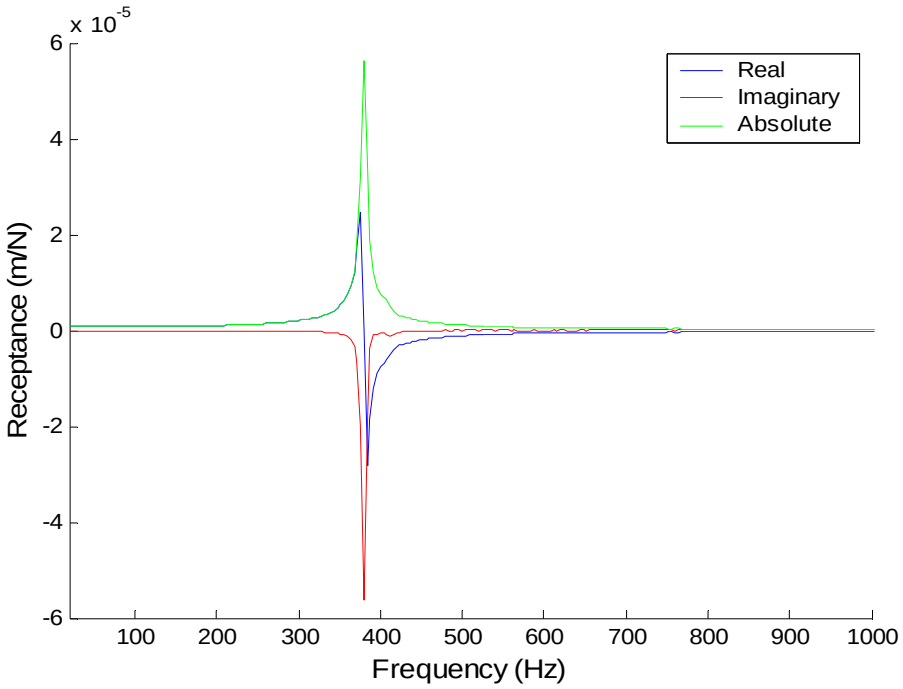


**Figure 5-8: Impact Hammer Testing $X_2/F_1$ Receptance 5.75 in Tool**

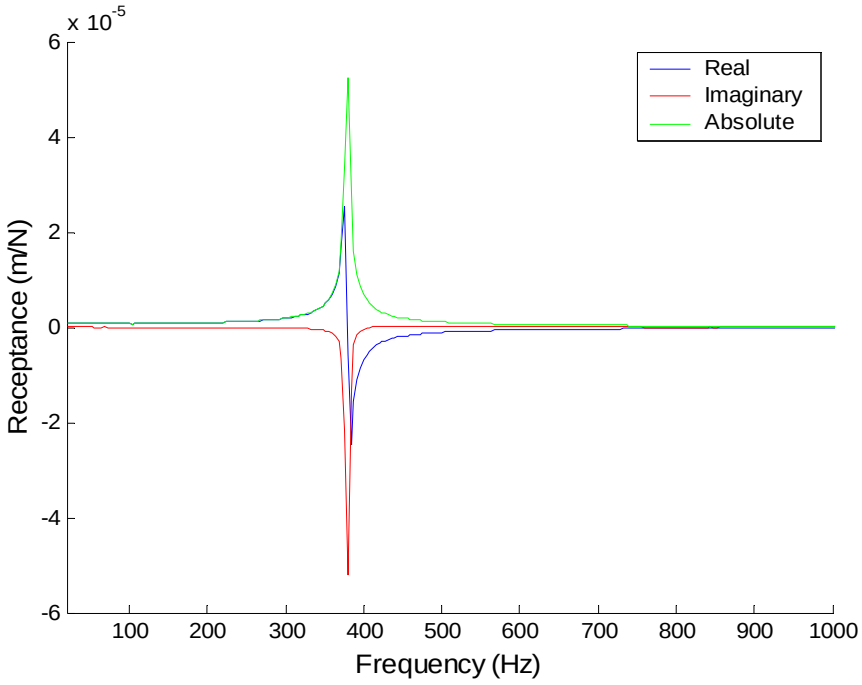


**Figure 5-9: Impact Hammer Testing $X_1/F_2$ Receptance 5.75 in Tool**

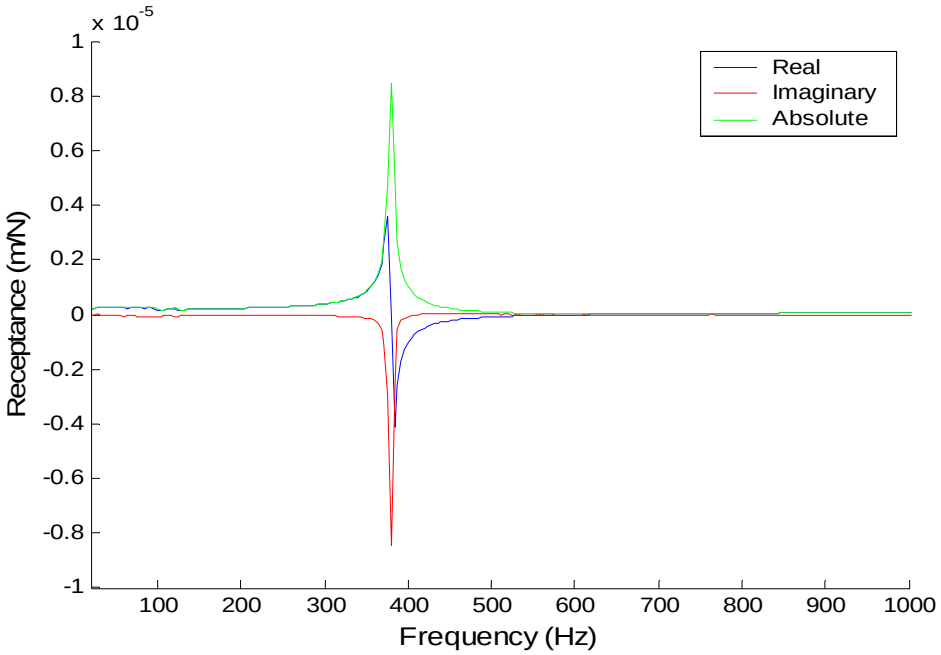


**Figure 5-10: Impact Hammer Testing $X_2/F_2$ Receptance 5.75 in Tool**

The similar shapes and magnitudes of these experimental receptances point to the accuracy of these measurements. The primary resonant mode of each receptance is clearly visible at 390 Hz (Figure 5-7 through Figure 5-10).

## *5.3 Inverse RCSA: Finding Subsystem Receptances*

The objective of inverse RCSA is to extract the "machine" receptance (including the toolholder, spindle, and milling machine structural dynamics) from the four tool-point receptances. In addition to the compound receptance measurements (the tool-point FRFs of Figure 5-7 through Figure 5-10), accurate tool blank parameters (mass, stiffness, and damping characteristics) are required for this process. As described in Section 3, the inverse RCSA algorithm solves for three independent FRFs (subsystem receptances $B_1$, $B_2$, and $B_3$) that describe the milling machine dynamics. These

subsystem responses, identified from using experimental FRFs from a 4.75 in tool and Equations 4.6 and 4.9, are presented in Figure 5-11 through Figure 5-13.

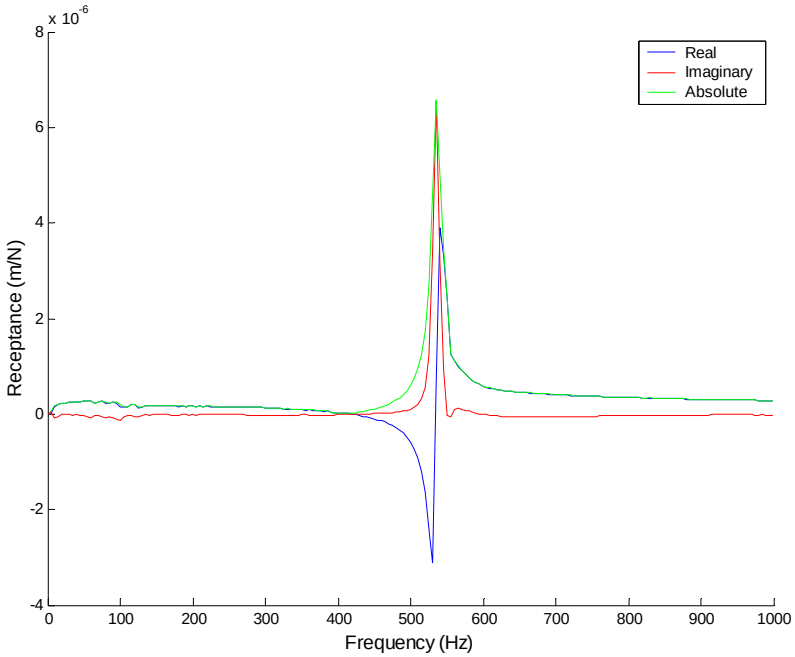


**Figure 5-11: Identified $B_1$ Receptance for a 4.75 in Tool (Impact Hammer Testing)**

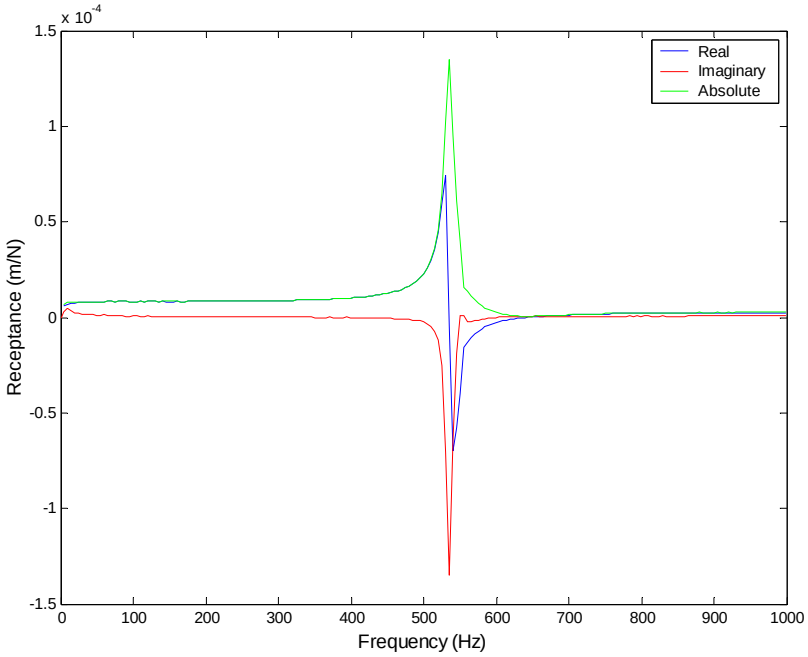


**Figure 5-12: Identified $B_2$ Receptance for a 4.75 in Tool (Impact Hammer Testing)**

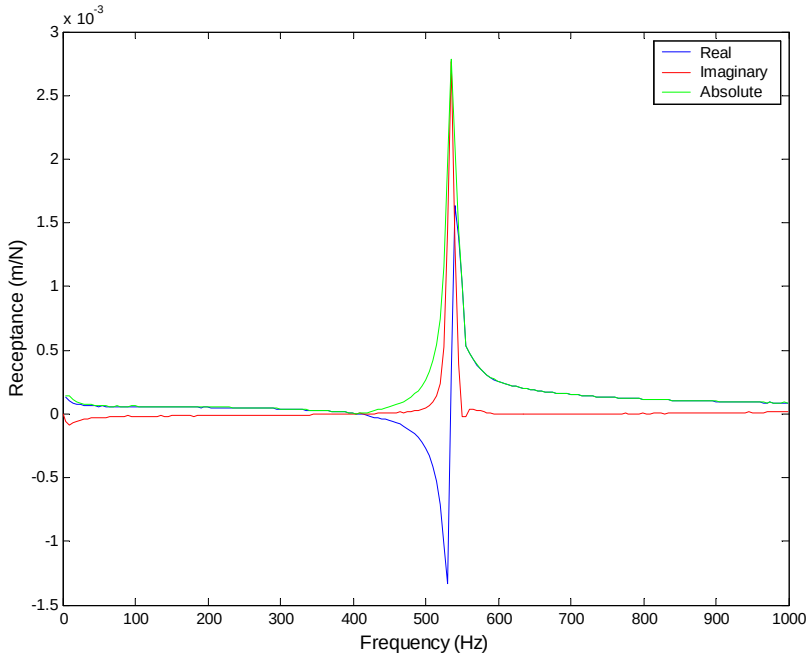


**Figure 5-13: Identified $B_3$ Receptance for a 4.75 in Tool (Impact Hammer Testing)**

As discussed in Section 4.1, the inverse RCSA process algebraically subtracts an analytic model of the lower portion of the tool blank from the compound tool-point FRF. Figure 5-11 shows this "remaining receptance" for the 4.75 in tool, which includes information about the milling machine. The inverted peak (real portion negative, imaginary positive) visible at 550 Hz in Figure 5-11 through Figure 5-13 represents the error between the analytic free-free tool FRF and the measured FRF. Small variations between modeled and actual tool responses occur at all frequencies; these differences are most discernable when the responses undergo rapid changes at the resonant point. The magnitude of this remnant peak (approximately $5\times10^{-5}\ m/N$ in Figure 5-11) can be referenced to the initial measured resonance to assess uncertainty in the RCSA process. This magnitude is approximately two orders of magnitude smaller than the primary measured tool-point receptance ($4\times10^{-4}\ m/N$ in Figure 5-7). Accordingly, the error magnitude for the algebraically-

solved B1 receptance is on the order of 1%* of the initial tool-point measurement. Because small variations in the B receptances, however, noticeably affect the size and location of the compound system resonance, the accuracy of derived B receptances is critical.

## *5.4 Forward RCSA: Predicting New Tool-point FRFs*

The identified subsystem receptances $(B_1, B_2, B_3)$ can be combined with analytic free-free tool blank receptances ($\alpha_{LL}$ Equation 4.2) using boundary and compatibility conditions (Equation 4.13). The result of this forward RCSA process is predicted tool-point FRFs for a variety of tools that can be used to predict and avoid chatter during machining. The accuracy of these predictions depends on the accuracy of the solved subsystem receptances and the analytic receptances for each tool blank. Figure 5-14 compares the actual (measured) and predicted tool-point FRF for a 5.75 in tool blank (calculated using B receptances derived from a 4.75 in tool blank).

* B2 and B3 receptances are defined as slope over input force and slope over moment. As a result, these receptances cannot be directly compared to the measured receptances. Accuracy is assumed similar to that of the B1 receptance.

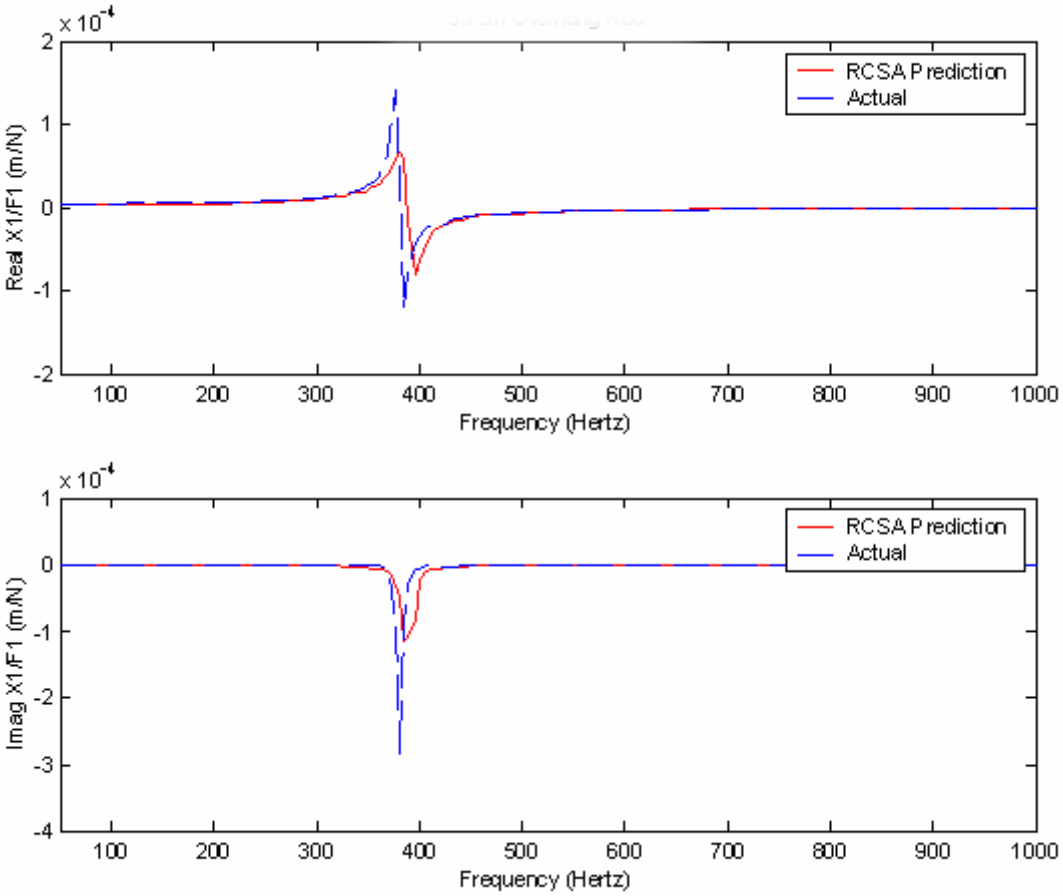


**Figure 5-14: Impact Hammer RCSA Prediction and Measured Tool-Point FRF**

The poor agreement between predicted and measured responses proved to be a very difficult problem to solve. Although impact measurements were taken with great care and measured data was averaged and windowed to improve accuracy, magnitude errors between predicted and actual tool-point FRFs appear to be caused by measurement inaccuracies. As discussed in Section 5.3, the inverse RCSA process is extremely sensitive to measurement errors and uncertainties; small variations in $B_1$, $B_2$, and $B_3$ yield large changes in predicted FRFs. It appears that impact hammer tests do not generate force across a sufficient frequency range to accurately characterize the milling machine receptances. Specific problems with modal testing are discussed in detail in the following

section. Later sections outline the use of a non-contacting electromechanical actuator (EMA) to make more accurate FRF predictions.

## *5.5 Modal Testing Drawbacks*

Impact hammer testing is a relatively straightforward experimental method used to determine the modal characteristics of vibratory systems. However, the accuracy of impact test results is often compromised by limited input force and suboptimal impulse profiles. Exciting stiff, lightly-damped structures (such as the tool blanks used in this research) can be a formidable task. Such systems require a hard-tipped impact hammer (which provides a short duration, high force impact) to excite frequencies across a broad frequency range. Unfortunately, it is very difficult to avoid multiple impacts when using a hard tipped hammer on such structures. For this reason, a firm nylon tip was selected for the PCB U086C03 impact hammer to achieve the broadest possible frequency range of excitation while minimizing multiple impacts. Figure 5-15 and Figure 5-16 show force inputs to a 3.25 in tool blank with impacts delivered at Location 1 (the tool tip) and 2 (the tool/toolholder interface), respectively. Figure 5-17 and Figure 5-18 show the frequency content of Figure 5-15 and Figure 5-16, respectively, obtained by averaging 10 consecutive impacts.

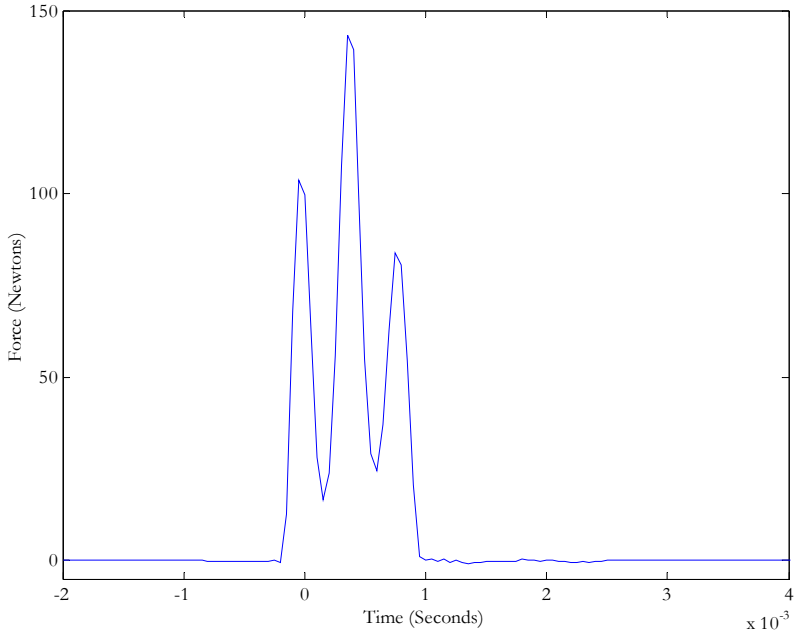


**Figure 5-15: Impact at Tool Tip (Location 1)**

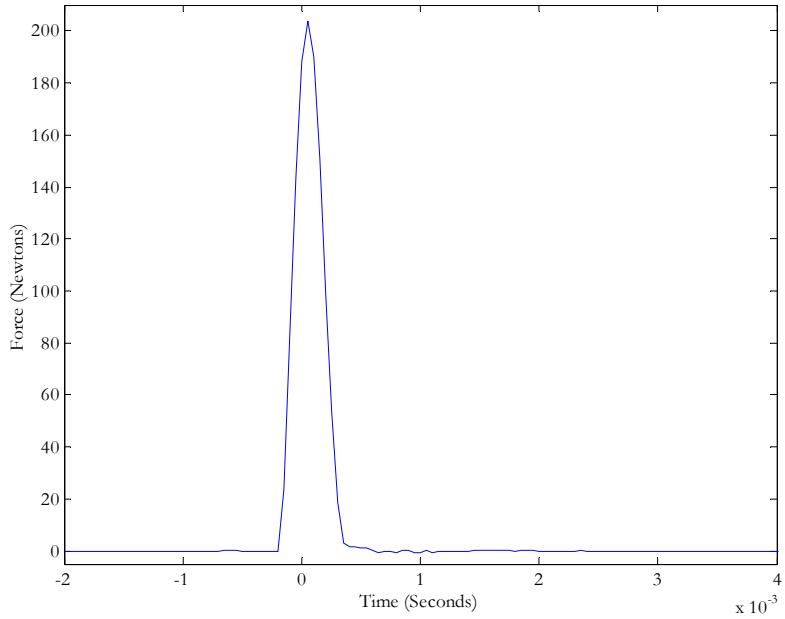


**Figure 5-16: Impact at Tool Interface (Location 2)**

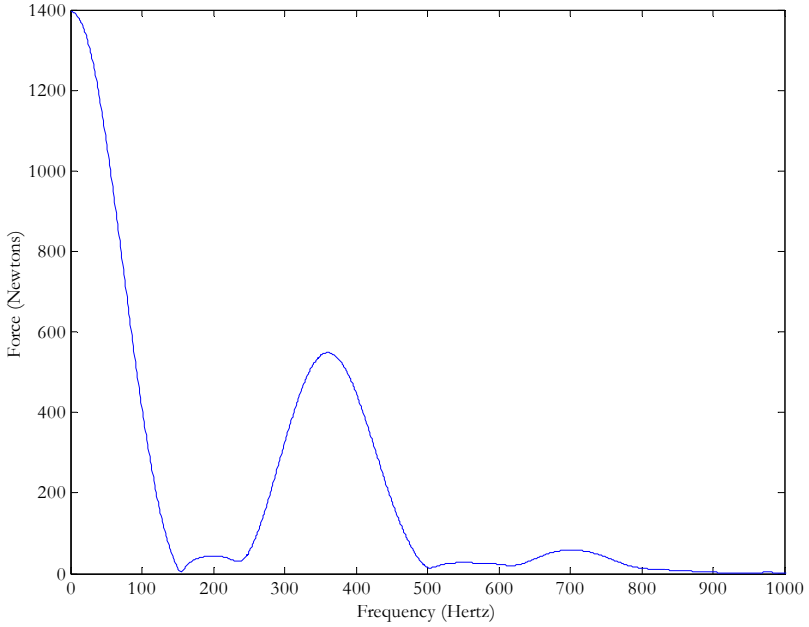


**Figure 5-17: Frequency Spectrum at Tool Tip (Location 1)**

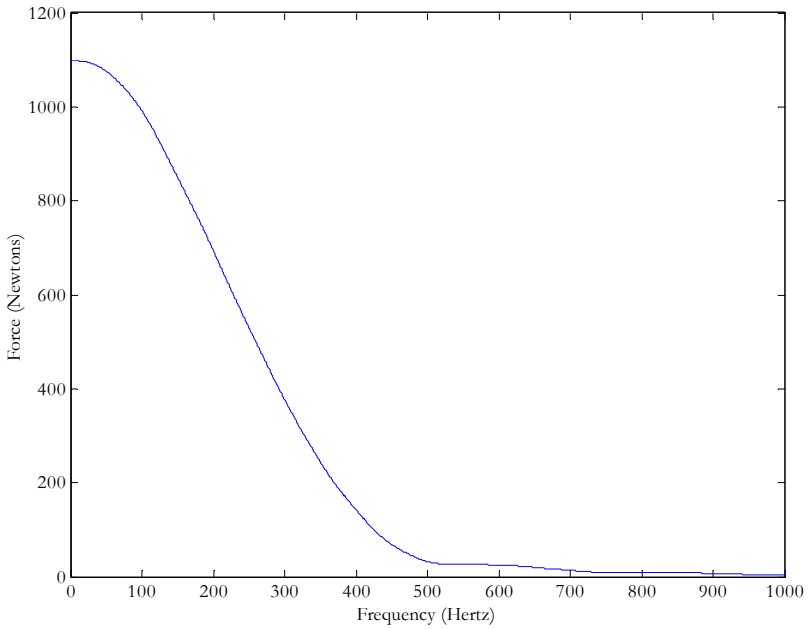


**Figure 5-18: Frequency Spectrum at Tool Interface (Location 2)**

The multiple impact problem (Figure 5-15) was observed on all tool tip force input receptances ($X_1/F_1$, $X_2/F_1$) measured on tool blanks longer than 3.0 in. This occurs because the amplitude of vibration for these longer tool blanks is enough to re-contact the hammer tip. Shorter tool blanks or tool-interface receptances ($X_1/F_2$, $X_2/F_2$) do not exhibit this problem. While both impact magnitudes (Figure 5-17 and Figure 5-18) decay rather quickly with frequency, the tool tip impact (Figure 5-17) declines to almost zero at 150 Hz and then 'bounces' at higher levels. This is a direct result of the multiple hits shown in Figure 5-15. Though the impact spectrum of Figure 5-18 indicates a much cleaner force profile, it fails to excite modes above 400 Hz. A steel tip would provide a flatter excitation profile for tool interface excitation but it would exacerbate the problem of multiple impacts.

Problems associated with impact hammer excitation undeniably result in measurement inaccuracies for tip-forced FRFs. Multiple impacts or 'bouncing' clearly alter the spectral characteristics of the excitation. Figure 5-19 shows the tool-point receptance for a 3.25 in tool blank, measured using impact hammer excitation. The second crest in this response (at approximately 1050 Hz) results from the second peak visible in the force spectrum (Figure 5-17).

Additional concerns with impact hammer excitation involve the lack of sufficient input force to accurately characterize subsystem dynamics. The non-contacting electromechanical actuator described in the following section overcomes these modal testing limitations. The actuator develops controllable magnetic excitation forces of sufficient amplitude and bandwidth to overcome these limitations.

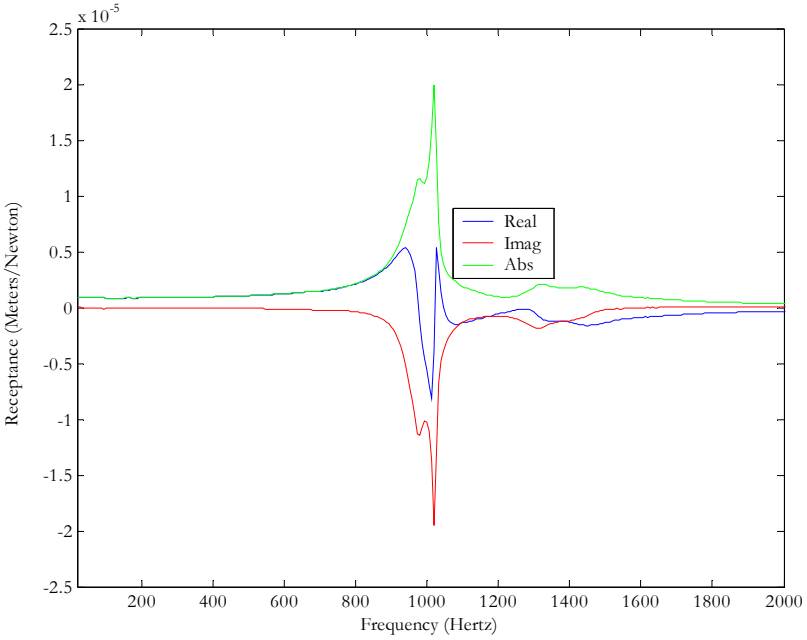


**Figure 5-19: $X_1/F_1$ Impact Hammer Receptance 3.25 in Tool Blank**

# 6. Experimental RCSA – Non Contacting EMA

The non-contacting electromechanical actuator (EMA) presented in this section is a third-generation prototype (Figure 6-1) designed to measure four tool-point receptances on a HAAS VF-1 3-axis milling center. The geometry of the actuator core was designed using magnetic circuit analysis (MCA), generalized machine theory (GMT), and finite element analysis (FEA). Designs for the actuator support structure and displacement sensor mount were dictated by the RCSA process (which requires measurements of excitation force and tool response at Locations 1 and 2 of the tool). The problems associated with impact hammer excitation (outlined in Section 5.5) are greatly reduced using a non-contacting, high-amplitude (1-50 N), broadband (1-1000 Hz) swept sinusoid input.

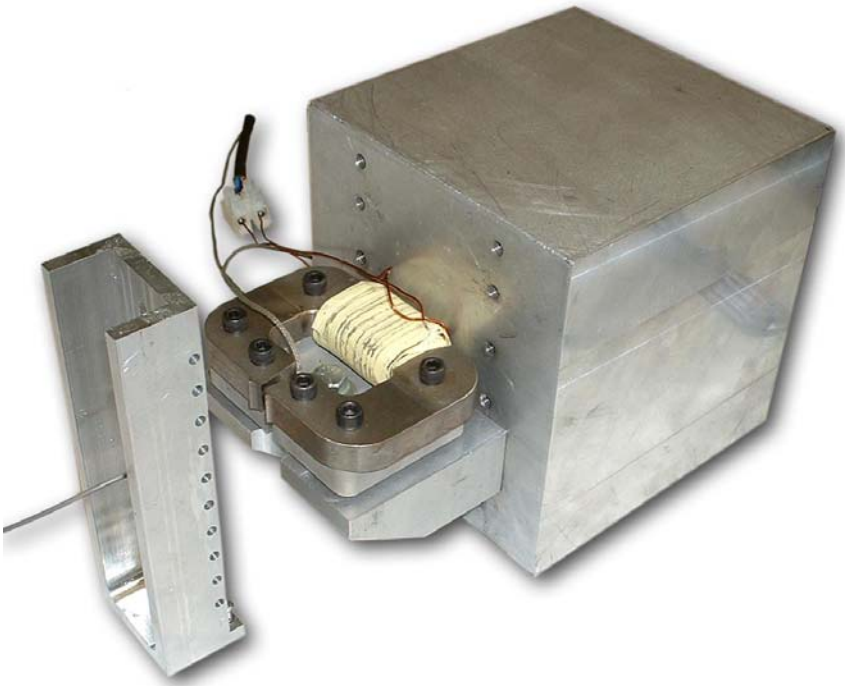

**Figure 6-1: Electromechanical Actuator, with Support Structure and Displacement Sensor Mount (Connecting Base Plate Omitted)**

## *6.1 EMA System Design*

This third-generation prototype utilizes a solid ferromagnetic core similar in dimensions and performance characteristics to the first-generation EMA prototype [9]. The design specifications for this EMA are compiled in Table 6-1. Details of the actuator design, modeling, analysis, and experimental evaluation can be found in Caulfield, et al [9], and are not reproduced here.

**Table 6-1 Actuator Force Parameters**

| | |
|---|---|
| Max Supply Current | 10.0 A |
| Core Depth cm (in) | 1.25 (0.5) |
| Tool Diameter cm (in) | 1.25 (0.5) |
| Nominal Air Gap cm (in) | .038 (0.015) |
| Force (10 Amps) | 50 N |
| Bandwidth | 0-1000Hz |

The EMA was designed to impart controllable force profiles (in this case swept sinusoids) to tool blanks mounted in the toolholder of the Haas VF-1 machining center. Current in the core windings creates magnetic flux through the actuator core and across the air gap. When a ferromagnetic tool is positioned in the gap, a magnetic reluctance force (attractive only) is developed in proportion to the core flux. This reluctance force provides controllable, non-contacting excitation. Swept sinusoids are used in this research because they impart high-amplitude (0 to 50 N) excitation across the entire frequency range of interest. While the excitation mechanism is unchanged from the first-generation prototype, this actuator and sensor system has been designed to meet requirements specific to the RCSA process.

### 6.1.1 RCSA Requirements

The RCSA approach described in this document requires precise application and measurement of excitation force and tool displacements at two locations on the tool blank: the tip (Location 1) and the tool/toolholder interface (Location 2). Because the EMA system is required to accommodate a range of tool lengths (overhangs from 1 in to 7 in), the actuator and displacement sensor must have multiple, precisely-located mounting positions. Accuracy of the excitation waveform is critical to the process: inadequate bandwidth, amplitude, and multiple impacts were blamed for poor RCSA predictions from modal testing. Measurement specifications require that the actuator mount and displacement sensor mount have natural frequencies significantly higher than the tool blank specimens.

### 6.1.2 Hardware Design

All structural components were designed using SolidWorks 2003 solid modeling software. 6061-T6 aluminum was selected for sensor and actuator support structures due to its non-ferromagnetic properties, excellent mechanical characteristics, and ease of machinability. The sensor and actuator mounts were designed to be secure yet able to be quickly repositioned. The complete EMA test setup was fabricated to fit into a standard 8 in milling center vice. The original EMA core and shelf design was revised to include a force measurement sensor (Figure 6-2) while the ECDS vertical sensor slot was lengthened (Figure 6-3) to accommodate tool blanks of 7 in overhang. The complete EMA experimental setup is shown in Figure 6-4. Dimensioned part drawings for all actuator hardware are included in Appendix A.

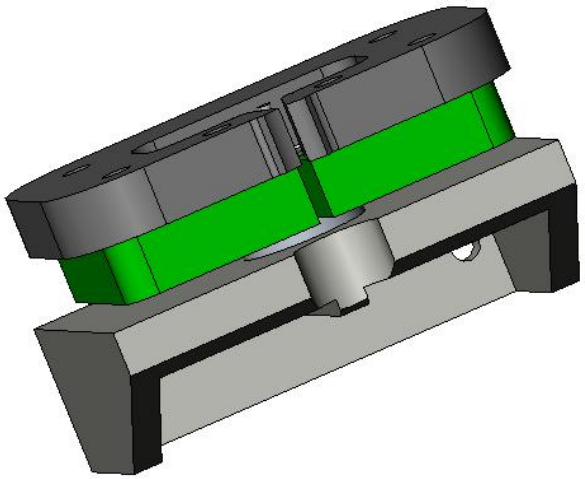

**Figure 6-2: EMA Core, Custom Sensor Plate, and PCB Shear Force Sensor**

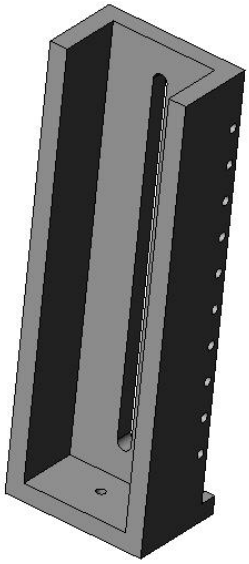

**Figure 6-3: Updated ECDS Mount**

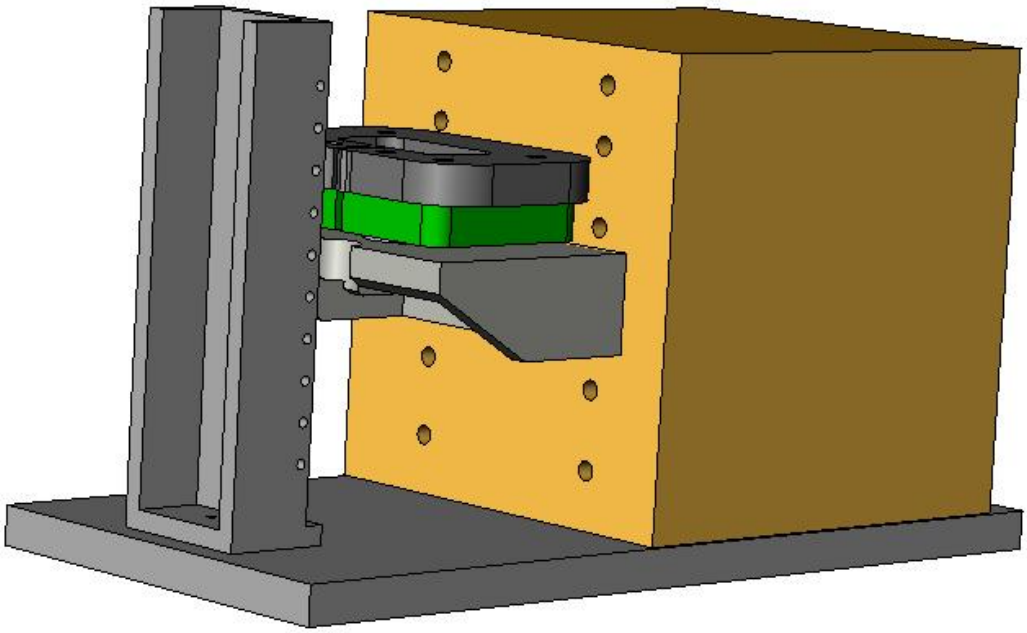

**Figure 6-4: Complete EMA Experimental Setup**

Natural frequencies and mode shapes for the sensor and actuator mounts were computed using CosmosWorks finite element analysis add-on package. Results are presented in Figure 6-5, Figure 6-6, and Table 6.2.

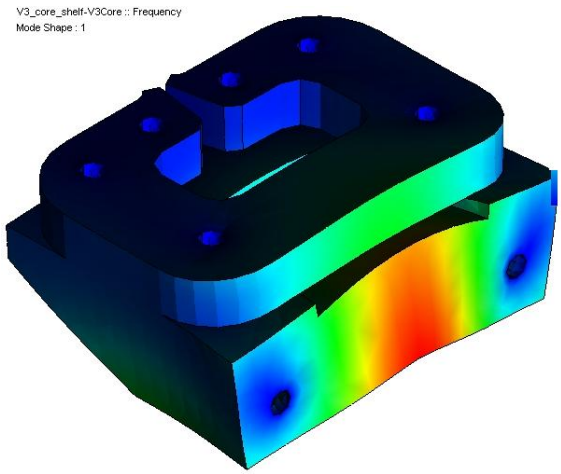


**Figure 6-5: FEA Modal Analysis of EMA Core and Actuator Shelf**

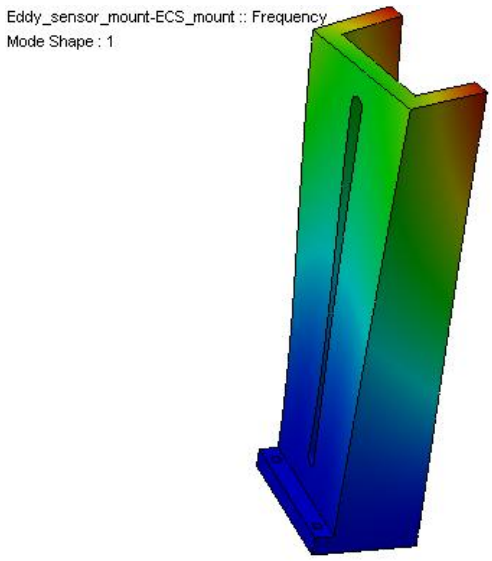


**Figure 6-6: FEA Modal Analysis of Eddy Current Sensor Mount**

**Table 6-2 FEA Modal Analysis Natural Frequency Predictions**

| First Mode Natural Frequency (Hz) | |
|---|---|
| Eddy Current Sensor Mount | 923 |
| EMA Actuator Mount | 1190 |

The FEA results of Table 6-2 predict fundamental natural frequencies of 923 Hz and 1190 Hz for the sensor tower and EMA structure, respectively. The predicted actuator structure natural frequency is above the 0-1000Hz measurement range. The ECDS first mode natural frequency, however, is within the range. Because excitation forces are not applied directly to the ECDS sensor mount (though forces may be transmitted through the EMA system baseplate), this bandwidth

limitation was not considered significant. No motion was measured on the ECDS mount during initial EMA swept sinusoid tests.

Later modifications to the EMA structure to include an actuator force sensor (Figure 6-2) dramatically reduced the EMA structure natural frequency. Designing and fabricating an EMA system including onboard force measurement with sufficient stiffness proved to be very difficult. Force measurement is discussed in detail in the following section. A compromise between system stiffness and measurement capability was reached with this system. Future work should focus on designing an actuator structure with force measurement capability that has a natural frequency well above that of milling center tooling.

### 6.1.3 Actuation Force Measurement

Accurate tool-point FRFs require accurate measurements of applied force and resulting displacement. Measuring displacement with requisite accuracy was straightforward; the Micro_Epsilon DT110-S-U05-M-C3 eddy current displacement sensor and custom sensor mount (Figure 5-1) provided 0.5 μm resolution with a bandwidth of 10 kHz. Accurately measuring or predicting the excitation force, however, proved to be extremely challenging. The principal difficulty with actuation force measurement was that the EMA system stiffness had to be maintained above that of the measured tool specimens. Several different force prediction and measurement approaches were attempted – each had caveats. Ultimately, a custom piezoelectric shear force sensor from PCB Piezotronics, model 201M73, proved to be the best compromise between system stiffness and measurement resolution. The following sections describe the attempted force measurement approaches.

***Force Prediction***

Initial research efforts focused on predicting (rather than measuring) excitation force. This approach utilized real-time measurements of tool displacement and EMA coil current to predict force. A nonlinear actuator force model was developed using generalized machine theory (GMT) to relate reluctance force to coil current and air gap [9]:

$$F_a(t) = -\frac{n_c^2 i(t)^2 \mu_g A_g}{4\left(l_{gnom} + \frac{x(t)}{\sin(\theta)}\right)^2} \tag{6.1}$$

*where :*
$n$ = *Number of coil turns*
$i(t)$ = *Coil current*
$\mu_g$ = *Permeability of free space*
$A_g$ = *Cross sectional area of core*
$lgnom$ = *Mean flux path length*
$x(t)$ = *Tool position*
$\sin\theta$ = *Angle relation to find net lateral tool force*

A simplified force expression incorporates many of these design parameters into a single constant of proportionality K :

$$F = K\frac{i^2}{x^2} \tag{6.2}$$

Because coil current i(t) and tool displacement x(t) are readily available measurements in the dSpace control system, force prediction simply requires that the constant of proportionality in (Equation 6.1) be solved offline using stored force and displacement data. For example, Figure 6-7 shows computed force for a portion of the 0-1000Hz excitation sweep at 7.5 amps peak current:

Unfortunately, the actuator force (Equation 6.1) derived using GMT does not account for non-linear effects such as magnetic saturation, fringing, and leakage fluxes. Predicted actuation forces were compared to measured forces (using the piezoelectric shear sensor) across a range of nominal coil currents and air gaps, but the accuracy was found to be unacceptably poor for large coil currents and small air gaps. To ensure accurate knowledge of the actuation force, a decision was made to add a force sensor to the EMA system.

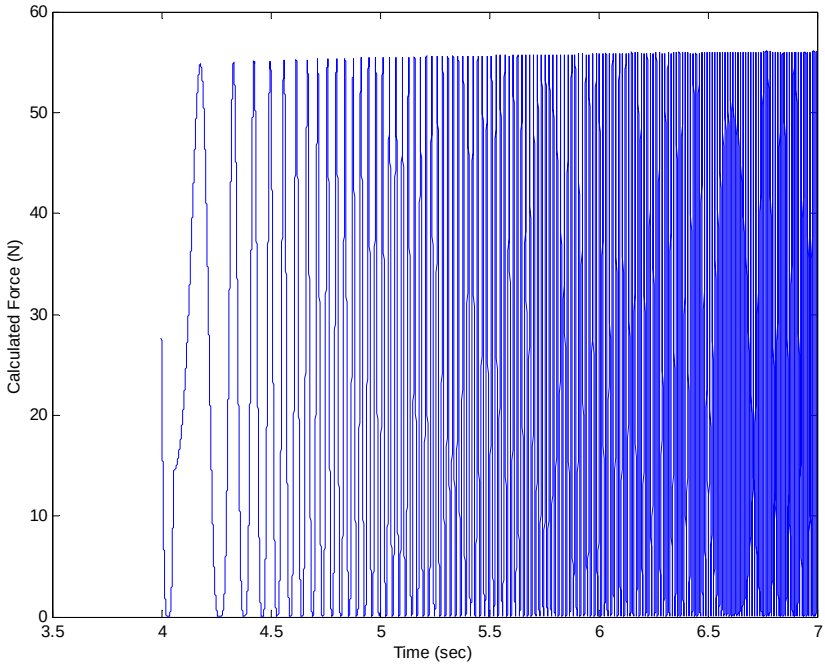


**Figure 6-7: GMT Calculated Swept Sinusoid Actuation Force**

***Strain Gage***

Strain gage measurement was the first choice because for this application because it offered a simple and reliable method to measure static and dynamic forces. A monolithic aluminum "bending beam" mount was designed to support the EMA and mount four Vishay Micro Measurement CEA-125UN-05-350 strain gages (Figure 6-8). These gages are temperature compensated specifically for aluminum substrates and designed for high voltage (12.0 V max) excitation. Two gages were glued on each side of the "bending beam" to create a load cell with full-bridge strain measurement circuitry.

**Figure 6-8: EMA Actuator Mount; Full Bridge Strain Gage Circuit**

Dimensions for the aluminum strain gage load cell were specified to provide adequate force sensitivity ($5mv/N$) while retaining the requisite EMA system stiffness of 1500 Hz (ensures that the fundamental vibration mode remained well above that of the tool blanks). For design purposes, this fundamental frequency can be approximated by lumping the system mass at the EMA (neglecting the mass contribution of the mounting bracket):

$$\omega_n = 1500\ Hz = \frac{1}{2\pi}\sqrt{\frac{k_{mount}}{m_{EMA}}} \tag{6.3}$$

Where $m_{EMA}$ is the actuator mass, 0.770 kg. The required strain block stiffness is $k_{mount} = 6.56 \times 10^7 \ N/m$. This bending stiffness is related to the load cell dimensions of Figure 6-9:

$$k_{mount} = \frac{3EI}{l^3}$$
$$k_{mount} = \frac{3(69 \times 10^9 \ Pa)I}{l^3} \tag{6.4}$$

Where $I$ is the area moment of inertia of the mount:

$$I = \frac{bh^3}{12} = \frac{(0.03m)(0.02m)^3}{12} = 2 \times 10^{-8} m^4 \tag{6.5}$$

Specifying mount dimensions of $b = 0.03\,m$, $h = 0.02\,m$, and $l = 0.04\,m$ results in $I = 2 \cdot 10^{-8} m^4$, $k_{mount} = 6.56 \cdot 10^7 \ N/m$, and $\omega_n = 1469$ Hz.

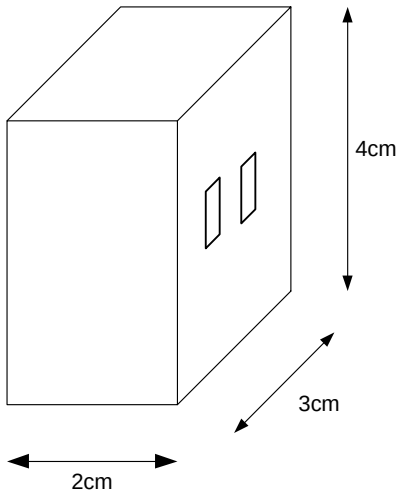


**Figure 6-9: Strain Gage Load Cell Dimensions**

The strain gage load cell was bolted top and bottom to the EMA plate and actuator shelf, respectively. These 3 cm connecting bolts were sized to extend only 1 cm into the block with 200 Nm of preload torque.

.

The minimum bending strain in the strain gage load cell ($0.1\mu strain$) is found from minimum actuator force ($0.1N$) through equation 5.6.

$$\varepsilon_{min} = \frac{\sigma_{min}}{E} = \frac{M_{min}\, h/2I}{69\times10^{9}\ Pa} = \frac{F_{min}\, lh/4I}{69\times10^{9}\ Pa} \tag{6.6}$$

$$\varepsilon_{min} = \frac{(0.1N)(.01m)(.07m)/2(2\cdot10^{-8}m^{4})}{69\cdot10^{9}\quad Pa} = 0.025\mu strain$$

$$\varepsilon_{min\ Corrected} = 4\cdot\varepsilon_{min} = .1\mu strain$$

This minimum bending strain in the load cell is multiplied by a factor of 4 (four gages installed) due to the full bridge strain circuit. Amplification for the full bridge output was achieved using a custom

electrical circuit based on the Analog Devices AD620 instrumentation amplifier (Figure 6-10). Batteries provided the +/-9.0 V power for this circuit to minimize electrical noise and ground loops, resulting in an output range of +/-7.2 V. Although this circuit provided a peak amplification of 10,000, noise and shielding problems could not be resolved. Thus, the custom amplification circuit was later replaced with a Vishay Micro Measurements 2010 signal conditioning amplifier (Figure 6-11).

The strain gage load cell was calibrated by sequentially loading the structure with known weights and recording the amplified output. The experimental calibration curve is shown in Figure 6-12, which reveals a force sensitivity of $5.6 \cdot 10^{-3}\, V/N$ at an amplifier gain of 5,000. This predicted voltage output at $1.0N$ load is quite close to the calculated strain sensitivity of Equation 5.6 and it is well within the measurement resolution of the dSpace 1102 16-bit data acquisition system.

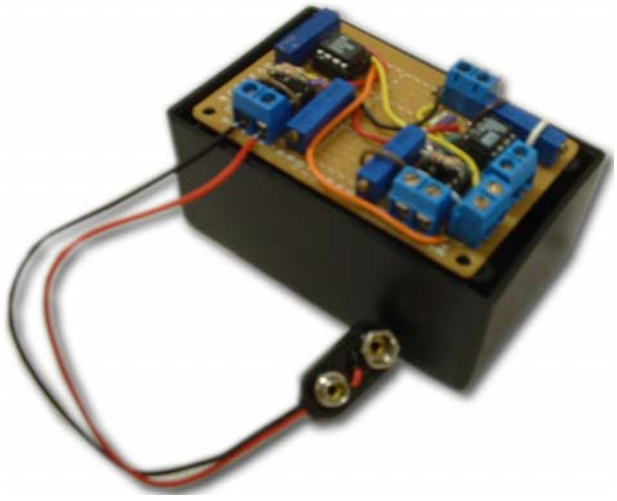

**Figure 6-10: Custom Strain Gage Load Cell Amplifier**

**Figure 6-11: Vishay Micro Measurements 2110 Signal Conditioning Amplifier**

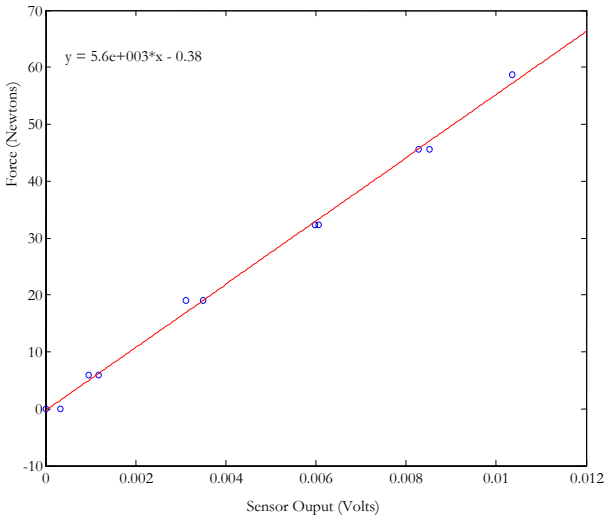


**Figure 6-12: Strain Gage Load Cell Calibration Curve**

To validate the stiffness and modal characteristics of the strain gage load cell, impact hammer tests were conducted. Figure 6-13 shows that the first natural frequency (1600 Hz) is close to the predicted natural frequency (1469 Hz), and well above the resonant frequency of a 4.5 in tool (650 Hz).

The custom load cell exhibited excellent sensitivity and accuracy during static testing. However, dynamic measurements with the EMA revealed limitations of the device. Figure 6-14 shows typical measurements to a linear swept sinusoid (1-1000 Hz).

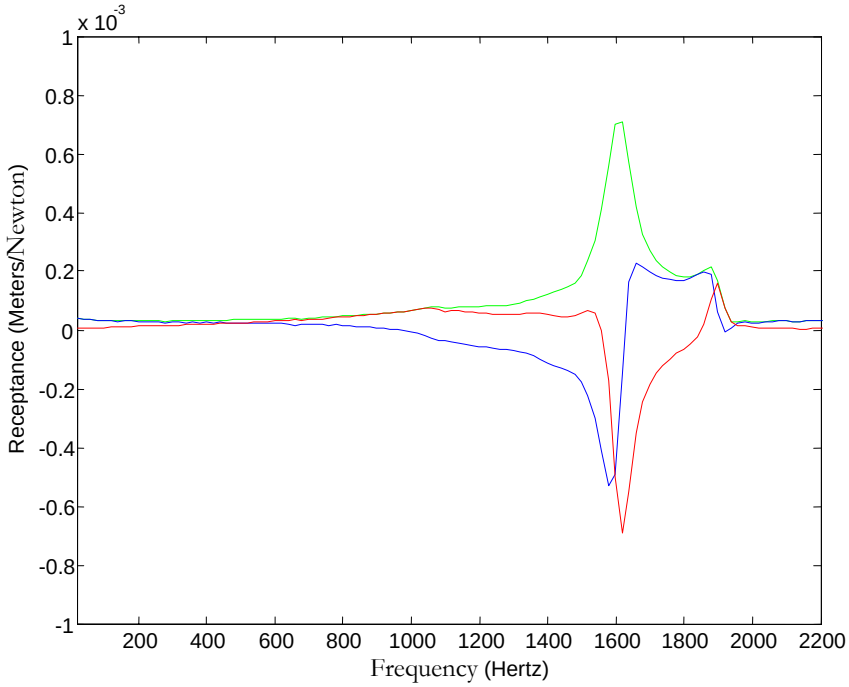


**Figure 6-13: Impact Hammer Tests on EMA Structure with Strain Gage Load Cell**

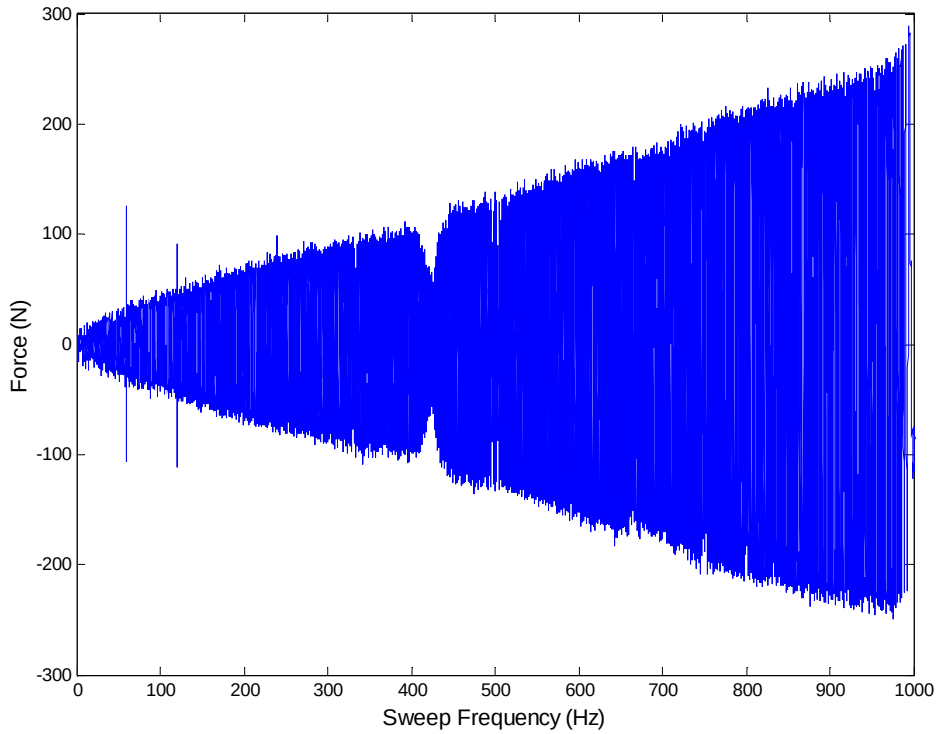


**Figure 6-14: Strain Gage Load Cell Swept Sinusoid Force Measurements**

At first glance, Figure 6-14 appears to be the force amplitude response of a system approaching resonance. However, this increase in amplitude is approximately linear with frequency, and doesn't coincide with the fundamental resonance of this system (1600 Hz, as shown in Figure 6-13). Experimental tests linked this erroneous signal growth to the rate of change of EMA core current. It was later confirmed that EMA leakage flux was inducing voltage in the strain gage wires. The linear increase in force amplitude results from the linear frequency increase of the swept sinusoid coil input (induced voltage is dependent on the rate of change of magnetic flux). Several attempts were made to shunt leakage flux away from the sensitive strain gage wires. Adding a 1/8 in ferromagnetic plate to the top of the strain gage load cell (Figure 6-15) reduced signal amplification across the 0-1000 Hz range to approximately 10%.

**Figure 6-15: Strain Gage Load Cell with Ferromagnetic Shield (Actuator Removed)**

The additional mass of this shield, however, shifted the system's fundamental frequency to approximately 800 Hz, unacceptably close to the resonant frequency of tool blanks. For these reasons, the strain gage load cell was replaced with a commercial force sensor.

### *Piezoelectric Shear Sensor*

PCB Piezotronics supplied a customized piezoelectric shear sensor, PCB model 201M73, for this application (Figure 6-16). A 5/16 in mounting stud and tensioning nut sandwiched the sensor between the bottom surface of the custom sensor mount plate (bolted to the EMA core) and the aluminum actuator shelf. Sensor specifications are listed in Table 6-3.

**Figure 6-16: PCB 201M73 Shear Force Sensor**

**Table 6-3: PCB Piezotronics Shear Force Sensor Specifications**

| Part Number | PCB 201M73 |
|---|---|
| Measurement Range N (lbf) | 444.8N (100) |
| Resolution N (lbf) | .009 N (0.002) |
| Preload | 5ft-lbs on stud or 1000lbs |

Piezoelectric sensors produce output voltages only in response time-varying strains, and are thus poor choices for static measurements. Because the EMA can only develop attractive forces, the swept sinusoid force profile is in fact generated by an offset sine wave (the actuator force has a non-zero mean, as shown in Figure 6-17. This static force component is subject to decay using piezoelectric sensors like the PCB 201M73. Initial dynamic measurements exhibited signal decay associated with this non-zero mean. This measurement inaccuracy was eliminated by inserting an initial 'offset signal' with identical mean to the swept sine input, as shown in (Figure 6-18). The duration of this initial offset signal was selected to allow the static force component to fully decay, eliminating erroneous drift in the swept sinusoid measurement.

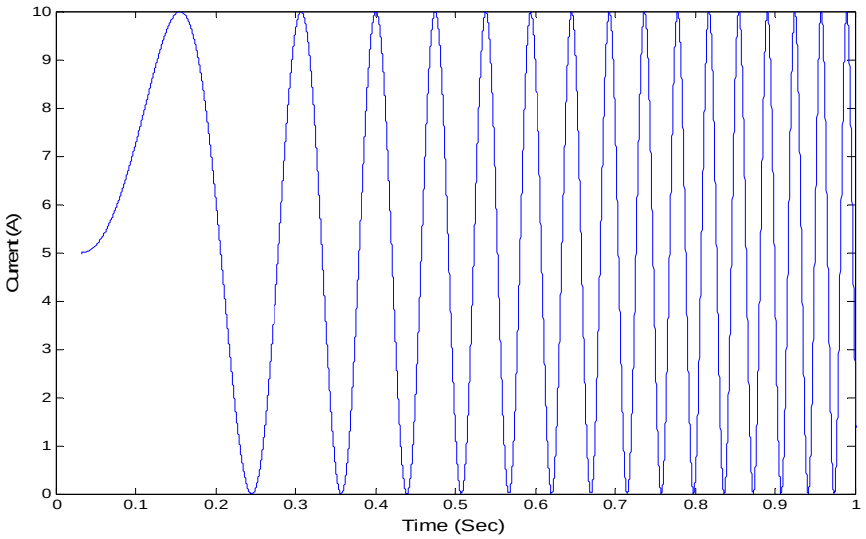


**Figure 6-17: Offset Sinusoid EMA Core Current Input**

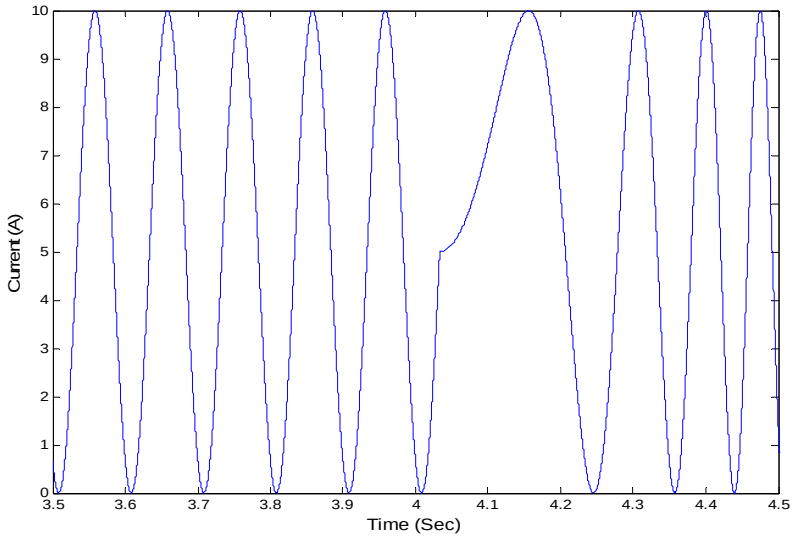


**Figure 6-18: EMA Current Input Prep Signal (0-4 Sec)**

Unfortunately, incorporating the PCB 201M73 sensor significantly lowered the fundamental frequency of the EMA system from 1600 Hz to only 575 Hz (Figure 6-19). Extensive modal testing attributed this unacceptably low natural frequency to bending in the 5/16 in mounting stud. In order to raise the natural frequency, the sensor was refitted with a 3/8 in mounting stud (the largest accommodated) and the mass of the EMA core and mounting hardware was reduced. Although these modifications increased the fundamental frequency to 690 Hz (Figure 6-20), this limited bandwidth of the EMA system restricted the range of tool blanks that could be tested.

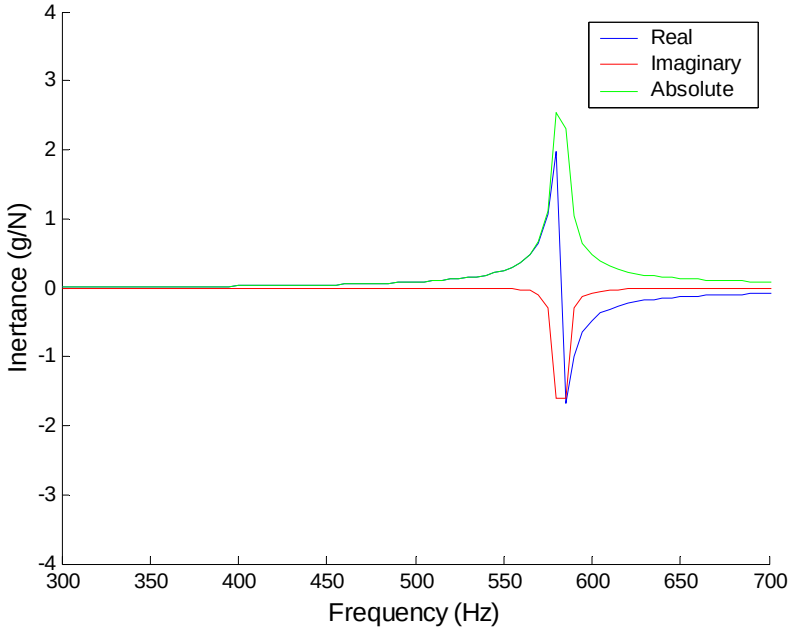


**Figure 6-19: Actuator Response with PCB Shear Force Sensor and 5/16in Stud**

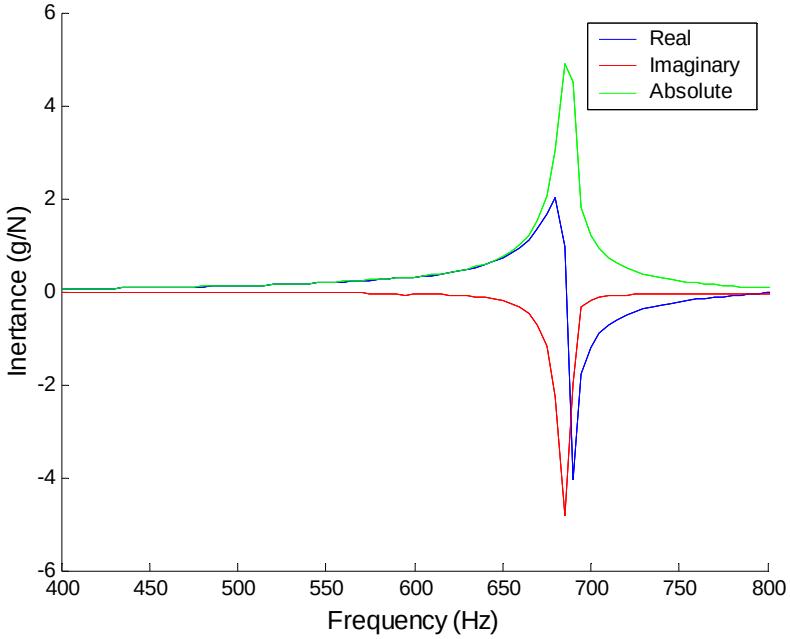


**Figure 6-20: Reduced Mass Actuator Response with PCB Shear Force Sensor and 3/8in Stud**

## *6.2 EMA Experimental Setup*

The complete EMA experimental setup (Figure 6-4) consists of the actuator core, custom sensor plate, and actuator support shelf (Figure 6-2), the Micro-Epsilon© U05 eddy current displacement sensor and custom sensor mount (Figure 5-1), and the PCB model 201M73 force sensor (Figure 6-16). The actuator core and support shelf can be mounted to the aluminum base block at any of the 6 equally-spaced mounting locations to facilitate FRF measurements (Figure 6-21). A Kepco BOP 2010 programmable power supply provides actuator coil currents based on a voltage input command provided by the dSpace 1102. Figure 6-22 shows how these hardware components were used to find tool FRFs.

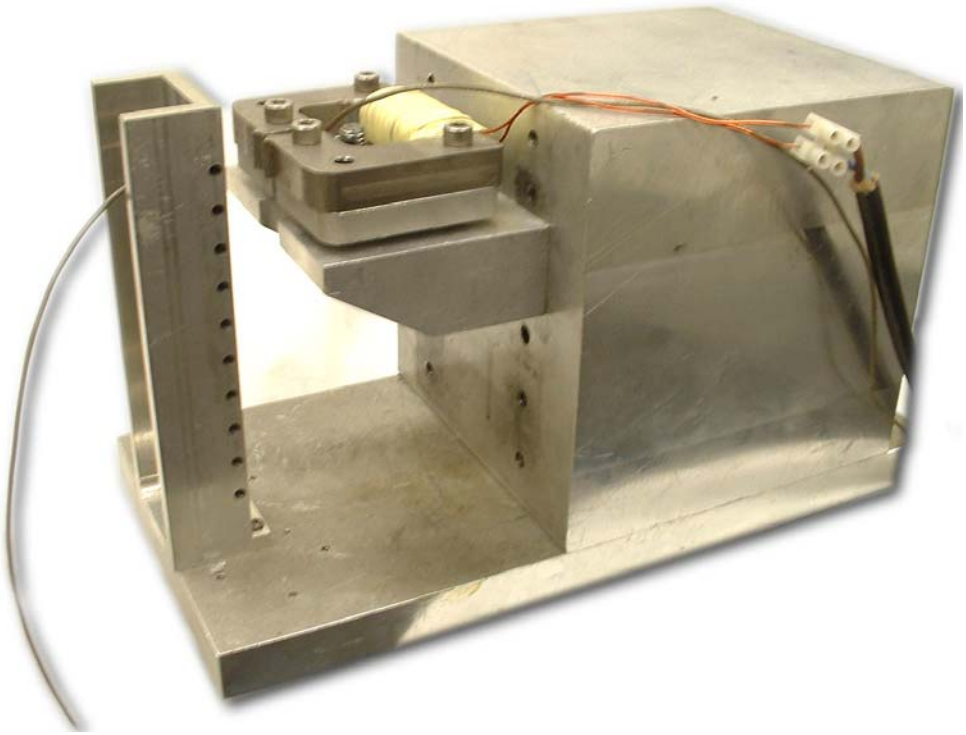

**Figure 6-21: Complete EMA Experimental Setup: Eddy Current Mount and Sensor, Actuator Core, Custom Force Sensor Plate, PCB 201M73 Sensor, Base Block, and Connecting Base Plate**

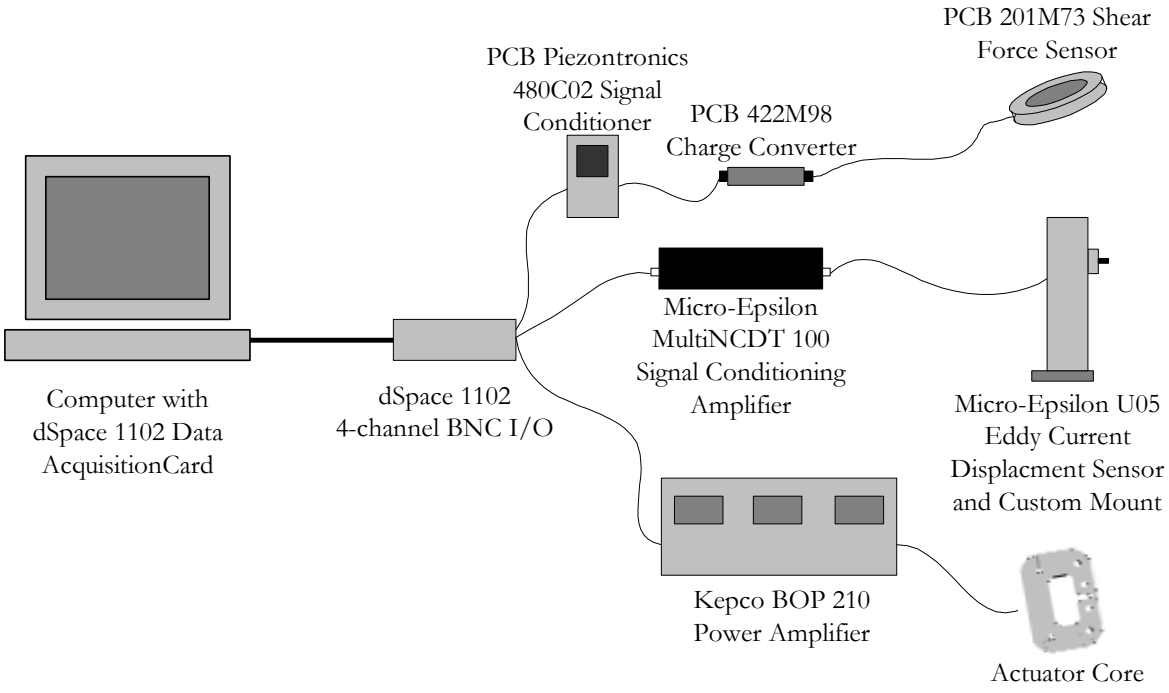


**Figure 6-22: Non-Contacting EMA System Hardware**

As before, algorithms for data acquisition and control algorithm were programmed in Simulink© and interfaced to the dSpace 1102 hardware using Real Time Workshop©. Force and displacement data was acquired, and the swept sinusoidal command signal was updated, at 20.0 kHz using a Simulink program similar to that shown in Figure 5-5.

## *6.3 EMA Test Results*

Frequency response measurements ($X_1/F_1$, $X_2/F_1$, $X_1/F_2$, $X_2/F_2$) were collected from three tool blanks (with overhang lengths 4.75 in, 5.75 in, and 6.75 in) mounted in the HAAS VF-1 collet toolholder. As discussed in Section 3.2, swept sinusoid excitation currents were selected to provide non-contacting excitation forces with peak amplitude of approximately 50 N across a 0-1000 Hz frequency range. Measurement locations are shown in Table 6-4.

**Table 6-4 Non-Contacting EMA Measurement Positions**

| Tool Length cm (in) | 16.5 (6.5) | 19.3 (7.6) | 20.3 (8.0) |
|---|---|---|---|
| Tool Overhang cm (in) | 12.1 (4.75) | 14.6 (5.75) | 17.15 (6.75) |
| $X1/F_1$ Position* cm (in) | 0.635 (0.25) | 0.635 (0.25) | 0.635 (0.25) |
| X2/F2 Position* cm (in) | 8.25 (3.25) | 10.8 (4.25) | 13.3 (5.25) |

*Measured from Tool Tip

Shown in Figure 5-7 through Figure 5-10 are the four measured receptances ($X_1/F_1, X_1/F_2, X_2/F_1, X_2/F_2$) for a 5.75 in tool blank. To facilitate accurate comparisons between EMA and impact hammer FRFs, EMA modal tests were conducted immediately after impact hammer measurements. As noted earlier, the redundant tip-forced FRF ($X_2/F_1$) was omitted as it was less accurate than the top-forced ($X_1/F_2$) measurement.

Measured receptances ( $X_1/F_1$, $X_1/F_2$, $X_2/F_2$ ) for a 5.75 in, 0.5 in diameter tool blank mounted in the HAAS VF-1 are shown in Figure 6-23 through Figure 6-25. Tool resonance is clearly visible at 390 Hz; the secondary peak on the $X_2/F_2$ receptance results from resonance of the actuator support structure. This unwanted mode is above the primary resonant peak (from which stability lobe diagrams are developed) and should not compromise measurement exactness. Figure 6-26 shows a direct comparison to impact hammer results (shown previously in Figure 5-7 through Figure 5-10).

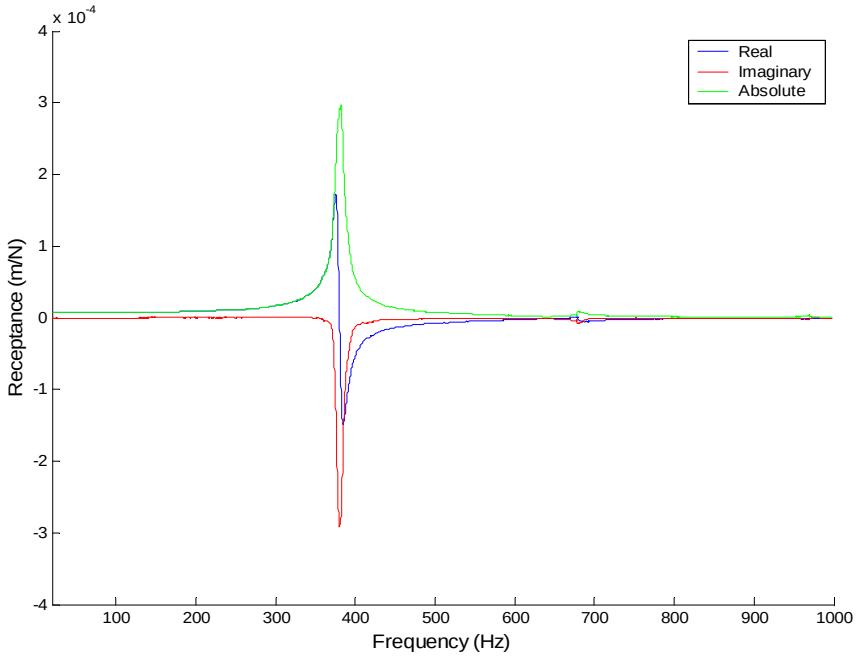


**Figure 6-23: Non-Contacting EMA Actuator $X_1/F_1$ FRF 5.75in Tool**

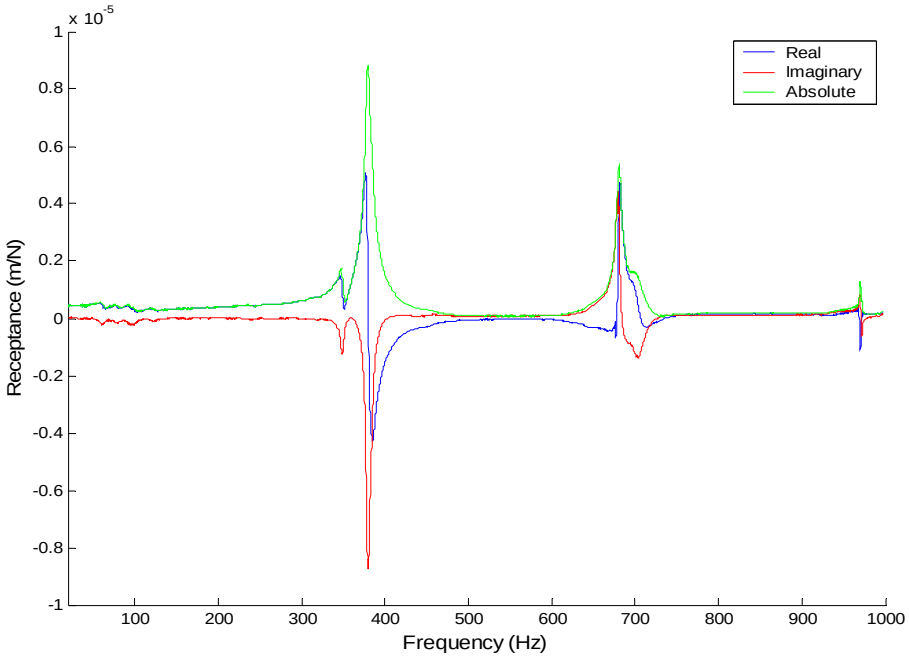


**Figure 6-24: Non-Contacting EMA Actuator $X_2/F_2$ FRF 5.75in Tool**

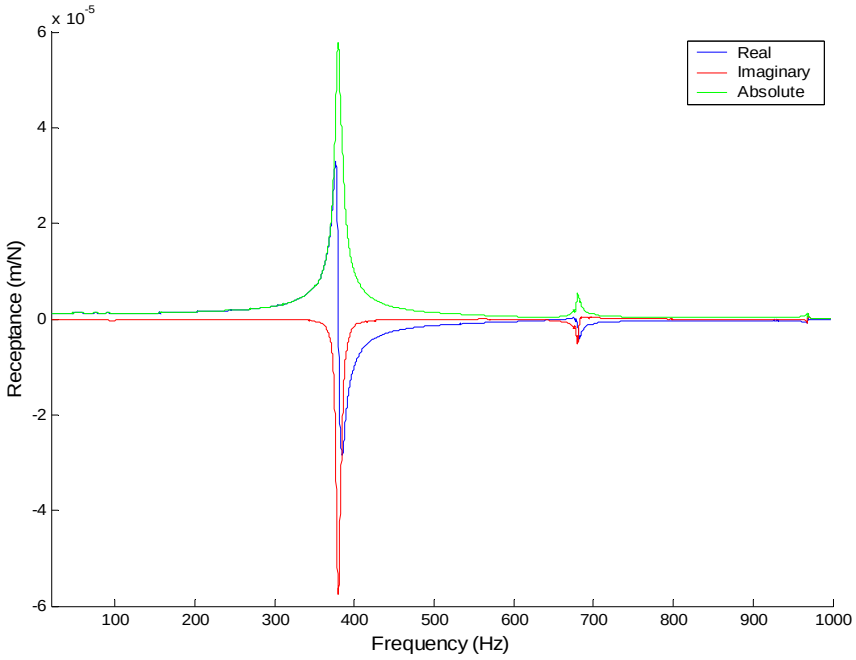


**Figure 6-25: Non-Contacting EMA Actuator $X_1/F_2$ FRF 5.75in Tool**

EMA sweep and impact hammer data (Figure 6-26) for the 5.75in tool blank compares favorably. Small discrepancies between hammer and sweep data are visible near resonance, where real and imaginary amplitudes change rapidly. FRF correlations for longer tool blanks, however, are less favorable (Figure 6-27).

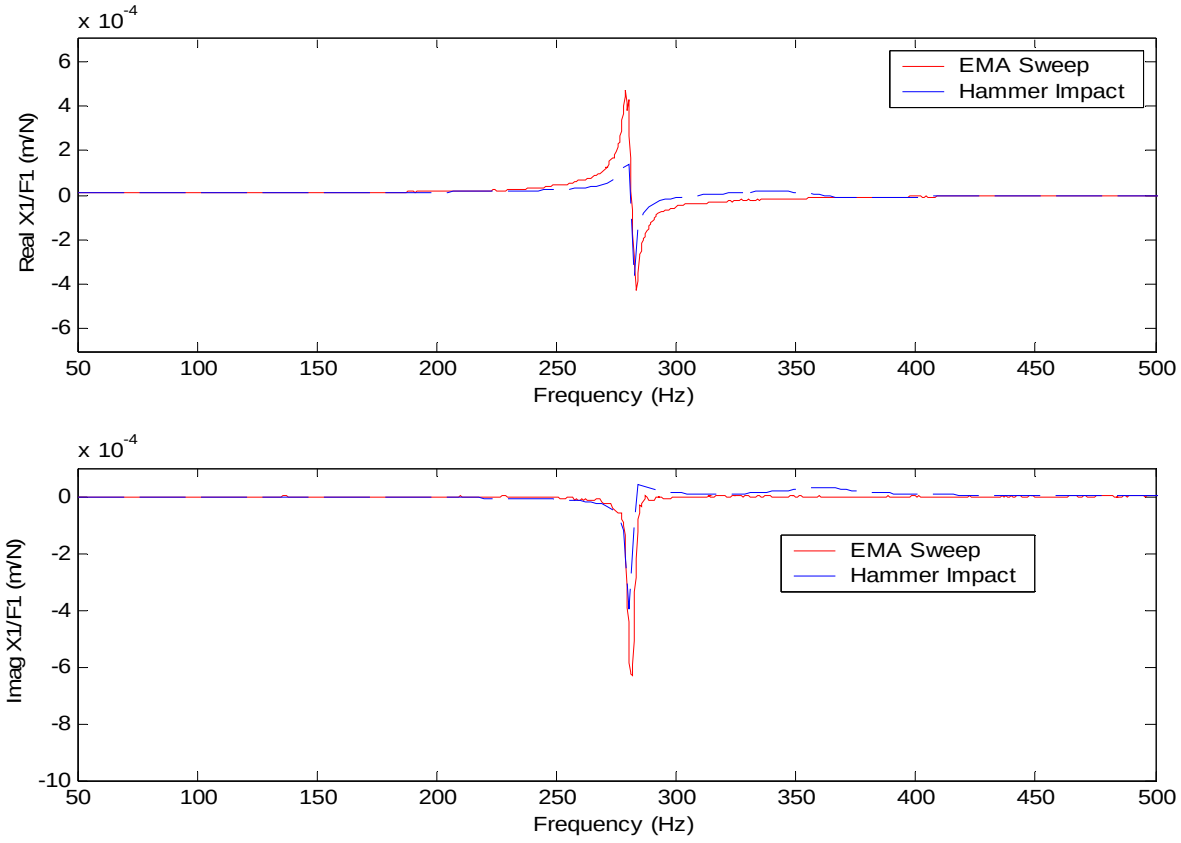


**Figure 6-26: Impact hammer and EMA Sweep Measured $X_1/F_1$ FRF Comparison 5.75in Tool**

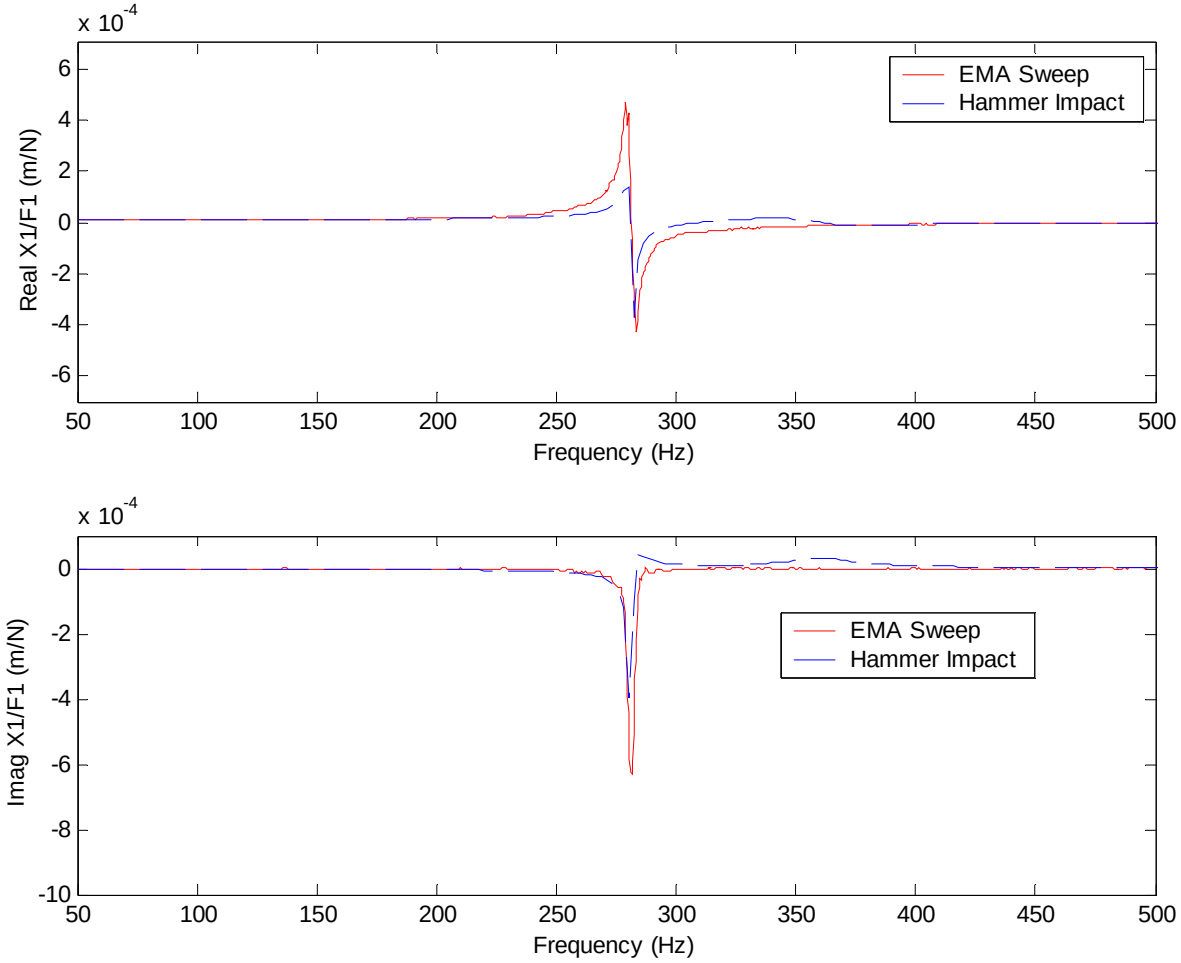


**Figure 6-27: Impact Hammer and EMA Sweep Measured $X_1/F_1$ FRF Comparison, 6.75in Tool**

In fact, FRF amplitude errors increase for modal testing approaches with increasing tool length. For long tools, peak EMA force amplitudes must be significantly reduced (to less than 5.0 N) to avoid actuator contact with the tool. Reducing the range of actuation forces reduces the resolution of the PCB 201M73 force sensor, resulting in poorly-scaled FRF output. Impact hammer testing is also less effective for longer tools: multiple impacts result in distorted FRFs at the resonant peak (Figure 5-19). The impact hammer data shown in Figure 6-27 (for the 6.75 in tool) represents the average of the best 10 of 30 impacts.

## *6.4 Inverse RCSA: Finding Subsystem Receptance*

As with the impact hammer data of Section 5.3, inverse RCSA was used to extract subsystem receptances ($B_1$, $B_2$, and $B_3$) from EMA-generated FRF data for a 4.75 in tool blank. These identified receptances are shown in Figure 6-28 through Figure 6-30.

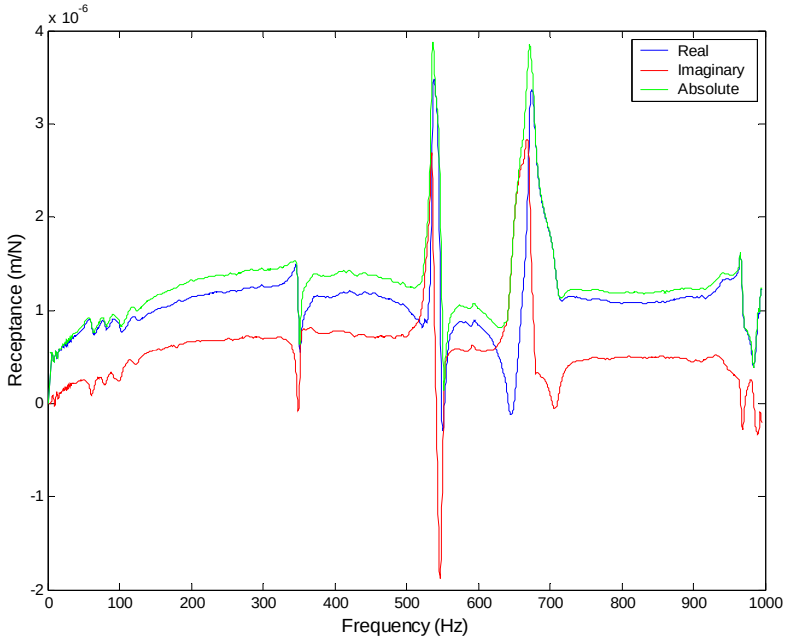


**Figure 6-28: $B_1$ Receptance Measured via EMA Actuator**

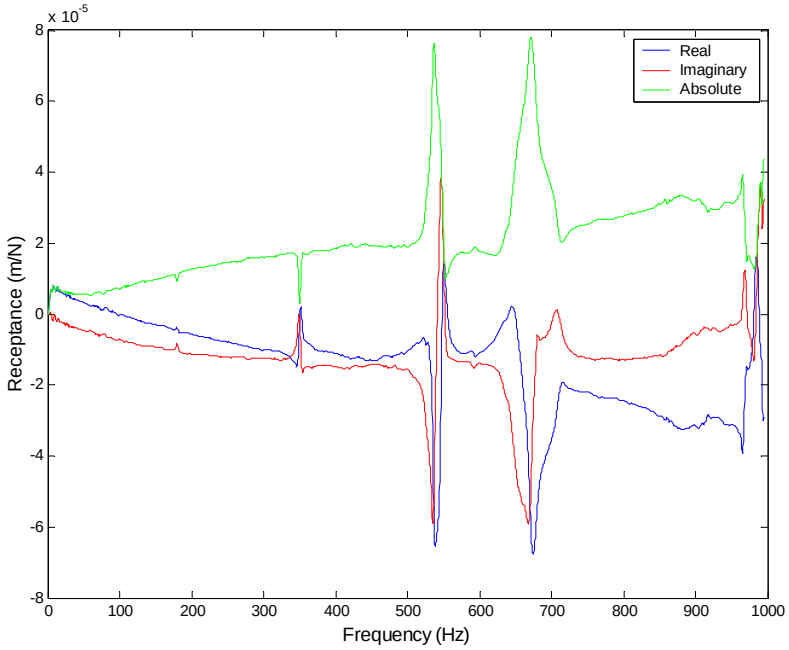


**Figure 6-29: $B_2$ Receptance Measured via EMA Actuator**

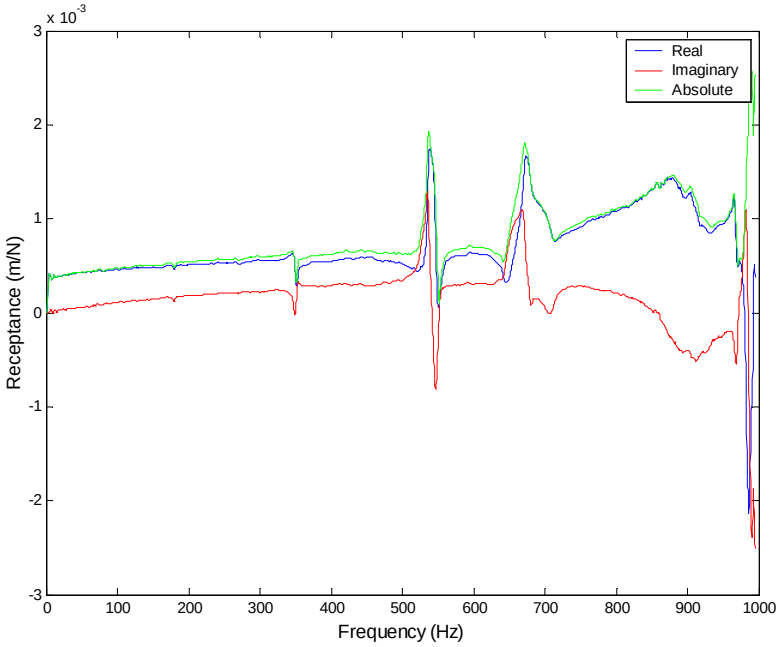


**Figure 6-30: $B_3$ Receptance Measured via EMA Actuator**

Each receptance contains a large peak near 550 Hz, which represents the peak error between the analytic FRF (for free-free tool blank) and the measured FRF. Secondary peaks near 690 Hz represent the fundamental natural frequency of the actuator system, which is limited by the compliance of the PCB 201M73 force sensor. These structural peaks are far less evident on the EMA FRF plots (Figure 6-23 through Figure 6-25); they appear much larger on the B receptance plots because actuator resonance is not accounted for analytically.

As before, the magnitude of the $B_1$ remnant peak (approximately $4\times10^{-6}\ m/N$ in Figure 6-28) can be referenced to the resonant magnitude (approximately $4\times10^{-4}\ m/N$ in Figure 6-23) to assess uncertainty in the RCSA process. Again, the error magnitude for the algebraically-solved $B_1$ receptance is on the order of 1%* of the initial tool-point measurement.

While peak errors associated with EMA-generated subsystem receptances are similar in magnitude to those of impact hammer tests, these receptances are less consistent across the frequency range than those derived from impact hammer testing. Inconsistencies in the EMA subsystem receptances can be attributed to poor signal to noise ratios (20 mV signal / 2 mV noise) associated with the PCB 201M73 force sensor. Again it is important to note that subsystem receptances represent the difference between two receptances with much greater scale. For this reason, small measurement errors can lead to significant changes in the "B" receptances and ultimately influence RCSA predictions.

* B2 and B3 receptances are defined as slope over input force and slope over moment. As a result, these receptances cannot be directly compared to the measured receptances. Accuracy is assumed similar to that of the B1 receptance.

## *6.5 Forward RCSA: Predicting Tool-point FRFs*

The identified subsystem receptances extracted from EMA test data ($B_1$, $B_2$, $B_3$) were then combined using boundary and compatibility conditions with analytic tip receptances for a tool blank of new dimensions (Equation 3.24). Figure 6-31 compares the predicted FRF for a 6.75 in tool blank (computed using the B receptances extracted from 4.75 in tool data) and the actual measured FRF.

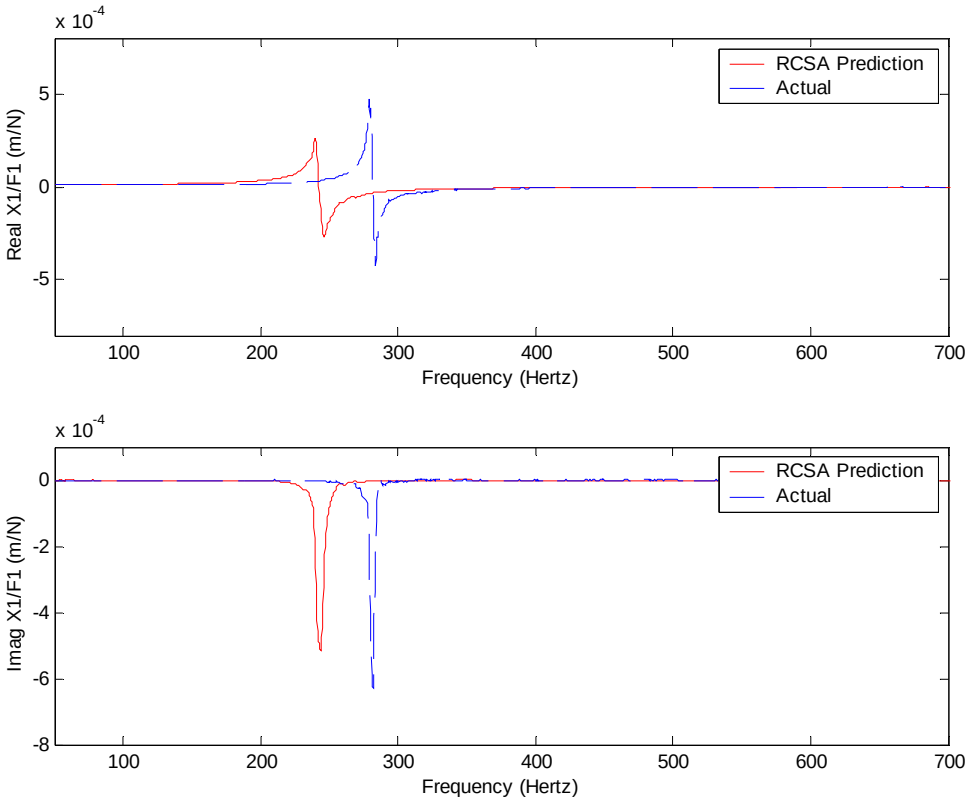


**Figure 6-31: RCSA Predicted FRF and EMA Measured $X_1/F_1$ FRF 6.75in Tool**

The sizeable errors between predicted and measured FRFs result from inaccuracies in the extracted subsystem receptances ($B_1$, $B_2$, $B_3$). These inaccuracies are caused by inadequate signal to noise ratio associated with low actuator force amplitudes (peak input 6.0 N). While actuator coil currents and

the tool/actuator air gap could be adjusted to increase force amplitudes (without causing EMA/tool contact), such modifications would require a complete redesign of this prototype EMA system and are beyond the scope and funding of this project. Instead, signal processing was investigated as a means of rectifying measurement inaccuracies. Measured FRFs were smoothed using digital filtering techniques prior to RCSA processing. Although this filtering produced smoother FRF plots (Figure 6-32), it may have altered the magnitude and phase of the measured data enough to compound the B receptance errors. Once again, small differences between these filtered measurements and analytic tool receptances lead to errors in the predicted subsystem receptances (the inverse RCSA process) and tool-point FRF predictions (the forward RCSA process).

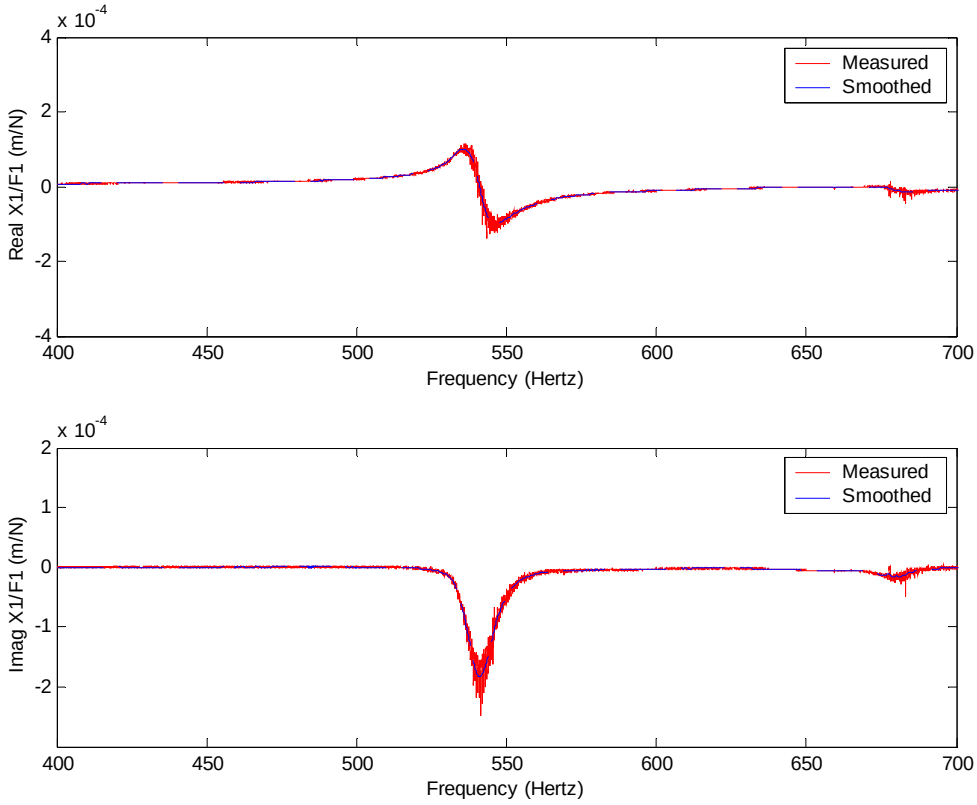


**Figure 6-32: Measured and Smoothed EMA $X_1/F_1$ FRF 4.75in Tool**

# 7. RCSA Prediction Errors

One of the major objectives of this research project was to accurately predict tool-point FRFs using RCSA theory. Quite a bit of time and energy was invested in refining the impact hammer and EMA system measurement techniques and improving signal processing in an effort to make precise predictions. While RCSA predictions made with impact hammer input are noticeably more accurate than those based on the current** EMA system measurements, the predicted impact hammer FRF magnitudes differ from the actual FRF by almost 25%.

In order to determine the cause of these unacceptably large prediction errors, tests were conducted on the double mass spring damper RCSA simulation. As noted in Section 3.2.2, the small RCSA prediction error found in the original MSD simulation (shown enlarged in Figure 7-1 and in Figure 3-12) appears to be caused by slight inaccuracies introduced by the Matlab FFT function (which is used to convert time record input and response to frequency domain.) The magnitude of the prediction error is $5 \times 10^{-5}\ N/m$.

In order to test this hypothesis, an analytic solution for the double MSD was used as input to the RCSA algorithm instead of the FFT-transformed response. RCSA predictions were made using the same parameters as in the original simulation. Figure 7-2 compares the new predicted response (based on analytic input) with the analytic solution.

** Improving the EMA system stiffness would allow FRF measurements with greater input force and would result in much improved measurement accuracy.

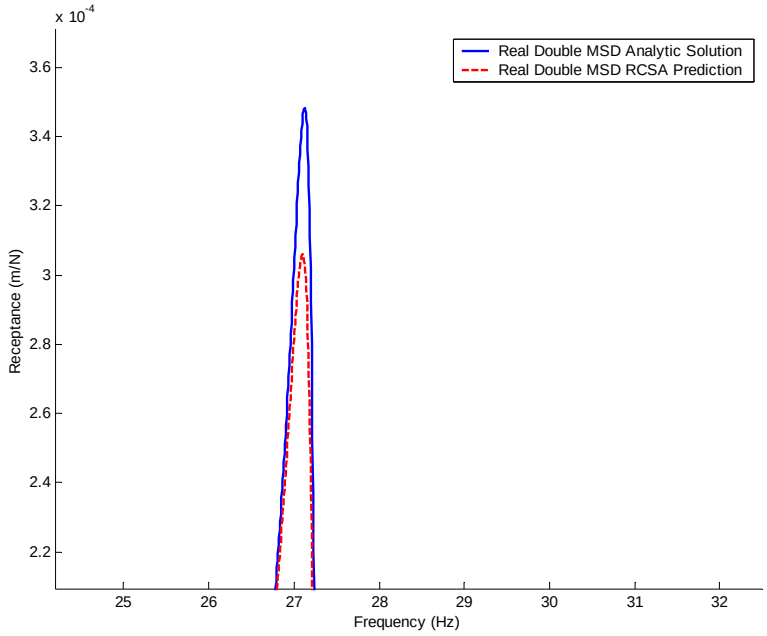


**Figure 7-1: Enlarged View Double MSD Simulation RCSA Prediction and Analytic Solution**

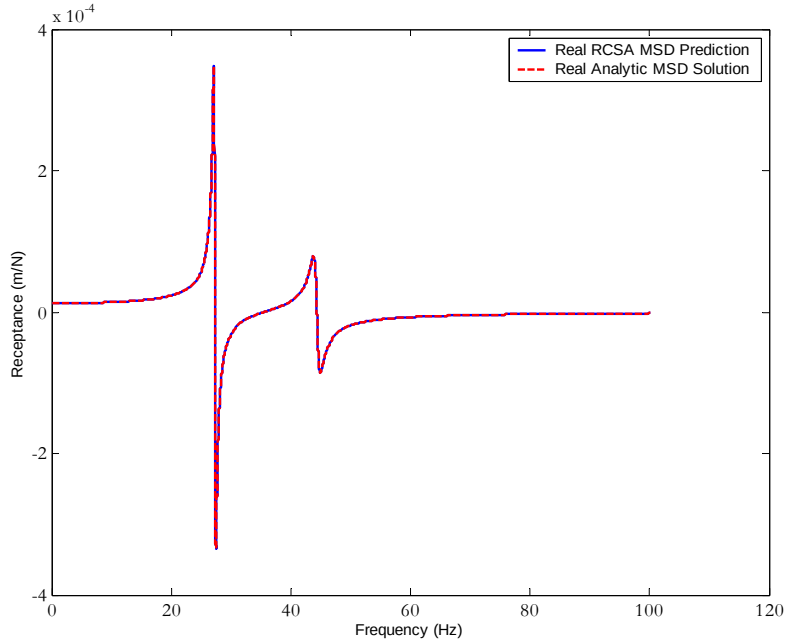


**Figure 7-2: RCSA Double MSD Simulation Prediction and Analytic Solution**

The predicted and actual plots are identical; the enlarged view of Figure 7-3 shows prediction accuracy to the numeric precision of the Matlab program.

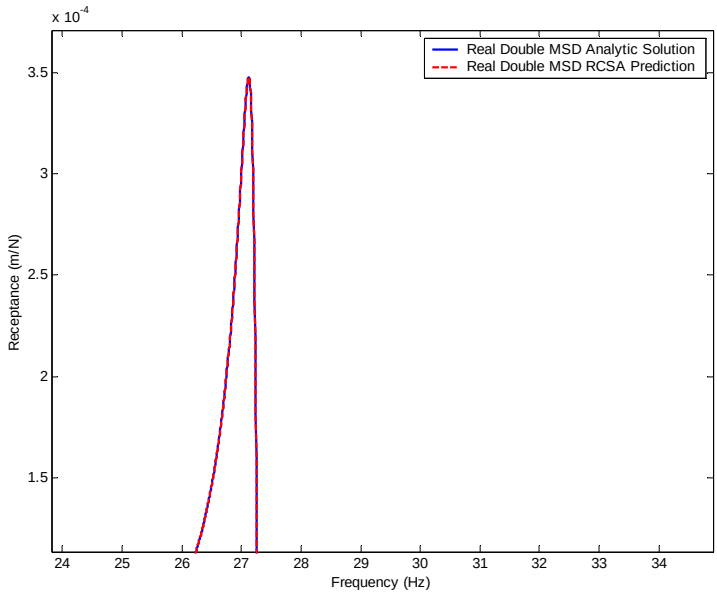


**Figure 7-3: Enlarged View Double MSD Simulation RCSA Prediction and Analytic Solution**

The simulation plots above seem to indicate that the MSD RCSA software is very sensitive, even to very small input (less than .01%) errors. To investigate the effects of measurement noise on the accuracy of FRF predictions, additional simulations were conducted using the double MSD system Figure 3-2. Figure 7-4 illustrates the effects of introducing 2% white noise and 1 Hz offset to the system excitation function.

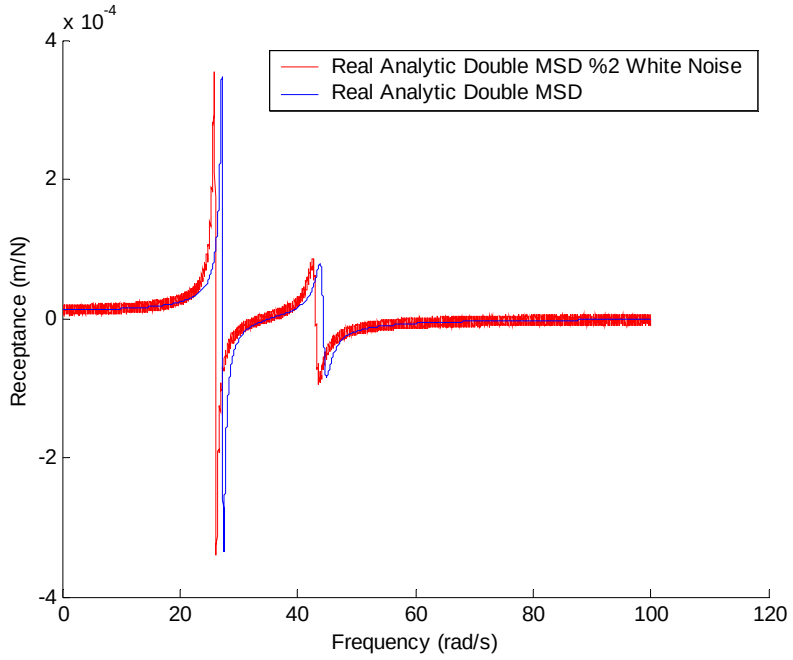


**Figure 7-4: Double MSD Input Comparison (Analytic and 2% White Noise)**

Figure 7-5 shows subsystem receptances computed via inverse RCSA using the analytic and white noise data sets of Figure 7-4. The error of the computed receptance is far greater than the magnitude of the white noise included in the input FRF. The comparison plot between FRFs predicted with the white noise input and the original analytic input (Figure 7-6) demonstrates that input inaccuracies as low as 2% can create errors in the range of 25% in the FRF prediction.

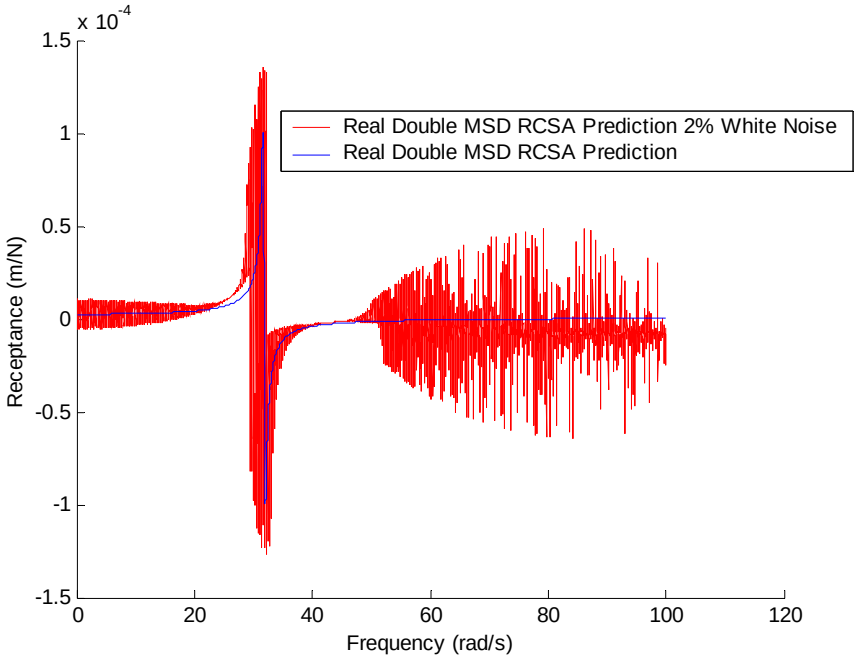


**Figure 7-5: Computed Double MSD Subsystem Comparison (Analytic and 2% White Noise)**

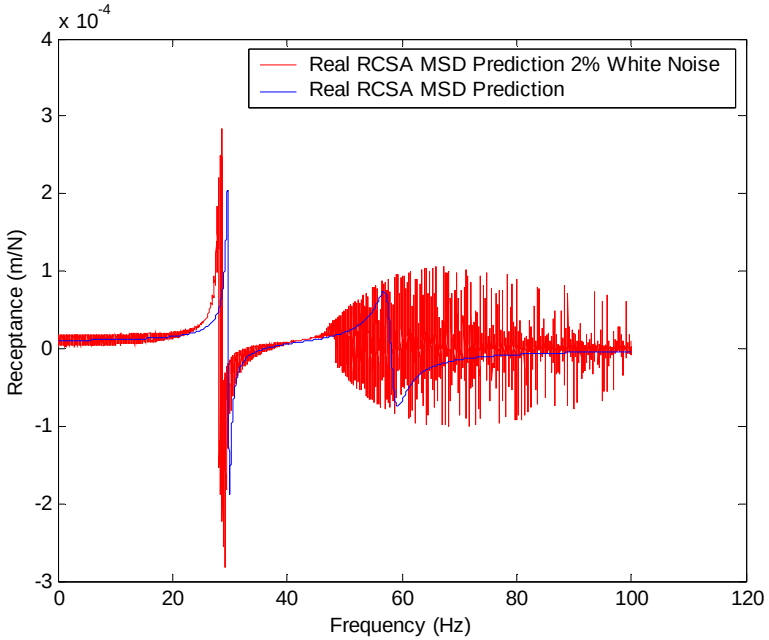


**Figure 7-6: RCSA Predicted Double MSD FRF Comparison (Analytic and 2% White Noise)**

These preliminary simulations indicate that even small levels of measurement noise (SNR > 34 dB) lead to significant errors in the inverse and forward RCSA process, even for low-order linear systems like the double MSD. This issue needs to be further investigated and resolved for experimental implementations to be useful.

If these investigations conclude that RCSA predictions based on experimental data are as susceptible to measurement errors and noise as the MSD simulations are, the chances of making accurate tool-point FRF predictions using this approach are very slim. Even the most precise modal testing methods can be expected to have 2-5% measurement error [6]. Before attempting a redesign of the EMA system or any refinements to the measurement process, acceptable levels of measurement error for accurate FRF prediction need to be determined.

# 8. Conclusions

The first research objective of this thesis was to design and demonstrate a non-contacting EMA actuator and sensor system that simplifies the measurement of tool-point FRFs on high speed machining centers. The second research goal was to adapt classical RCSA methods to predict tool-point FRFs on high speed machining centers. The predicted milling system FRFs found through the Matlab RCSA algorithms were intended to be converted into stability lobe diagrams for chatter prediction. The non-contacting EMA system proved to be a complete success. The inverse RCSA algorithm was found to be extremely sensitive to any inconsistencies in the FRF input data.

This second-generation EMA prototype improves upon existing non-contacting actuators, namely the NIST "best speeds device", which was developed for similar purposes. The actuator imparts controllable, high-amplitude (0-50 N) excitation forces to ferromagnetic machine tools across a broad frequency range (0-1000 Hz). The accuracy and simplicity of this EMA technology in predicting tool-point FRFs are demonstrated using 0.50 in diameter HSS tool blanks mounted in a HAAS VF-1 3-axis CNC milling center. Comparisons to FRFs obtained from impact hammer testing are very favorable. Small discrepancies resulting from inadequate EMA force measurement resolution and hammer tip bouncing at impact are noted.

'Inverse RCSA' techniques were used to extract unknown receptances (associated with the milling machine structure) from these EMA-measured tool-point FRFs. A 'Forward RCSA' procedure utilized these identified receptances and analytic tool models to predict tool-point FRFs for a range of cutting tools. Although this approach proved to be very effective in linear mass, spring, damper (MSD) simulations, experimental results from HAAS VF-1 3-axis CNC milling center were not accurate. Experimental limitations on peak actuator force (approximately 6.0 N to prevent

tool/actuator contact) and frequency range (approximately 720 Hz to avoid structural resonance) resulted in measurement errors that prevented accurate identification of subsystem receptances and inaccurate prediction of tool-point FRFs.

It is possible that these inaccuracies could be reduced or eliminated through subsequent EMA design iterations. Stiffer and more accurate force sensing should be implemented to keep the fundamental frequency of the EMA structure above 1500 Hz. This design enhancement would allow accurate FRF measurements on stiffer tools (with higher fundamental frequencies) and more accurately characterize the milling machine dynamics (tool, toolholder, and spindle structure).

# 9. Bibliography


[1] Sandia National Laboratories, "High Speed Machining," 2003.

[2] Unigraphics, "High-Speed Machining Using NURBS Technology," vol. 2002: Unigraphics, 2002.

[3] M. Davies, Pratt, J., Dutterer, B., "Device for Stable Spindle Speed Determination in Machining." US, 2002.

[4] J. Tlusty, *Manufacturing Processes and Equipment*. Upper Saddle River, NJ: Prentice Hall, 2000.

[5] H. Merrit, "Theory of Self-Excited Machine-Tool Chatter Contribution to Chatter Research-1," *Journal of Engineering for Industry*, vol. 87, pp. 447-454, 1965.

[6] Hewlett-Packard, "The Fundamentals of Modal Testing." Palo Alto, CA, 1986.

[7] J. Sutherland, Devor, R., "A Dynamic Model of the Cutting Force System in the End Milling Process," *Sensors and Controls for Manufacturing, ASME PED*, pp. 53-62, 1988.

[8] T. Delio, Jiri, T., Smith, S., "Use of Audio Signals for Chatter Detection and Control," *Transactions of the ASME*, vol. 114, pp. 146-157, 1992.

[9] D. Caulfield, "Electromechanical Actuator Development for Integrated Chatter Prediction on High Speed Machining Centers," in *Mechanical Engineering*. Raleigh: North Carolina State, 2002.

[10] D. Esterling, Caulfield, D., Kiefer, A., Buckner, G., "Inverse RCSA Method for Obtaining the Frequency Response Functions of CNC Machine Tools," presented at IMECE2003, Washington, D.C, 2003.

[11] T. Schmitz, Davies, M., Medicus, K., Snyder, J., "Predicting High-Speed Machining Dynamics by Substructure Analysis," in *NIST*. Gaithersburg, 2000.

[12] T. Schmitz, Burns, T, "Receptance Coupling for High-Speed Machining Dynamics Prediction," presented at International Modal Analysis Conference, 2003.

[13] S. Park, Altintas, Y., "Identification of Spindle Integrated Force Sensor's Transfer Function for Modular End Mills," presented at 2003 ASME Int. Mech Eng Congress1, Washington, DC, 2003.

[14] R. Bishop, Johnson, D., *Mechanics of Vibration*. Cambridge, England.: Cambridge University Press, 1960.

[15] T. Schmitz, Davies, M., Medicus, K., Snyder, J., "Improving High-Speed Machining Material Removal Rates by Rapid Dynamic Analysis," in *Mechanical Engineering and Engineering Science*. Charlotte: North Carolina Charlotte, 2000.

[16] D. Esterling, "Active Electromagnetic Device for Measuring Method the Dynamic Response of a Tool in a CNC Machine." USA, 2003.

[17] D. Esterling, "Method for Reducing the Measurement Requirements for the Dynamic Response of Tools in a CNC Machine," 2003.

[18] C. Salomon, "Process for the Machining of Metals or Similar Acting Materials When be Worked by Cutting Tools." Germany, 1931.

[19] ASME Committe on Metal Cutting Data, "Manual on Cutting Metals," ASME, New York 1939.

[20] R. Arnold, "The Mechanism of Tool Vibration in the Cutting of Steel," *Proc. Inst. of Mechanical Engineers*, vol. 154, pp. 261-276, 1946.

[21] S. Tobias, "The Vibrations of Vertical Milling Machines Under Test and Working Conditions," *Proc. Inst. of Mechanical Engineers*, vol. 474, 1959.

[22] S. Tobias, *Machine-Tool Vibration*. New York: John Wiley and Sons Inc, 1965.
[23] S. Tobias, Fishwick, W., "Theory of Regenerative Machine Tool Chatter," *Engineering London*, vol. 205, 1958.
[24] J. Peters, "What Can Vibration Research Contribute to Machine Tool Development," presented at Prod. Eng. Res. Conference, Pittsburg, 1963.
[25] J. Tlusty, Polacek, M., "The Stability of the Machine Tool Against Self-Excited Vibration in Machining," presented at Prod. Eng. Res. Conference, Pittsburg, 1963.
[26] S. Smith, Tlusty, J., "An Overview of Modeling and Simulation of the Milling Process," *Journal of Engineering for Industry*, vol. 113, pp. 169-175, 1991.
[27] Modern Machine Shop, "High Speed Machining: Aerospace
Boeing's One Part Harmony," 1999.
[28] J. Tlusty, Ismail, F., "Special Aspects of Chatter in Milling," *Transactions of the ASME*, vol. 105, 1981.
[29] MALInc, "Cutpro Software," vol. 2004, 2004.
[30] M. Weck, "Adaptive Control for Face-Milling Operation with Strategies for Avoiding Chatter-Vibrations and for Automatic Cut Distribution," *Annals of CIRP*, vol. 24, pp. 405-409, 1975.
[31] E. Budak, "Improving Productivity and Part Quality in Milling of Titanium Based Impellers by Chatter Supression and Force Control," *Annals of CIRP*, vol. 49, pp. 31-40, 2000.
[32] M. Shiraishi, Kume, E., "Suppression of Machine-Tool Chatter by State Feedback Control," *Annals of CIRP*, vol. 37, pp. 369-372, 1988.
[33] Ingersoll-Rand, "Harmonizer," 2000.
[34] D. Browning, Golioto,. I , Thompson, N., "Chatter Suppression in Milling: An Active Approach," presented at Dynamics System and Control Division - 1999, Nashville, Tn, 1999.
[35] D. Ewins, *Modal Testing: Theory and Practice*. Letchworth: Research Studies Press, 1984.
[36] T. Schmitz, Burns,T., "Receptance Coupling for High-Speed Machining Dynamics Prediction," presented at IMAC-XXI, 2003.